A MINIATURE HIGH RESOLUTION ENDOSCOPE FOR 3D ULTRASOUND IMAGING

by

Katherine Latham

Submitted in partial fulfilment of the requirements
for the degree of Doctor of Philosophy

at

Dalhousie University
Halifax, Nova Scotia
August 2020

TABLE OF CONTENTS

LIST OF TABLES

LIST OF FIGURES

ABSTRACT

Miniaturized ultrasound imaging arrays have many potential clinical applications, specifically, in guiding surgical procedures. 3D capable probes are also particularly suited to endoscopic applications because of the large amount of information that can be gathered without being sensitive to the position of the tool within the patient. A 3D dataset can provide imaging access to hard to view planes, accuracy in volume measurements and flexibility in image display. Unfortunately, for a fully sampled 2D array capable of 3D imaging, the fabrication challenges inherent to requiring thousands of small piezoelectric array elements are prohibitive when considering endoscopic packaging constraints. This dissertation presents an approach to developing a low channel count, endoscopic, real-time capable 3D imaging system using a crossed electrode array architecture and bias-sensitive piezoelectrics.

A 30 MHz, 128 element crossed electrode array based on a 1-3 relaxor composite substrate was fabricated for this work. The reduction in the total element count of the crossed electrode array eases the challenges of electrically connecting a fully sampled 2D array. However, there is still a challenge in connecting to back-side and front-side elements. A process has also been developed that uses a thinly diced strip of flexible circuit board to bring the back-side connections to a front-facing bond surface, which allows the final size of the forward-looking endoscope to measure only 6 mm x 5 mm.

The imaging techniques developed for this array build on the concept of an electrically steerable elevation lens for 3D imaging. New beamforming techniques have been developed to improve the image quality in the elevation plane by creating an electrically reconfigurable lens with a bias-sensitive array substrate. In the first technique, a Fresnel mimicking lens is created along the elevation dimension of the crossed electrode array. Compounding a set of Fresnel patterns creates a high-quality, two-way elevation lens focus and can be steered to a moderate range of angles ($\pm 15^{\circ}$). Alternatively, the second approach uses a Fresnel lens on transmit for elevation slice selection combined with Hadamard receive coding. Using either of these steerable elevation lenses, imaging in azimuth is completed simultaneously. Therefore, when ultrafast imaging is employed in azimuth, each elevation slice can be collected at high frame rates and full volume images can be generated in real-time (19.5 volumes/s).

LIST OF ABBREVIATIONS AND SYMBOLS USED

1D		One-dimensional
2D		Two-dimensional
3D		Three-dimensional
A	$[m^2]$	Cross sectional area
AC		Alternating current
A-scan		Amplitude scan
ASIC		Application specific integrated circuit
$B(\theta, r, n)$		Beamformed data for a line, for an element
B-mode		Brightness mode
BW	%	Fractional bandwidth
c	$[m/s]$	Speed of sound
c	$[N/m^2]$	Stiffness constant in constitutive equations
C_0	$[F]$	Clamped capacitance
CAD		Computer-aided design
CMUTs		Capacitive micromachined ultrasonic transducers
CT		Computed tomography
d	$[C/N]\ or\ [m/V]$	Piezoelectric constant
d	$[m]$	Thickness
D	$[C/m^2]$	Electric displacement
D	$[m]$	Aperture width
$D(\theta)$		Directivity function
DC		Direct current
DRIE		Deep reactive ion etch
e	$[C/m^2]$	Piezoelectric stress constant
E	$[V/m]$	Electric field

f	$[Hz]$	Frequency
f_0 or f_c	$[Hz]$	Centre frequency
f_a	$[Hz]$	Anti-resonant frequency
f_r	$[Hz]$	Resonant frequency
f_h	$[Hz]$	High frequency spectrum threshold
f_l	$[Hz]$	Low frequency spectrum threshold
F		F-number
F	$[N]$	Force
$flex$		Flexible circuit board
FORCES		Fast Orthogonal Row Column Electronic Scanning
FPGA		Field programmable gate array
FR	$[Hz]$	Frame rate
FWHM		Full width at half maximum
$FWHM_{ax}$	$[m]$	Axial resolution
$FWHM_{lat}$	$[m]$ or $[°]$	Lateral resolution or beamwidth
g	$[V * m/N]$	Piezoelectric voltage constant
h	$[V/m]$ or $[N/C]$	Piezoelectric constant
$\boldsymbol{H}$		Hadamard matrix
$\boldsymbol{I}$		Identity matrix
ICE		Intracardiac echocardiography
IEEE		Institute of Electrical and Electronics Engineers
k_t		Electromechanical coupling factor
K		Relative dielectric constant
KLM		Krimholtz-Leedom-Matthaei
l	$[m]$	Length from element to focus
LC		Inductor-capacitor
M	$[m^2/V^2]$	Electrostrictive coefficient for electric field
Mg		Magnesium

MR		Magnetic resonance
$n\ or\ N$		Number of elements
N_C		Number of compounded Fresnel patterns
N_S		Number of elevation slices
N_t	$[Hz * m]$	Thickness mode frequency constant
Nb		Niobium
Nd:YAG		Neodymium-doped yttrium aluminum garnet
P	$[C/m^2]$	Polarization
PMN-PT		Lead magnesium niobate-lead titanate
PRF		Pulse repetition frequency
PZT		Lead zirconate titanate
Q	$[m^4/C^2]$	Electrostrictive coefficient for polarization
r_n	$[m]$	Radius of Fresnel zone plate rings
R_A	$[\Omega]$	Transducer electrical resistance
$\boldsymbol{R}$		Matrix of receive coded signals
$\boldsymbol{R_D}$		Matrix of decoded RF data
RC		Resistor-capacitor
RF		Radio frequency
s	$[1/(N/m^2)]$	Elastic constant
S		Strain
S_{bias}	$\pm$	Sign of the bias
SA		Synthetic aperture
SAFE		Simultaneous Azimuth and Fresnel Elevation
SNR		Signal to noise ratio
T	$[N/m^2]\ or\ [Pa]$	Stress
$\boldsymbol{T}$		Transmit pulse matrix
T_C	$[°C]$	Curie temperature
TEE		Transesophageal echocardiography

TOBE		Top Orthogonal to Bottom electrode
US		Ultrasound
UV		Ultraviolet
v_L	$[m/s]$	Longitudinal velocity
w	$[m]$	Element width
Z_0	$[MRayl]$	Acoustic impedance
α	$[°]\ or\ [rad]$	Plane wave angle
β	$[1/(F/m)]$	Dielectric constant
ε	$[F/m]$	Permittivity constant
ε_0	$[F/m]$	Vacuum permittivity
λ	$[m]$	Wavelength
ρ	kg/m^3	Density
τ	$[s]$	Time delay
φ	$[°]\ or\ [rad]$	Phase delays
$\boldsymbol{\Phi}$		Field transfer matrix
(x, y, z)		Position in cartesian coordinates
(θ, r)		Polar coordinate for a sector scan

ACKNOWLEDGEMENTS

First, I would like to thank my supervisor Dr. Jeremy Brown. Dr. Brown is generous with his time, encouragement and inventive ideas. I am lucky to have learned in his lab.

My supervisory committee was also instrumental in the completion of this dissertation. Dr. Rob Adamson provided technical support, often asking the questions that had gone unnoticed. Dr. Timothy Bardouille shared important insights from a perspective outside of ultrasound that are greatly appreciated.

Thank you to Dr. Zemp and Dr. Chris Ceroici for hosting me in Edmonton and helping with the early imaging experiments.

To the members of the Dalhousie Ultrasound Lab, thank you for the collaborative and positive atmosphere created within our group. A particular thanks goes to Chris Samson, Jeff Woodacre, Debbie Wright, Dr. Tom Landry and Dr. Eric Simpson for their contributions to this work.

Thank you to my parents and family for their unwavering support. Margot and William, I will always treasure the many distractions from research that you provided.

Finally, for keeping me calm, happy and well fed, thank you Adam.

CHAPTER 1
INTRODUCTION

Conventional ultrasound imaging systems display 2D images or slices of a volume of tissue. While ultrasound is a powerful imaging modality, there is a limitation to the amount of information that can be gleaned from a 2D image of 3D anatomy. Using the example of imaging a tumour, ideally, there would be a full picture of the size, shape and edges of the lesion as well as the interaction with the surrounding tissue. In a 2D system, the operator can move the probe in space as they are identifying anatomy slice by slice. There is a skill required to connect the image slices with the probe movement while manually sweeping. Using a 3D ultrasound system, the movement is not necessary to generate a 3D visualization of the anatomy and linking the slices of a volume is computerized and automatic. The volume can be displayed in the software post-capture by flipping through sequential slices or by displaying a rendered 3D image of the data. A 3D capable system has the added advantage of needing less area for movement during imaging and, because of this, will be easier to operate in confined spaces while still visualizing hard to access image planes.

One clinical application this dissertation is targeting is image-guided neurosurgery. In minimally invasive neural surgery, small burr holes are drilled into the skull and endoscopic instruments and visualization tools are placed

through the burr holes. The tools can be guided down into the folds of the brain, called sulci, to reach the region of the brain containing a lesion. Alternatively, the endoscopic visualization tools can be guided down the surgical pathway and this may be preferred to using the sulci depending on the particular pathology and surgeon (Figure 1-1).

The goal of this project was to develop a 3D capable ultrasound system and novel 3D image building technique. Given the minimally invasive surgical applications that are of interest, the main requirements of the 3D ultrasound system were:

- minimal, or no, increase in RF channel count compared with a 2D imaging system
- an endoscopic form factor
- real-time volumetric frame rates

B-mode ultrasound images are built by electronically focusing the acoustic energy. The beam is focused by inserting channel-to-channel delays in the RF data associated with the elements of the transducer array. The electronics required to beamform ultrasound images get more complex and costly with added RF data channels. Minimizing the number of channels (array elements) for 3D imaging inherently minimizes the complexity added to the system. The Dalhousie Ultrasound Lab has previously developed a custom 64-channel beamformer and

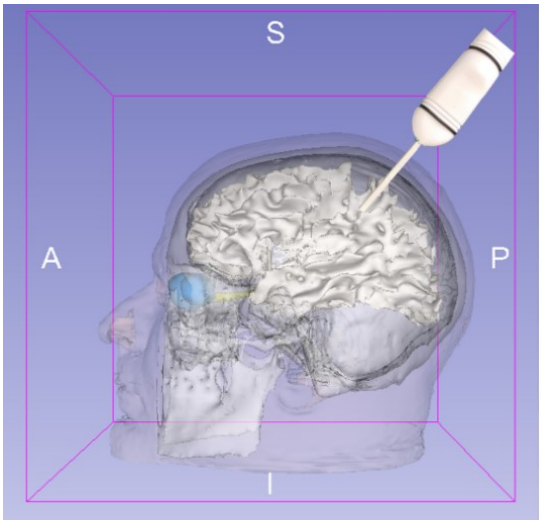

Figure 1-1 A diagram of the proposed use of the imaging probe, through a burr hole surgical approach. The head model and MR data set provided by Slicer 3D software as an example [132], [180].

would like the 3D functionality to be a simple module added to the current system. The need for adding electrical channels dedicated to the perpendicular plane can be eliminated by expanding the concept of an acoustic lens. Conventional 1D ultrasound arrays have a fixed acoustic lens that focuses the ultrasound energy in the elevation direction and improves the slice selection in the 2D image (reduces the slice thickness). If a lens could be created that could be reconfigured to steer to different angles, a 3D image could be built up from multiple elevation 2D image slices. This concept of a steerable lens is the kernel of the idea supporting my approach to a 3D ultrasound system. The imaging techniques that have been developed from this concept are detailed in the following chapters.

The endoscopic form factor is an important consideration for the physical design of the array and the fabrication process. The largest influence on packaged array size is the element count, which, fortunately, aligns well with the first requirement. The chain of electrical connections typically begins with a cable connected to the beamforming electronics on one end and a flexible circuit board (flex or flex circuit) on the other. The flexible circuit board generally has a connector for the cable as well as a set of wire bonding pads, one for each array element. A wire bond from a flex wire bonding pad to each array element provides the electrical connection. These electrical connections between the array elements and the flexible circuits require a large percentage (>50%) of the total surface area of the front face of the array. Therefore, the careful design of the placement and type of electrical interconnects to the array will be of utmost importance. When considering the design of the active, piezoelectric portion of the array the endoscopic requirement dictates that the array will need to be high frequency (> ~20 MHz) because high resolution is required and resolution scales with frequency. Also, the size of ultrasound array elements inversely scale with frequency which is beneficial for the size requirement of an endoscopic device.

Frame rate is a key challenge and requirement for the 3D system because imaging schemes that focus to more points in the image typically require more transmit/receive pulses. The maximum frame rate is determined by two factors: 1) the number of insonifications necessary to build a volumetric image and 2) the

maximum pulse repetition rate between insonifications. The allowable pulse repetition rate is governed by the time required for a pulse to propagate from the array to the largest depth in the image and back. This time-of-flight is fixed unless we shrink our image window, so we will be focussing on the total pulse count when considering imaging techniques in the following chapters. Maintaining real-time frame rates is important to avoid motion artifacts due to respiratory and cardiac motion, which degrade image quality.

1.1 Research Objectives

The general approach to developing the low channel count, endoscopic, real-time capable 3D imaging system was to use a crossed electrode array architecture and bias-sensitive piezoelectrics. The imaging techniques developed for this array build on the concept of an electrically steerable elevation lens and other new beamforming techniques are used to improve the image quality in the elevation plane. The reduction in the total element count of the crossed electrode array eases the challenges of electrically connecting a fully sampled 2D array. However, there is still a challenge in connecting to back-side and front-side elements. A new method is used to bring the back-side connections to the accessible front face that allows the forward-looking crossed electrode array to be packaged into an endoscopic form factor. The dissertation is divided into three studies. Each study

builds towards the objective of developing a 3D capable, endoscopic ultrasound imaging system.

1.1.1 Simultaneous Azimuth and Fresnel Elevation Compounding: A Fast 3-D Imaging Technique for Crossed-Electrode Arrays (Study 1 – Chapter 3)

The objective of the first study was to demonstrate a bias-controllable elevation lens on a 10 MHz, electrostrictive crossed electrode array. It was hypothesized that coherently compounding the result of a set of Fresnel mimicking bias patterns would improve the focus generated in the elevation dimension. Furthermore, the study demonstrated that the imaging in the azimuth dimension could be improved simultaneously with the elevation focus. The imaging was demonstrated on a prototype 10 MHz array using a Verasonics Ultrasound System with custom biasing electronics.

1.1.2 A 30 MHz, 3D Imaging, Forward-Looking Miniature Endoscope based on a 128-element Relaxor Array (Study 2 – Chapter 4)

The objective of the second study was to develop a fabrication process that facilitates packaging a high frequency crossed electrode array into an endoscopic form factor (6 mm x 5 mm). The hypothesis for this study was that the development of new fabrication techniques would result in a crossed electrode array packaged into a miniaturized form factor with high element yield, broad

pulse bandwidth and low element-to-element crosstalk. The study characterizes the array performance and evaluates the switching performance of the electrostrictive ceramic. The imaging technique described in Study 1, SAFE compounding, was used to demonstrate imaging performance.

1.1.3 A New 3D Imaging Technique Integrating Ultrafast Compounding, Hadamard Encoding, and Reconfigurable Fresnel Lensing (Study 3 – Chapter 5)

In the final study, a new imaging technique is described and demonstrated. It was hypothesized that employing elevational Hadamard encoding on receive, combined with the Fresnel lens on transit would improve the elevational image quality. The Hadamard coding can be implemented using the electrostrictive ceramic by applying a pattern of positive and negative biases, matching a row of a Hadamard matrix. After decoding, we gain the RF data for each element across the elevation aperture even though there is effectively only one channel in that dimension. Using the decoded data, a synthetic receive aperture can be built. The objective of this study was to describe the imaging technique and demonstrate the performance on the 30 MHz endoscope from Study 2.

1.2 Summary of Chapters

Chapter 2 presents background related to the design and performance of ultrasound arrays, 2D ultrasound arrays and developments relating to crossed

electrode arrays, bias-sensitive transducer materials and clinical applications of 3D ultrasound.

Chapter 3 (Study 1) describes the fabrication of the prototype crossed electrode array and the novel imaging technique called Simultaneous Azimuth and Fresnel Elevation (SAFE) compounding. This chapter gives some context for what is meant by bias-controlled imaging and background for Fresnel lenses. We demonstrate the ability to focus in elevation by controlling the polarization direction across the aperture and the improvement in the focus by coherently compounding multiple insonifications. This chapter was published in IEEE Transactions on Ultrasonics, Ferroelectrics and Frequency Control under the title "Simultaneous Azimuth and Fresnel Elevation Compounding: A Fast 3-D Imaging Technique for Crossed-Electrode Arrays"

Chapter 4 (Study 2) describes the miniaturization of a forward-looking, 30 MHz, crossed electrode array into an endoscopic form factor. The fabrication method and array characterization are highlighted, and imaging performance is demonstrated using SAFE compounding. This chapter was accepted for publication in IEEE Transactions on Ultrasonics, Ferroelectrics and Frequency Control under the title "A 30 MHz, 3D Imaging, Forward-Looking Miniature Endoscope based on a 128-element Relaxor Array".

Chapter 5 (Study 3) introduces a new imaging technique that uses a Fresnel mimicking lens in elevation on transmit and uses bias-controlled Hadamard

encoding on receive. The imaging technique is demonstrated using the 30 MHz endoscope array and results are compared to simulation. This chapter was submitted and is under review in IEEE Transactions on Ultrasonics, Ferroelectrics and Frequency Control under the title "A New 3D Imaging Technique Integrating Ultrafast Compounding, Hadamard Encoding, and Reconfigurable Fresnel Lensing"

Chapter 6 summarizes the conclusions and presents future work based on the results of the previous chapters. Improvements to the imaging techniques are explored as well as potential applications for similar low channel count, bias-sensitive devices.

1.3 Statement of Contributions

In Study 1, I was responsible for developing and simulating the elevation lens imaging techniques. During the development of the imaging techniques, I was presenting author at two conferences which each have accompanying proceedings papers [1], [2]. The content of these papers is not in the work presented in this thesis but show important steps in developing the elevational lens imaging approach. I fabricated the 10 MHz crossed electrode array which included making the composite and integrating it into an interconnect board and packaging. The imaging experiments for this array were performed at the University of Alberta (Dr. Roger Zemp's lab) using a Verasonics beamforming

system and custom biasing electronics developed for capacitive micromachined ultrasonic transducers (CMUTs). This started a collaboration on projects using the 10 MHz electrostrictive crossed electrode array and resulted in contributing authorship on two publications [3], [4] and several conference presentations. For the work presented in Study 1 (Chapter 3), I was the first author of the journal article [5] and conference proceedings [6]. I also contributed to a patent application based on the imaging approach [7].

In Study 2, I was responsible for the design, fabrication and testing of the 30 MHz endoscopic crossed electrode array. This work is presented in a journal article (accepted but not yet published) and conference presentation and proceedings [8]. The other authors supported the work by contributing ideas to the fabrication techniques and developing the dynamically controllable biasing electronics.

In Study 3, I was responsible for the design, simulation and implementation of the new bias-controllable imaging scheme. The imaging performance is demonstrated using the array design from Study 2 in a conference presentation and proceedings [9] and an expanded journal article is submitted and is under review.

CHAPTER 2
BACKGROUND

In a simple ultrasound system, a single piezoelectric element is excited, expands and contracts and creates a pulsed pressure wave. The transmitted ultrasound energy into the medium is referred to as an insonification. The piezoelectric element then receives any echoes that have been generated from scattering targets in the field of view. The pressure from the propagating echoes hits the transducer and an electric signal is generated due to the piezoelectric effect. The strength of the scatterer (or brightness) is related to the amplitude of the electric signal while the depth of the scatterer is encoded in the time stamp of the received pulse. The RF signal received by a transducer creates one image line called an A-scan (Figure 2-1 a)). To improve the ability to resolve small structures and generate high-quality images the emitted ultrasound energy must be focussed. A conventional way to focus is to progress from a single piezoelectric element to a linear array of elements, a concept similar to RF antenna arrays. In this configuration, each element can be excited at a different time and the relative delays can be chosen such that the resulting beam is steered in addition to being focussed. With this type of array, called a phased array, a 2D sector-shaped scan is built up by steering to a different image line for each

insonification. By convention, the elements of a 1D array are along the azimuthal direction (shown in Figure 2-1 b)), therefore, it creates a 2D image in the azimuthal plane. Thus, another degree of freedom is required for 3D imaging. Generally, 3D ultrasound systems consist of either a mechanically scanned 1D array or a 2D array. Volumetric images are built by either physically moving the 1D array to produce a series of elevation image slices or by electronically focusing and steering a 2D array (Figure 2-1 c)). Mechanical scanning is limited by a low frame rate because the physical motion required to capture the image increases acquisition time. The drawn-out acquisition time can result in motion artifacts reducing image quality. Furthermore, this technique also suffers from poor spatial resolution in the elevation direction (direction of mechanical motion) since the elevation lens is only weakly focused. These disadvantages are inherent to the technique and have not been overcome with technical innovation [10], [11].

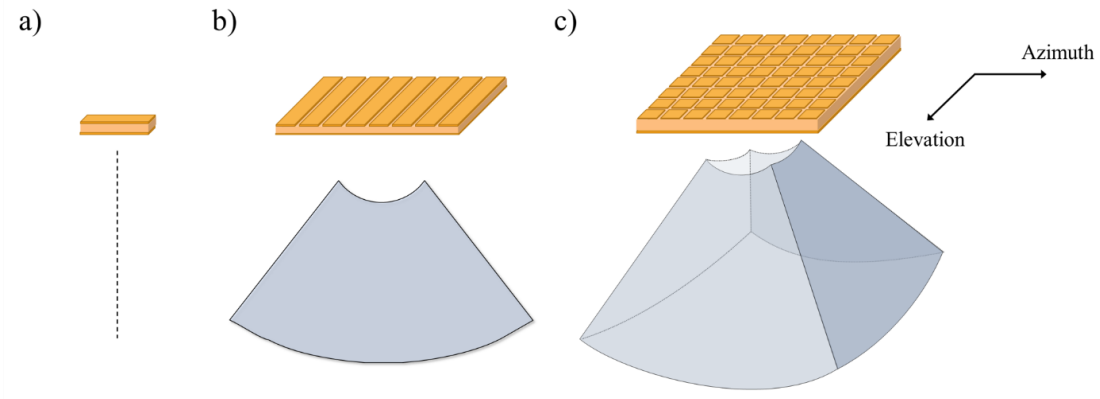

Figure 2-1 The progression of increasingly complex transducer architectures and their imaging capabilities: a) the single image line created with a single element transducer, b) the 2D image created with a 1D phased array and 3) the 3D volume image created with a 2D grid array.

There are significant challenges that arise when scaling up a linear 1D array to a conventional 2D array, both in the fabrication and operation of the devices. To summarize, the thousands of very small elements required present challenges in forming the electrical connections to each element. The driving electronics must scale with element count and quickly become impractical in size and cost. Considering the operation of the array, imaging a very large field of view with high quality, high frame rate images present its own set of challenges. For this reason, the array design presented in this dissertation considers the whole 3D ultrasound system, including the transducer material and architecture, the supporting imaging methods and the system electronics.

A further discussion of transducer design and materials, imaging methods, 2D arrays and 3D ultrasound is completed in the following sections of the chapter. The focus is on unconventional approaches to volumetric imaging that successfully reduce channel count and maintain image quality.

2.1 Transducer Design

The basic architecture of a piezoelectric transducer consists of a resonant active layer, a backing layer and a set of matching layers (Figure 2-2). The thickness of the active layer is chosen to be equal to half a wavelength ($\lambda/2$) in the material to create resonance at the desired operating frequency. The speed of

sound in the piezoelectric material, c, gives the antiresonance frequency at a transducer thickness using the formula for a wavelength.

$$\lambda = \frac{c}{f} \tag{2-1}$$

An alternate measure is the thickness mode frequency constant, N_t, that relates the resonance frequency to the thickness of the material.

When acoustic waves encounter a material with a different characteristic impedance some energy is reflected and some transmitted depending on the difference in impedance between the two materials. Acoustic matching layers can be used to improve the transfer of energy out of the front face of the transducer and into the load medium. Piezoelectric materials generally have a high acoustic impedance (~30 MRayl) and tissue has a low acoustic impedance (1.5 MRayl). An acoustic matching layer can be used similarly to an electrical matching circuit to improve the power transmission into the medium. A simple single layer

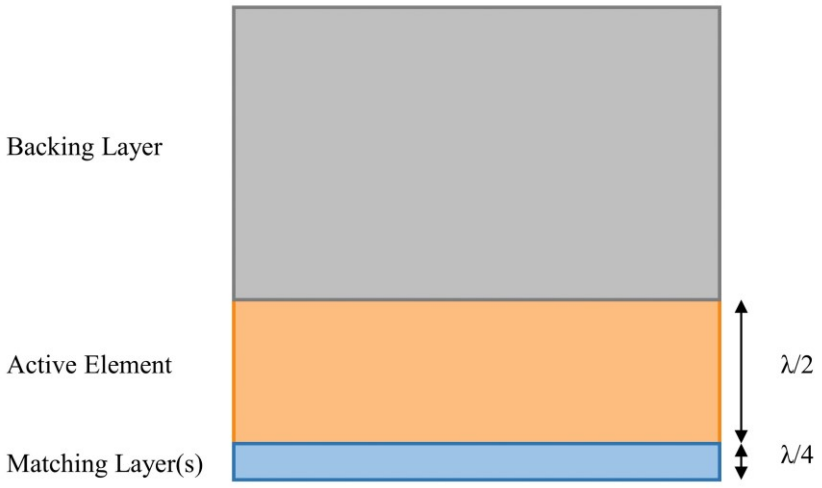

Figure 2-2 Acoustic stack of a typical transducer including the active piezoelectric layer, the attenuative backing layer and a quarter wavelength matching layer.

matching design consists of a quarter wavelength layer using a material with an acoustic impedance that is equal to the geometric mean of the two mediums.

$$Z_2 = \sqrt{Z_1 Z_3} \tag{2-2}$$

Under these conditions, the transmission coefficient is equal to 1. This example of a matching layer is tuned to the resonance frequency of the active element. More complex, multilayer designs are employed to match a broad range of frequencies and improve the pulse bandwidth. A common formula used to determine single quarter length matching layers for broadband operation is given by Desilets et al. [12],

$$Z_2 = (Z_1 {Z_3}^2)^{1/3}, \tag{2-3}$$

Two or three matching layer designs are often used to improve pulse bandwidth and transducer sensitivity.

The backing layer serves a practical function of providing rigidity to the acoustic stack and it is also important in the acoustic operation. Generally, the backing layer is made from dense, attenuating material. This absorbs the energy transmitted into the backing layer and provides damping to the resonator. In an acoustic backing design, there is a trade-off between bandwidth and sensitivity. If a very high acoustic impedance backing is chosen, the pulse will have very high bandwidth because any energy reflected off the front of the transducer is well matched to the backing and is quickly attenuated. However, the transducer's sensitivity suffers when energy is lost to the backing layer.

2.1.1 Piezoelectric Materials

The property of piezoelectricity was first described by Jacques and Pierre Curie in 1880. They observed the generation of electrical charge in crystals, such as quartz, after the application of pressure. The phenomenon was named piezo from the Greek word meaning "to press". An understanding of the internal structure of the material is necessary to explain this electromechanical relationship. The perovskite structure is a subset of crystal structures that is of importance because a large group of ferroelectric ceramics manufactured exhibit this structure. A typical perovskite unit cell has an ABO_3 structure as shown in Figure 2-3. When an electric field is applied to the unit cell, the central ion (e.g. Ti^{4+} or Zr^{4+}) moves in the direction of the field, shifting the charges and leading to an elongation of the structure. Because ceramic is made up of many of these

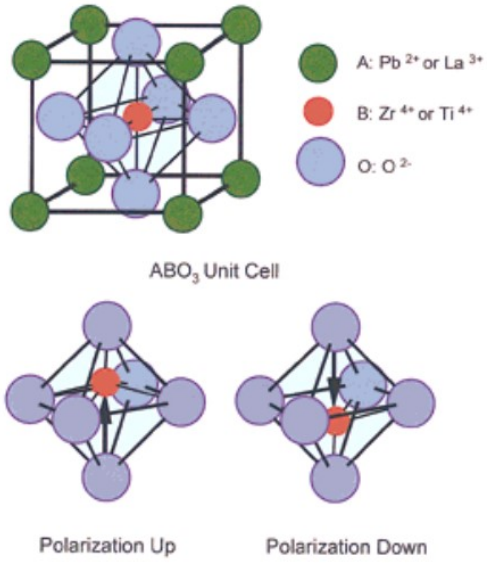

Figure 2-3. Perovskite ABO_3 unit cell for PZT, illustrating 180° polarization reversal for two of the six possible polarization states produced by displacement of the central cation in the tetragonal plane. Reprinted with permission from [13].

unit cells or crystallites in random orientation and the movement is bound by the crystallographic structure, the direction of movement only approximates the electric field [13]. The hallmark of all piezoelectric materials is this non-centrosymmetric structure. Single crystal can be grown in this manner while piezoceramics need to be poled. The randomly oriented domains of a ceramic are aligned in a DC electric field at an elevated temperature just below its Curie temperature. When the field and temperature are removed from piezoceramics, most of the domains remain fixed in near alignment. The poling steps are shown in Figure 2-4. The polarization that remains is often called remnant polarization and is imperative to the performance of the ceramic as a piezoelectric. Thermal de-poling occurs when the material is heated above its Curie temperature.

The piezoelectric effect is the term used to define the electromechanical phenomenon seen in this specialized group of materials with non-centrosymmetric

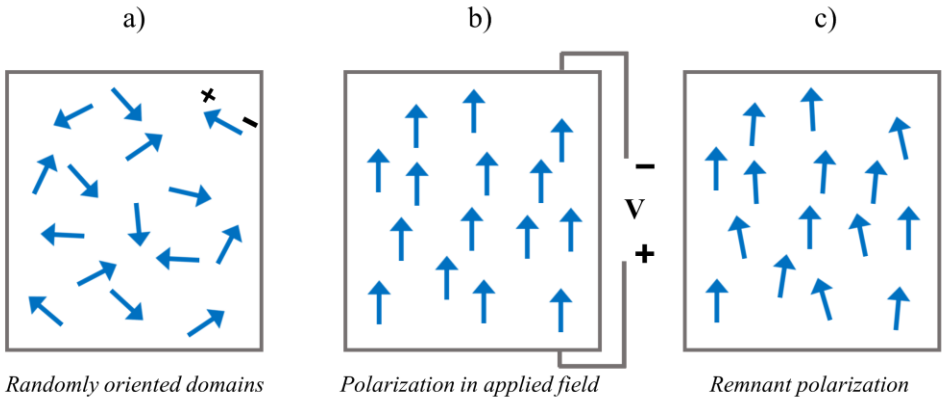

Figure 2-4. Steps to pole a piezoelectric ceramic, a) the material begins with randomly oriented domains, b) an electric field is applied along the axis of polarization with heat, c) after the field is removed the domains remain mostly aligned. Redrawn and modified based on [181].

structures. In the direct piezoelectric effect, a force on the material creates a potential difference. The stress on the material rotates the internal dipoles or domains, creating the potential difference (Figure 2-5 (c)). In this mode, the piezoelectric medium acts as a sensor. The direct piezoelectric effect can be described mathematically as,

$$D = dT \tag{2-4}$$

Where the charge per unit area or electrical displacement, D, is related to the applied stress, T, through a piezoelectric constant, d (units of C/N). The indirect effect describes the strain in the medium in response to an applied electric field

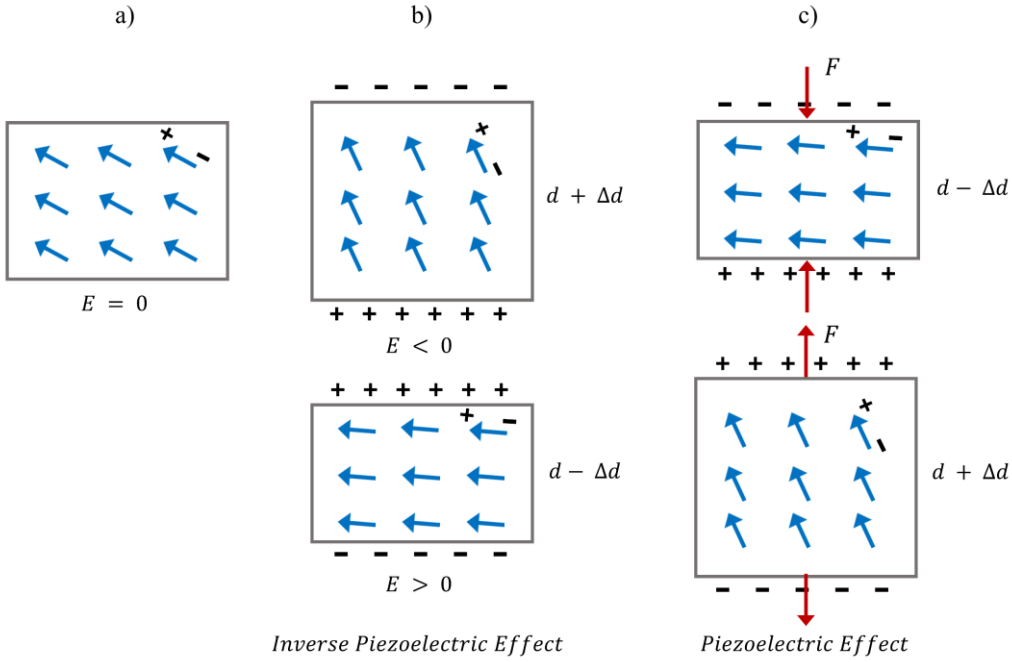

Figure 2-5. Simplified diagram of a piezoelectric medium, a) in equilibrium, (b) with an applied electric field resulting in a rotation of the dipoles demonstrating the inverse effect and, (c) under a force that creates a strain in the medium and induces polarization illustrating the direct piezoelectric effect. Redrawn and modified from [11].

(Figure 2-5 (b)). In this mode, the piezoelectric medium acts as an actuator. The direct piezoelectric effect can be described mathematically as,

$$S = dE \tag{2-5}$$

where the deformation of the material or strain, S, is related to the applied electric field, E, through the piezoelectric constant, d (this time expressed in units of m/V). The piezoelectric constant is numerically the same when describing both the direct and indirect piezoelectric effect [11], [14], [15].

Piezoelectricity describes the linear coupling between electric and elastic forces. A set of constitutive equations are used to relate the stress (T), strain (S), electric field (E) and dielectric displacement (D). The equations shown in the previous section (Eq. (2-4) and Eq. (2-5)) describe the relationship between the electrical and mechanical components. To fully describe the medium, we must also account for the purely elastic and purely electric mechanisms. Hooke's law relates the stress and strain through an elastic constant, s (units of $1/(\mathrm{N/m^2})$).

$$S = sT \tag{2-6}$$

We can also relate the electric field displacement to the strength of an applied electric field through the dielectric permittivity, ε (units of F/m).

$$D = \varepsilon E \tag{2-7}$$

If we combine both the terms for both the direct and indirect piezoelectric effect, we get a set of constitutive equations [11], [15].

$$\boldsymbol{S = s^E T + dE, \quad D = dT + \varepsilon^T E} \tag{2-8}$$

However, this is only one representation of the equations. Three other equation pairs give the relationships between the different electromechanical variables.

$$\begin{gathered} \boldsymbol{T = c^E S - e^t E, \quad D = eS + \varepsilon^S E} \\ \boldsymbol{S = s^D T + g^t D, \quad E = -gT + \beta^T D} \\ \boldsymbol{T = c^D S - h^t D, \quad E = -hS + \beta^S D} \end{gathered} \tag{2-9}$$

These relations assume the medium is anisotropic, homogenous and under isothermal conditions. Because the piezoelectric medium is anisotropic, the elastic, dielectric and piezoelectric properties are orientation dependent. For this reason, electrical and mechanical variables as well as the elastic, dielectric and piezoelectric constants must be expressed as matrices. A common notation convention has been adopted for these equations. The stress (T) and strain (S) are represented by a 3x3 matrix, including the normal and shear components. Because it is assumed that the material is in equilibrium, the opposite shear components are equal, and the matrix can be reduced to a 6-element column. The electric field (E) and electric displacement (D) can be expressed as 3-element matrices, one component for each direction.

$$\boldsymbol{T} = \begin{bmatrix} T_{11} & T_{12} & T_{13} \\ T_{21} & T_{22} & T_{23} \\ T_{31} & T_{32} & T_{33} \end{bmatrix}, \tag{2-10}$$

$$T_1 = T_{11}, T_2 = T_{22}, T_3 = T_{33}\ (normal\ stress\ components)$$

$$T_4 = T_{32} = T_{23}, T_5 = T_{13} = T_{31}, T_6 = T_{12}$$
$$= T_{21}\,(shear\ stress\ componets)$$

The piezoelectric coefficients are also second rank tensors, and all have two subscripts in the form x_{ij}. The subscripts represent an electrical/mechanical force applied in the jth direction and the electrical/mechanical response in the ith direction. By convention the direction subscript 3 refers to the poling axis. The coefficient matrices represent partial derivatives and, therefore, have boundary conditions associated with them. The conditions are indicated in the coefficient's superscript. The constants are evaluated at constant stress, constant electric field, constant electric displacement or constant strain representing free, short circuit, open circuit or clamped boundary conditions, respectively [14]. The t superscript indicates a matrix transpose operation. Any set of elastic, dielectric and piezoelectric constants can be used to fully describe the system and a different set can be obtained from straightforward matrix operations [11].

For piezoceramics, the matrices can be significantly simplified by considering symmetries in the crystal structure. The subscript 3 is used to describe the poling axis and this direction acts as an axis of symmetry. Many coefficients can become zero or are equal to the coefficients in corresponding directions. The large matrices of property coefficients can be reduced to just ten independent values. The matrix notation for one set of the constitutive equations is shown in Eq. (2-11).

$$\begin{bmatrix} S_1 \\ S_2 \\ S_3 \\ S_4 \\ S_5 \\ S_6 \\ D_1 \\ D_2 \\ D_3 \end{bmatrix} = \begin{bmatrix} s_{11}^E & s_{12}^E & s_{13}^E & 0 & 0 & 0 & 0 & 0 & d_{31} \\ s_{12}^E & s_{11}^E & s_{13}^E & 0 & 0 & 0 & 0 & 0 & d_{31} \\ s_{13}^E & s_{13}^E & s_{33}^E & 0 & 0 & 0 & 0 & 0 & d_{33} \\ 0 & 0 & 0 & s_{44}^E & 0 & 0 & 0 & d_{15} & 0 \\ 0 & 0 & 0 & 0 & s_{44}^E & 0 & d_{15} & 0 & 0 \\ 0 & 0 & 0 & 0 & 0 & s_{66}^E & 0 & 0 & 0 \\ 0 & 0 & 0 & 0 & d_{15} & 0 & \varepsilon_{11}^T & 0 & 0 \\ 0 & 0 & 0 & d_{15} & 0 & 0 & 0 & \varepsilon_{11}^T & 0 \\ d_{31} & d_{31} & d_{33} & 0 & 0 & 0 & 0 & 0 & \varepsilon_{33}^T \end{bmatrix} \begin{bmatrix} T_1 \\ T_2 \\ T_3 \\ T_4 \\ T_5 \\ T_6 \\ E_1 \\ E_2 \\ E_3 \end{bmatrix} \quad (2\text{-}11)$$

2.1.2 Electrostrictive Materials

An example of a bias sensitive transducer material is an electrostrictive ceramic. The previous section on piezoelectricity described the linear electromechanical effects in ferroelectrics ceramics. Electrostriction is another electromechanical effect that describes a mechanical deformation in response to an electric field. In the case of electrostriction, the strain is proportional to the square of the electric field and is independent of the direction of the field. Electrostriction is not limited to materials with a certain structural symmetry. All dielectric materials exhibit some electrostriction, but the effect is usually small and often can be ignored. The electrostrictive effect is large in a group of materials called relaxor ferroelectrics. These materials have very high dielectric and electrostrictive constants [13]. For this dissertation relaxor ferroelectric and electrostrictive material will be used interchangeably.

In contrast to the piezoelectric effect, the electrostrictive effect does not require a prior alignment of the medium domains (a remnant polarization) to be

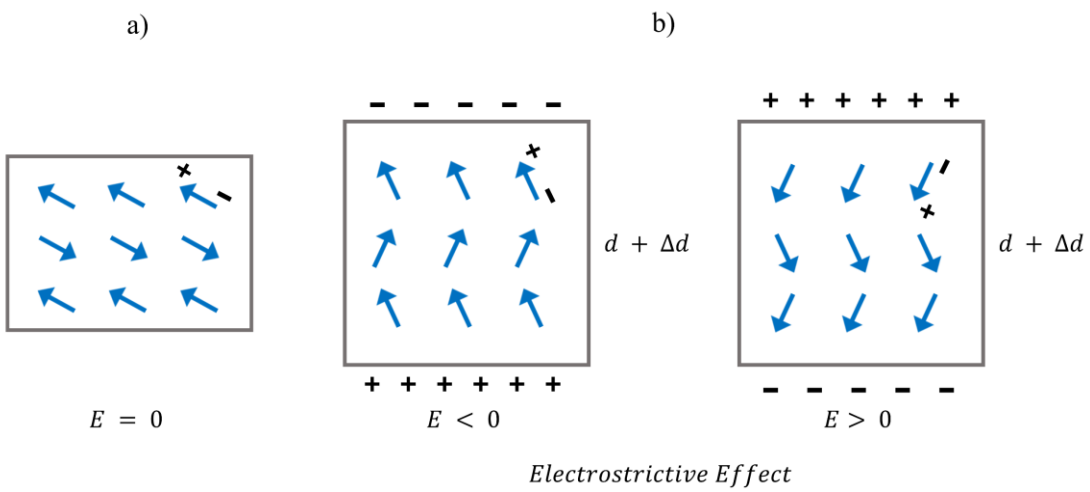

Figure 2-6 Simplified diagram of an electrostrictive medium, a) in equilibrium and (b) with an applied electric field resulting in a rotation of the dipoles and a strain proportional to the square of the electric field illustrating the electrostrictive effect. Redrawn and modified from [11].

demonstrated. If an electrostrictive medium is in equilibrium and an electric field is applied, the electric dipoles rotate in line with the field and a strain is produced. The same strain will be produced when the direction of the field is reversed. There is no inverse electrostrictive effect. Stress on the medium does not result in a change in polarization (Figure 2-6) [11]. The electromechanical relationship can be expressed in terms of the square of the electric field or square of the polarization as,

$$S = ME^2 = QP^2 \tag{2-12}$$

where M and Q are the electrostrictive coefficients used for the electric field and polarization, respectively. The simple conversion between M and Q is as follows [15].

$$M = (\varepsilon^T)^2 Q \tag{2-13}$$

Electrostrictive ceramics can provide a strain due to the electrostrictive effect alone. However, for applications like ultrasound transducers, it is necessary to take advantage of the piezoelectric effects of the ferroelectric ceramic that are present when biased. In this mode of operation, the electrostrictive effect is used to induce the polarization necessary for piezoelectricity. Figure 2-7 highlights the field dependence of piezoelectricity and electrostriction. An applied bias induces a strain and, therefore, polarization in an electrostrictive material.

The linear set of constitutive equations describing piezoelectricity does not capture this new effect. The second-order term will need to be included in the electromechanical relationship, where previously we assumed these terms to be negligible. We can now describe the strain in terms of stress and electric field as,

$$S = s^E T + dE + ME^2 \tag{2-14}$$

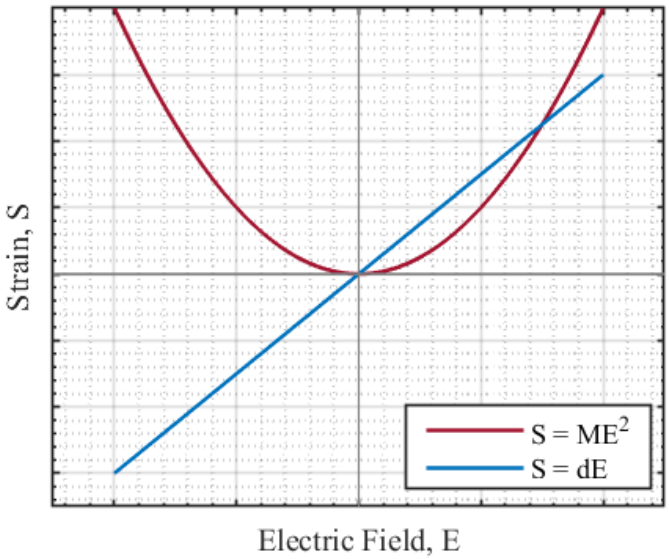

Figure 2-7 Illustration of the strain dependence on electric field for electrostriction and piezoelectricity. Redrawn and modified from [182].

where the first term describes Hooke's law, the second term describes the indirect piezoelectric effect and the final term describes the electrostrictive effect [15], [16]. Similarly, there are higher-order terms for the electric displacement equation. However, since electrostriction does not have an inverse effect the extra terms are not necessary to capture this behaviour [16], [17]. Both the DC and AC portions of the electric field must be considered when operating an electrostrictive ceramic in a biased piezoelectric mode. The behaviour of these ceramics is not as straightforward as the simple change to the strain equation suggests. Like piezoceramics, the performance depends on the polarization in the material. But, the polarization in electrostrictive ceramics changes with the bias field. The piezoelectric constant in the poling direction can be expressed as [13], [18], [19],

$$d_{33} = 2\varepsilon_{33}Q_{11}P_3 \tag{2-15}$$

Thus, the higher the electric field, the higher the piezoelectric effect until the material polarization saturates. The effective piezoelectric constants, dielectric permittivity constants and elastic constants change with polarization. Figure 2-8 shows the change in these coefficients with the electric field for a common electrostrictive ceramic, PMN-PT (lead magnesium niobate-lead titanate). Because of the complicated behaviour, there is a body of research focused on measuring the electromechanical coefficients over a range of polarization conditions and fitting the results to higher-order polynomials [20]–[23]. For the

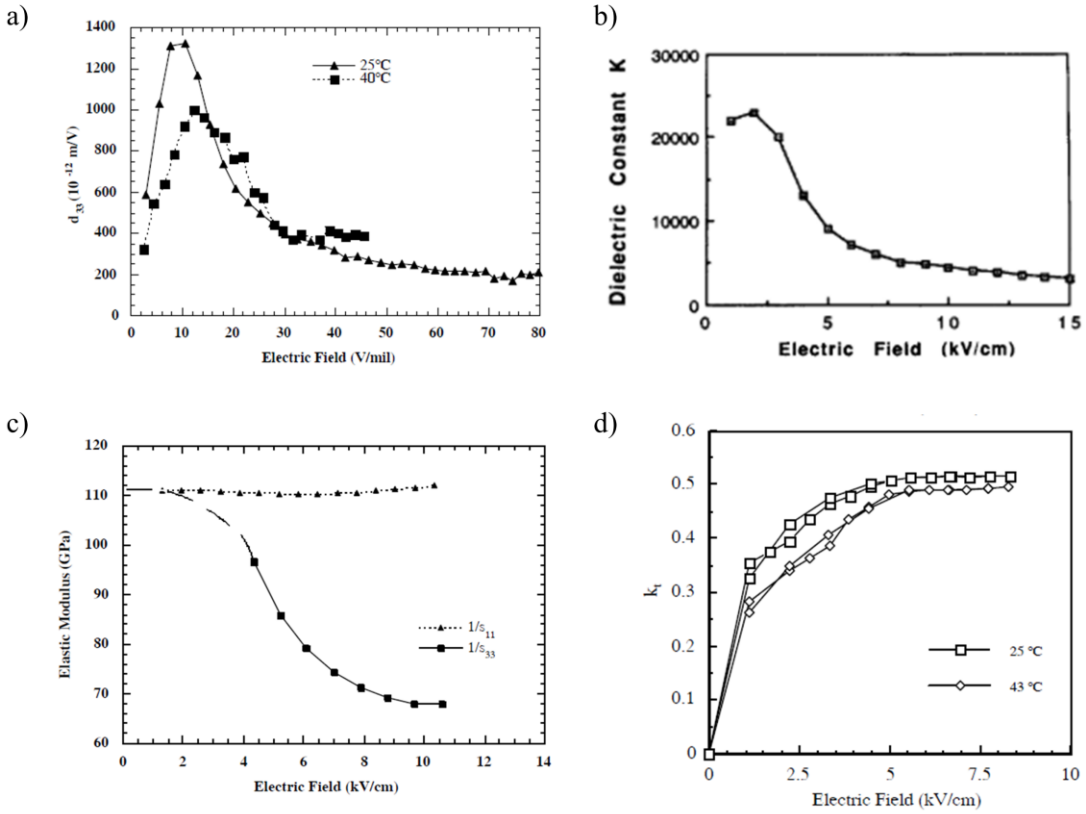

Figure 2-8 Illustration of experimental measurements of PMN-PT highlighting the piezoelectric dependence on bias field, (a) piezoelectric coefficient, d_{33}, (b) dielectric constant, $\varepsilon_{33}/\varepsilon_0$, (c) elastic coefficients, s_{11} *and* s_{33} and (d) the resulting electromechanical coupling factor, k_t (1kV/cm = 2.54 V/mil). Reprinted from [24], [129]. © 1990 IEEE.

transducer design in this project, piezoelectric properties at peak polarization were estimated and used in the transducer model.

Relaxor ferroelectrics are characterized by their diffuse phase transition and the dependence of the dielectric constant on frequency. This means the ferroelectric exhibits a large electrostrictive effect over a relatively wide temperature range. The dielectric constant peaks at the Curie maxima (T_m) and decays slowly with increasing temperature. Figure 2-9 shows the contrasting behaviour of a relaxor ferroelectric and a conventional ferroelectric ($BaTiO_3$). In

the curve for the conventional ferroelectric, the dielectric constant is low in the operating range and there is a sharp transition at the Curie temperature ($T_C \cong 125^0C$). This is the point where the spontaneous polarization would be lost [19], [24]. This high, diffuse dielectric peak is a large advantage for relaxor ferroelectrics ($K > 25000$) but it is also important to consider the frequency and temperature dependence on the performance. As was shown in the last chapter, high permittivity increases piezoelectricity. One additional benefit of a high dielectric constant is reduced electrical impedance.

The second advantage of electrostriction is the minimal hysteresis seen in the strain-electric field curves. In a conventional piezoelectric ceramic, the amount of strain measured depends on the strength of the electric field and whether it is increasing or decreasing. The strain produced from the electrostrictive effect is

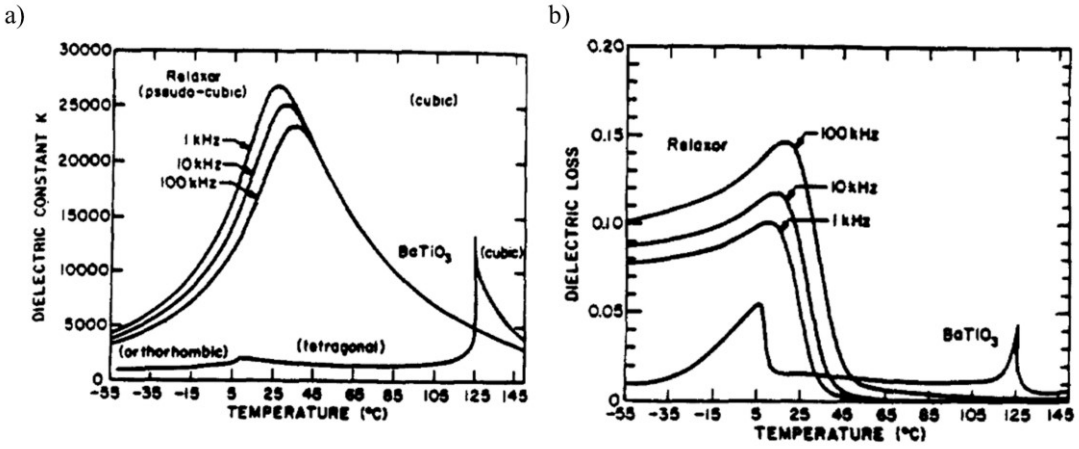

Figure 2-9 Typical dielectric behaviour of a relaxor ferroelectric (PMN-PT) compared with a normal ferroelectric, a) dielectric constant and b) dielectric loss. Reprinted from [24] © 1990 IEEE..

stable and reproducible. In addition, the size of the strain can be even larger than that produced using the piezoelectric effect [25].

The mechanisms behind the operation of relaxor ferroelectrics are not fully understood. The prevailing theory is an inhomogeneous micro-domain model. The combination of the high, diffuse dielectric peak and the minimal hysteresis is attributed to the random and disordered arrangement of Mg and Nb in the B-site of the perovskite structure (see Figure 2-3). The random groups throughout the material each have different Curie temperatures, therefore, in the presence of an electric field, the material can easily be polarized over a range of temperatures. The random arrangement returns when the electric field is removed (i.e. no remnant polarization and little hysteresis) [19].

Because of these advantages over other ferroelectrics, electrostrictive ceramics have been used in high strain (>0.1%) actuators [26], deformable mirrors [27] and high dielectric (K > 25000) capacitors [28]. These ceramics are also suitable for use in tunable piezoelectric transducers, especially for high frequency, 2D addressable arrays [19], [29]–[31].

2.1.3 Capacitive Micromachined Ultrasonic Transducers

An alternative approach to creating bias sensitive transducers is a completely different method for ultrasound generation. These devices are called capacitive micromachined ultrasonic transducers (CMUTs). CMUTs were first developed in

1996 [32] and have more recently been integrated into commercial ultrasound systems by Hitachi [33]. The fabrication is based on existing silicon fabrication methods which can be transitioned to a large, batch process for commercialization.

CMUTs consist of thin, conductive membranes suspended with a gap between the membrane and a conductive silicon wafer. The two conductive, parallel plates behave as a capacitor. A schematic of a typical CMUT is shown in Figure 2-10 a). The void between the membrane and bottom wafer is often evacuated to avoid electrical breakdown and mechanical effects from air loading the backside of the membrane [34]. On transmit, electrostatic forces, provided by an AC voltage, vibrate the membrane. A DC bias voltage must be used to counter the unipolar electrostatic force (Figure 2-10 b)). Without the DC bias,

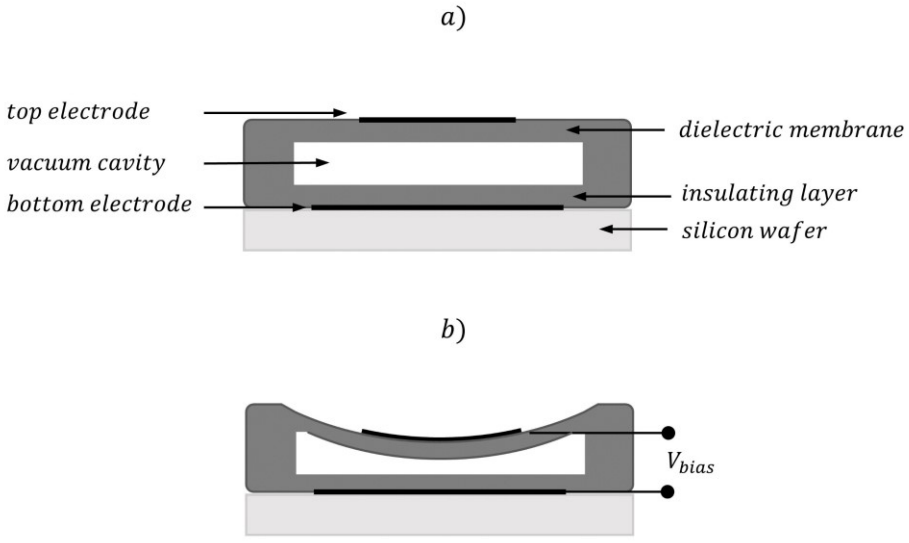

Figure 2-10. Diagram of CMUT cell structure a) without a bias and b) biased for operation. Redrawn and modified from [183]

the membrane would vibrate at effectively twice the operating frequency since the force would be always attractive. The vibration of the membrane produces acoustic pressure waves in the medium. CMUTs operate similarly on receive. An incident pressure wave causes a DC biased membrane to vibrate, the change in distance between the parallel plates causes the capacitance to change. The modulation in current is the received electrical signal. CMUT cells operating in immersion act as non-resonant devices because the membrane is mechanically loaded and damped [35]. The DC bias has a limit for correct operation. When the DC bias is applied the membrane is pulled toward the silicon substrate. If the electrostatic force pulling the membrane down overcomes the restoring force of the membrane, the membrane will collapse onto the bottom substrate. This threshold voltage is called the collapse voltage.

One of the advantages of CMUT technology is its ability to very efficiently convert between electrical and mechanical energy. The electromechanical coupling coefficient relates physically to the size of the gap between the membranes and the amount of deflection (controlled by the DC bias) [36], [37]. Figure 2-11 a) shows the electromechanical coupling as a function of bias voltage. The coupling approaches unity as the bias approaches the collapse voltage. These devices are usually operated at a coupling coefficient of approximately 0.8.

In conventional piezoelectrics, the acoustic impedance is determined by the properties of the material. In general, the acoustic impedance of water/tissue is

much larger than the characteristic impedance of the membrane material. For CMUT cells the membrane has an impedance, modelled as an LC resonant structure. So, for frequencies where the membrane impedance is small compared to the medium impedance, most of the mechanical force appears across the load impedance [36]. Figure 2-11 b) shows the membrane impedance as a function of frequency. The immersion bandwidth is taken as the point where only half of the mechanical force is transmitted into the medium (i.e. when the membrane impedance matches the immersion medium impedance). In water, these devices are inherently very broadband ($> 100\%$).

For CMUT devices the transmit sensitivity is in direct opposition with receive sensitivity. In contrast, the piezoelectric effect is largely equal on transmit and receive. To evaluate the sensitivity on receive, the smallest membrane deflection which registers a detectable change in the capacitance must be

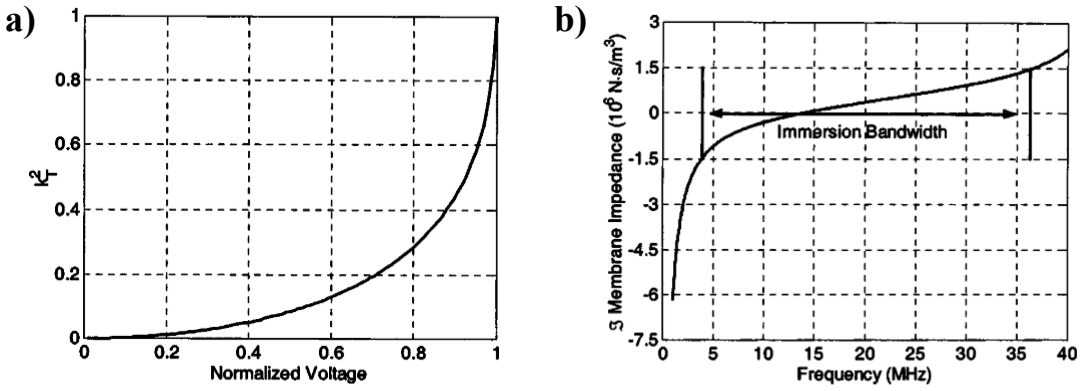

Figure 2-11 Illustration of the performance of CMUTs including a) the electromechanical coupling coefficient as a function of bias voltage normalized to the collapse voltage and b) the mechanical impedance of a typical CMUT element designed for operation in the 5-35MHz range in water. Reprinted from [36] with permission from ASCE.

determined. In this mode a small gap height is desirable. The transmit sensitivity is a measure of pressure out given a pulsed drive voltage. Now it is desirable to have a large gap height to maximize membrane movement [34]. This unfortunate trade-off has been a major motivation for much of the ongoing CMUT research and development.

In a typical CMUT cell, the overall spacing between the parallel membranes is in the range of 1-12 µm, which is hundreds of times smaller than the thickness of a piezoceramic transducer. The dielectric constant is much lower (~1000x) for CMUTs, therefore, overall the capacitance is much smaller, and the impedance is large. As a result, CMUT elements require electrical matching to the electrical source [35], which can be prohibitive in many large element count design.

For reasons including transducer sensitivity and electrical impedance, positive/negative pulse symmetry and inhouse equipment and expertise, CMUTs were not chosen for the work in this dissertation.

2.1.4 Transducer Modelling

The behaviour of piezoelectricity and electrostriction is complex. Comprehensive models have been developed that can predict the behaviour of each part of an ultrasound transducer from the backing material, to the piezoelectric resonance, to any number of acoustic matching layers. The most commonly adopted model is called the KLM model, named with the initials of its

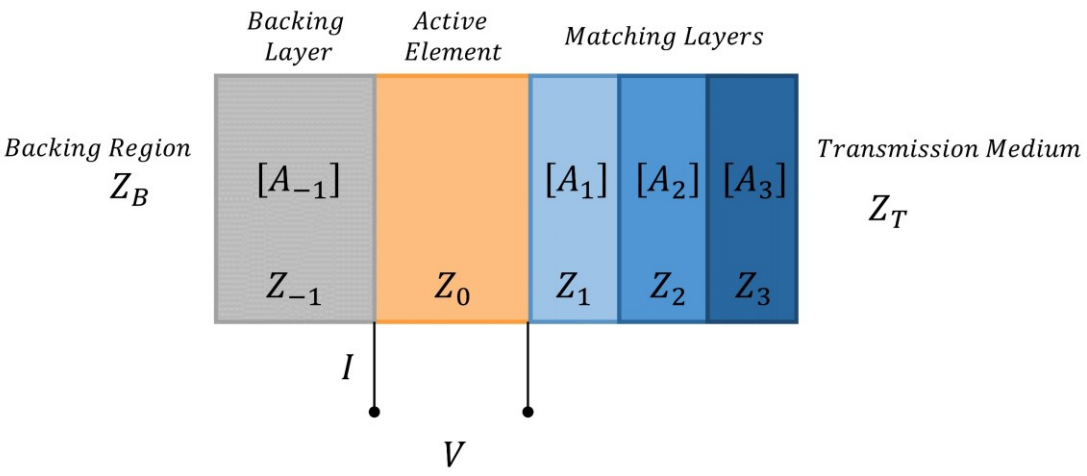

Figure 2-12 A transducer with multiple cascaded acoustic layers. Redrawn and modified from [11].

inventors [38]. KLM is a 1D model in which the transducer element is modelled with three ports, one electrical port and two acoustic ports. The rest of the transducer layers (i.e. backing medium, backing layer, matching layers, transmission medium) are modelling as a series of cascaded two-port networks where each layer is defined by its transmission matrix (Figure 2-12).

The total transmission matrix is the multiplication of the individual transmission matrices defining each acoustic layer in series. This model is easily scalable as layers can be added, removed or edited by just acting on the corresponding transmission matrix.

2.1.5 Transducer Performance Metrics

There are many ways to evaluate the performance of an ultrasound transducer. The most relevant metrics for this project are summarized here.

Electromechanical Coupling Coefficient (k)

The electromechanical coupling coefficient is a measure of the transducer's efficiency in converting electrical energy to mechanical and vice versa (which is equal by reciprocity). This coefficient is a dominant contributor to the transducer sensitivity. The electromechanical coupling coefficient is calculated differently depending on the shape of the resonator and the chosen boundary conditions (changing the piezoelectric, dielectric and elastic coefficients used). For example, for a resonating pillar (thickness >> length, width) with an electric field applied in the poling direction, the value k_{33} is used and is calculated with the following equation [25], [39].

$$k_{33} = \frac{d_{33}}{\sqrt{s_{33}^E \varepsilon_{33}^T}} \tag{2-16}$$

A different measure, k_t, is used to evaluate the efficiency of a piezoelectric plate (length, width >> thickness) that is clamped laterally and operating in thickness mode.

$$k_t = \frac{e_{33}}{\sqrt{\varepsilon_{33}^S c_{33}^D}} \tag{2-17}$$

When evaluating the performance of a fabricated transducer, the electromechanical coupling is confirmed by measuring the resonant frequency (f_r) and anti-resonant frequency (f_a) and using Eq. (2-18) [40].

$${k_t}^2 = \frac{\pi f_r}{2f_a} \cot\left(\frac{\pi f_r}{2f_a}\right) \tag{2-18}$$

Bandwidth

The bandwidth of a transducer determines the image resolution in the axial direction. A wide bandwidth pulse is desired to shorten the pulse in the time domain and increase resolution. The bandwidth of the active substrate can be approximated as the inverse of the electrical quality factor [40]. However, the backing layer and matching layers play a large role in the bandwidth produced by the acoustic stack. The beamwidth is measured from the frequency spectrum of the pulsing using the following formula,

$$BW = \frac{f_h - f_l}{f_c} \tag{2-19}$$

Where f_h and f_l are the upper and lower frequency thresholds of the spectrum. For a one-way pulse, the frequency thresholds are measured at -3 dB and for a two-way pulse, the threshold is moved to -6 dB. The frequency in the centre of the spectrum is given by f_c. Bandwidth is normally expressed as a percentage of the center frequency.

Electrical Impedance

Electrical matching, or mismatching, between the driving source electronic and the electrical impedance of the transducer is an important design consideration. If the impedances match, the electrical energy transfer is efficient.

The real part of the electrical impedance at resonance (R_A) can be calculated as follows,

$$R_A = \frac{2{k_t}^2}{\pi^2 f_0 C_0} \tag{2-20}$$

where f_0 is the operating frequency and C_0 is the clamped capacitance of the transducer.

$$C_0 = \frac{\varepsilon^S A}{d} \tag{2-21}$$

The electrical impedance is one example of why it is desirable to have a large clamped dielectric constant. A higher clamped capacitance leads to lower electrical resistance. At high frequencies, array elements become very small in area and, unless the dielectric constant is very high, have a very large impedance making matching to the cabling system difficult [41].

2.1.6 Composite Materials

Composite materials are used in transducer design to tune material properties. Piezocomposites generally consist of piezoelectric ceramic combined with a softer epoxy component. The structures of piezocomposites vary and include a regular grid of piezoelectric pillars, randomly sized piezoelectric rods or ceramic grains embedded in epoxy. Figure 2-13 shows two common composite structures often made with a dice and fill method, a 2-2 composite and a 1-3 composite. For example, the 1-3 composite is made by dicing kerfs into the

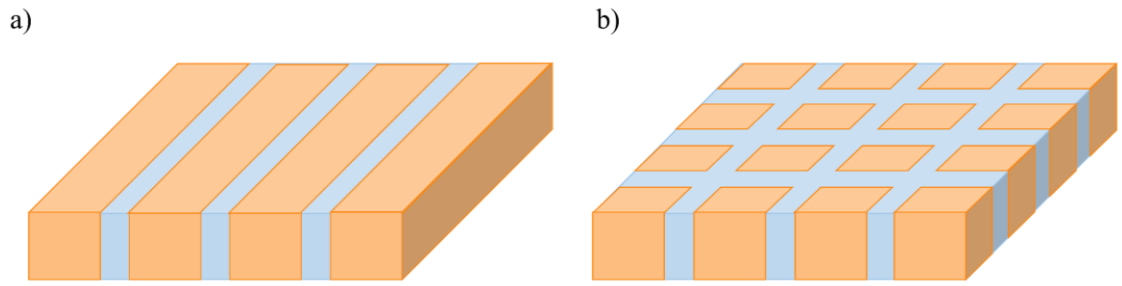

Figure 2-13 Diagrams of example composites showing a) a 2-2 composite and b) a 1-3 composite.

ceramic in the x and y direction. This leaves a grid of square pillars on a base of solid ceramic. The kerfs are filled with epoxy and the excess epoxy on top and ceramic on the bottom is lapped away to finish the composite. By convention, the first number in the type name indicates the number of connectivity directions (x, y, z) that the piezoceramic is continuous. The second number corresponds to the number of directions the epoxy is continuously connected and not interrupted by ceramic.

There are two main advantages of a composite that increase the performance of an ultrasound transducer. First, the high percentage of epoxy significantly lowers the acoustic impedance of the composite compared to a solid piezoelectric ceramic. Therefore, the acoustic impedance of the array is more closely matched to tissue and can eliminate the need for more than one matching layer to achieve acceptably broad bandwidth. Second, the piezoceramic is no longer clamped laterally, thus, it operates more efficiently in pillar mode. The electromechanical coupling coefficient of composite material is significantly higher

than bulk ceramic operating in plate mode (k_t approaches k_{33}) [42]. Additional tangential advantages to composites include decreased element-to-element crosstalk in piezocomposite arrays, increased element directivity and increased bendability for curved designs. Smith and Auld [43] have described a model for redefining the constitutive equations for a piezoelectric composite. From this model, we can plot the transducer performance metrics as a function of ceramic volume fraction. Figure 2-14 shows the effect of volume fraction on the

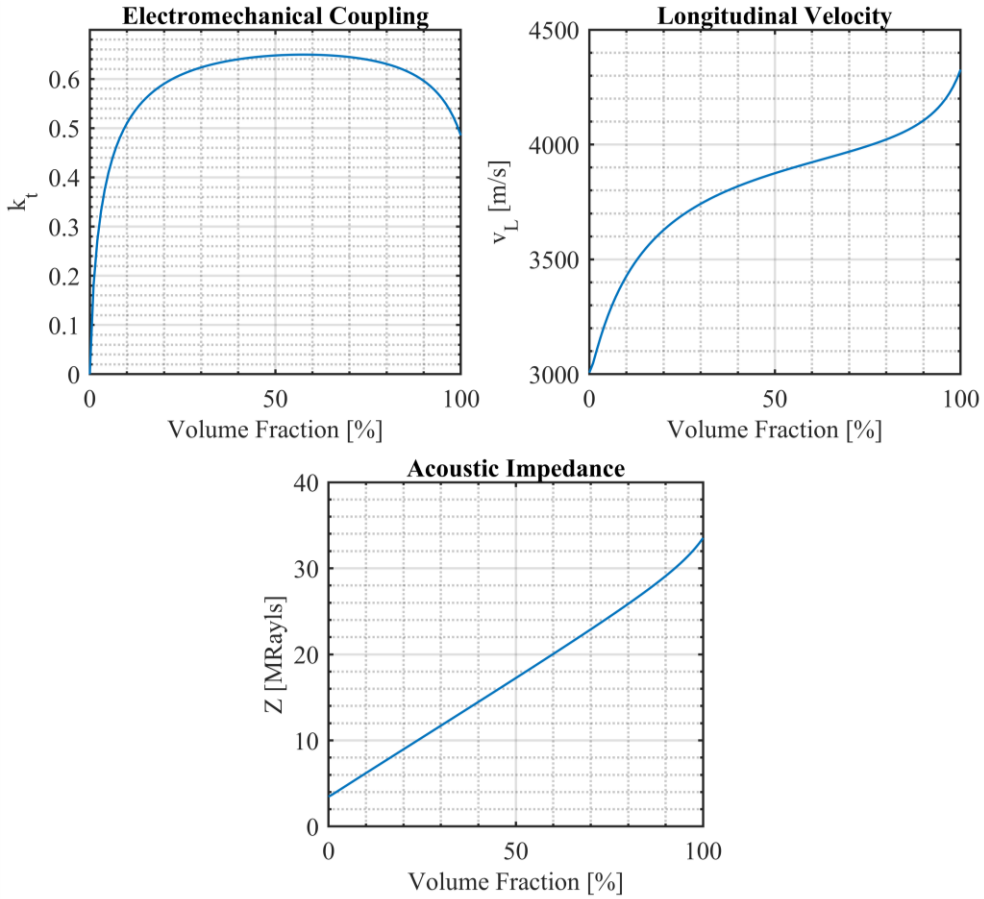

Figure 2-14 Design example showing the changing in electromechanical coupling, longitudinal velocity and acoustic impedance with piezoelectric volume fraction, This example uses PZT 5H and EPO-TEK 301 epoxy as example composite materials in a 30 MHz 1-3 composite. Recreated with method in [43].

electromechanical coupling, longitudinal speed of sound and acoustic impedance of the resulting composite.

The scale of the composite must be sufficiently fine to avoid lateral and spurious modes through the epoxy. At high frequencies, the scale of the composite structure introduces fabrication challenges. At frequencies greater than 30 MHz the composite kerf width must be less than 7 μm to push the lateral modes through the epoxy outside the operating bandwidth of the composite. The pillar height to width aspect ratio must also be sufficiently high (ideally >4), however, the kerf width tends to be the limiting dimension and causes challenges with high frequency composite fabrication.

2.2 Imaging Techniques

A high-quality 2D image requires the ultrasound energy to be focussed and steered through the imaging field of view. This is accomplished with an array of ultrasound transducer elements with time delays applied across the array. The body of work aimed at developing and refining beamforming approaches is vast. Therefore, the following section discusses only a few relevant beamforming techniques for understanding the new techniques developed in this dissertation.

2.2.1 Conventional Beamforming

In conventional beamforming, or delay and sum beamforming, the beam is focussed to a single imaging line on transmission and reception. In a linear array, a delay profile is applied to a sub-aperture of elements, focussing directly in front of the centre of the sub-aperture. The RF data collected for each image line is called an A-scan. The active sub-aperture electronically translates down the array, shifting the location of the imaging line. Each line contributes to a rectilinear image. A phased array generally has fewer array elements than a linear array because the whole array is active for each imaging line. The imaging line is shifted by changing the steering angle, building up a sector shaped image. Figure 2-15 shows the delay profile changing as the beam is steered. When the full set of A-scans for the image is collected, the envelope is taken, and the amplitude values are converted to gray scale values. The 2D map of the greyscale values is a B-mode or brightness mode image.

The delay value for each element in the aperture is a simple time of flight calculation from the element (n) to the focal location (x, z).

$$\tau_n = \sqrt{z^2 + (x - x_n)^2}/c \tag{2-22}$$

where x_n is the location of the element n and c is the speed of sound in tissue. The delay profile gives a single transmit focal location. The depth of focus can be extended by using multiple transmit focal zones and stitching together the image from multiple acquisitions of a given line. However, the frame rate decreases by a

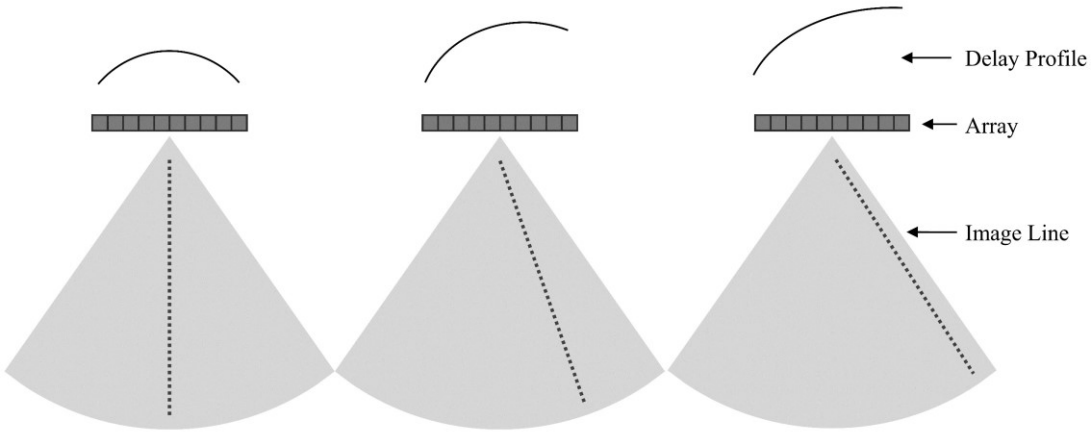

Figure 2-15 Diagram illustrating the line by line acquisition of conventional beamforming.

factor equal to the number of transmit focal zones. The focus can be improved on receive because it is not limited to a fixed point per insonification. The delay profile can also be adjusted so that the received signal from each depth is delayed by the appropriate value. This is called dynamic receive beamforming.

2.2.2 Ultrafast Imaging

Conventional beamforming can achieve real-time frame rates; however, the speed is not adequate to capture transient movement (e.g. for cardiac imaging or shear wave propagation) or large fields of view. In the field of ultrafast imaging frame rate of greater than 1000 Hz can be achieved.

In synthetic aperture imaging, the number of required insonifications is driven by the number of aperture elements rather than the number of imaging lines and transmit focal zones. To build a synthetic aperture image the transmit/receive response from individual element pairs is recorded and used to focus and reconstruct the image afterward. Figure 2-16 shows a simple example of

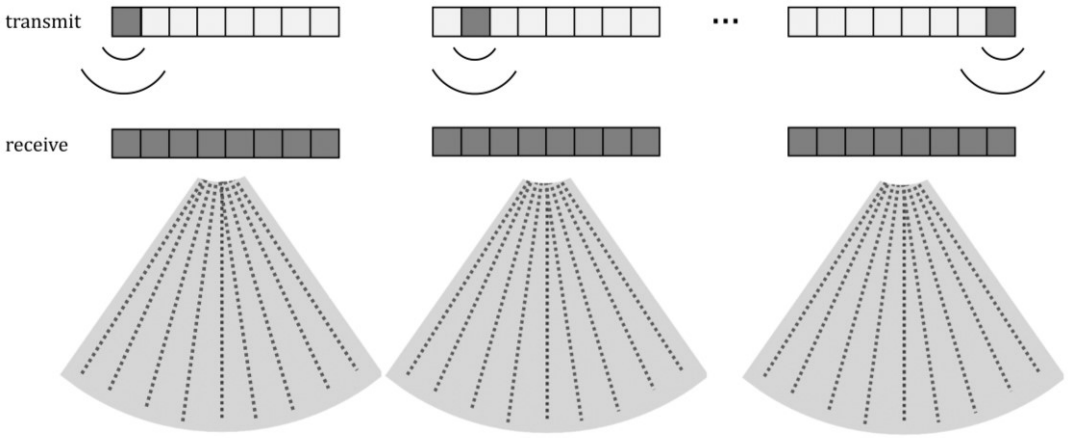

Figure 2-16 Diagram of a synthetic aperture scheme where each element is used to transmit one at a time and all receive elements are active. After each transmit-receive event a low quality image is formed and the low resolution images can be combined to create a high resolution image. Redrawn and adjusted from [11].

synthetic aperture imaging where each element is used to transmit in turn and all elements are used on receive. After each transmit-receive event, a low-quality image is formed based on the beamforming delays for the active transmit element. The process is repeated and the low-resolution images can be combined to create a high-resolution image [11]. This technique has the added advantage that the image is in focus at every pixel with no need to sacrifice frame rate. Synthetic aperture, however, can suffer from poor SNR since only a small portion of the aperture is active at a time.

Synthetic aperture imaging can be further sped up by employing a sparse synthetic aperture approach described by Lockwood et al. [44]–[46]. A sparse synthetic aperture approach uses the idea that the effective total aperture is the convolution of the transmit aperture with the receive aperture. Designing a sparse imaging technique using the effective aperture approach can greatly reduce the

number of insonifications required while maintaining the radiation pattern. For example, sparse periodic apertures can be used on transmit and receive and, if they are chosen with the effective aperture in mind, the grating lobes will occur at different locations and the effect will cancel out.

Another way to perform ultrafast ultrasound imaging is coherently compounding plane or diverging waves. Like single-element synthetic aperture imaging, a low-quality image can be created by transmitting a single plane wave that insonifies the full field of view. The dynamic beamforming on receive can build a one-way focussed image. The image quality is improved by building up a transmit focus by transmitting a series of angled plane waves (Figure 2-17). The received data for each plane wave has a different interference pattern from the scatterers. Each image is transmit/receive beamformed based on the angle of the plane wave (i.e. the distance the wave travels to each image pixel and back).

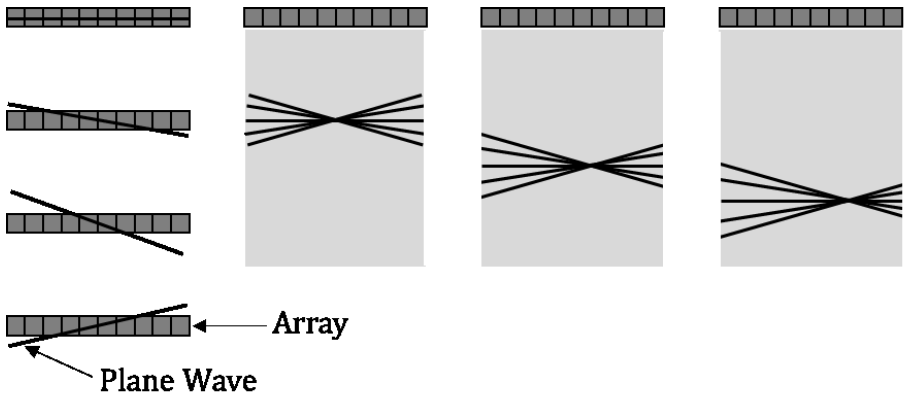

Figure 2-17 Diagram illustrating plane-wave imaging. A series of individual plane waves insonify the field of view. The received data can be synthetically transmit focussed throughout the field on view. The compounded result is a higher quality image focussed on transmit and receive. Redrawn and modified from [47].

When the images are coherently compounded a high-quality image is formed [47]. This type of full aperture compounding technique has an SNR advantage over synthetic aperture imaging. Images can theoretically be generated much faster as well, the image quality can be weighed against frame rate to suit a clinical application. The directivity of this plane-wave technique, however, is very limited as most of the energy is transmitted within the bounds of the array aperture.

Alternatively, a set of diverging waves can be used to achieve similar results with a much larger field of view for an equivalent aperture (Figure 2-18). A virtual point source is synthetically created behind the array and moved along with a corresponding sub-aperture for each insonification [48]. Like for plane-wave imaging, each insonification originates from a new viewpoint and

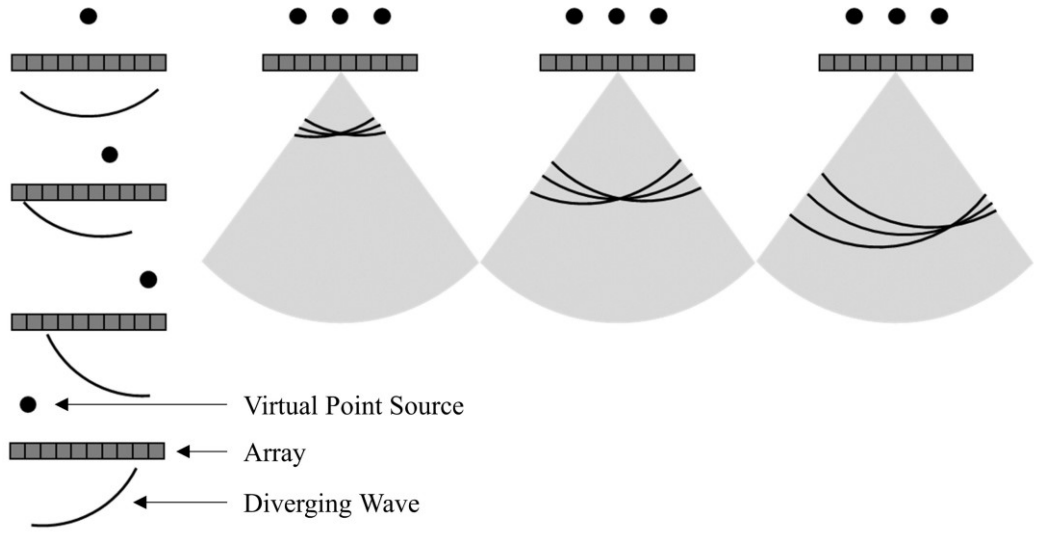

Figure 2-18 Diagram illustrating diverging wave imaging. A series of individual diverging waves insonify a large field of view. Each diverging wave is changed by moving a virtual point source behind the array. The received data can be synthetically transmit focussed. The compounded result is a higher quality image focussed on transmit and receive. Redrawn and modified from [48]

contributes to the synthetic transmit focus. These examples of coherent compounding techniques are advantageous in 3D imaging because the frame rate is decoupled from the number of lines in the image.

Hadamard based coding has also been used in various forms in ultrasound imaging largely to improve SNR as an alternative to traditional synthetic aperture imaging [49]–[52]. More recently, and more relevant to this dissertation, it has been used to provide a transmit elevation focus on crossed electrode arrays [53], [54]. Figure 2-19 illustrates how Hadamard coding works on transmit. A Hadamard matrix is made up of entries equal to +1 or -1 with the property that each row is mutually orthogonal. When the elements across an aperture are

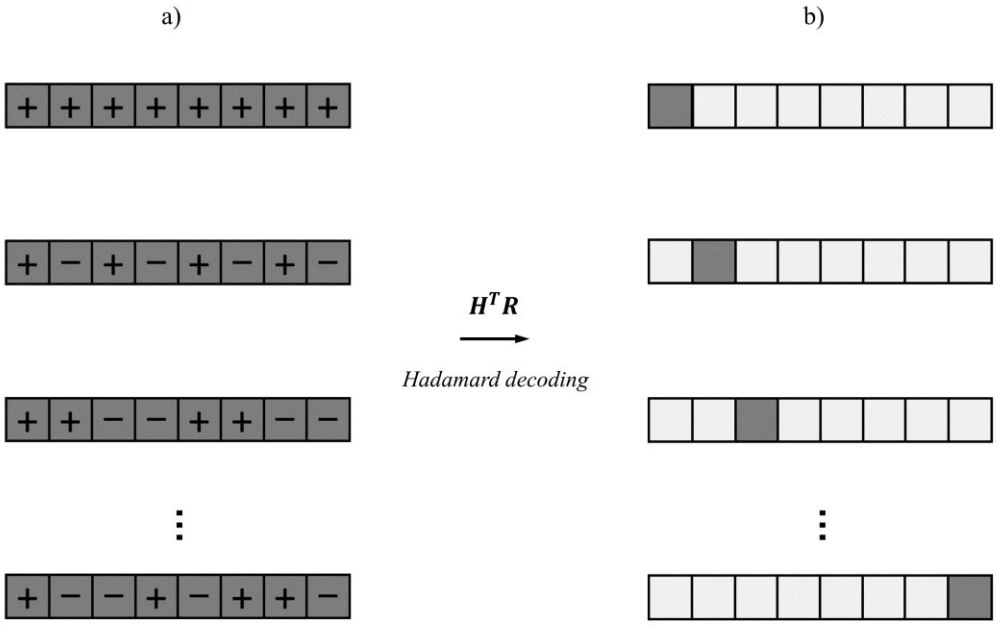

Figure 2-19 Diagram illustrating a Hadamard coded synthetic transmit aperture, s) Hadamard codes are applied across the transmit aperture, the received signals are decoding and b) the result is the data as if only a single transmit element was active at a time (scaled by a factor of N).

Hadamard encoded (given either a positive or negative polarity, Figure 2-19 a)) we can perform a simple matrix calculation on the set of received data to decode and retrieve the equivalent of the RF data from each element across the array (Figure 2-19 b)) by multiplying by the transpose of the Hadamard matrix. The decoding step uses the properties of orthogonal matrices. The transpose of an orthogonal matrix multiplied by the matrix is equal to an identity matrix with a gain term.

$$\boldsymbol{H^T H = nI} \tag{2-23}$$

The received data can be represented as,

$$\boldsymbol{HT\Phi = R} \tag{2-24}$$

The Hadamard matrix multiplied by a diagonal transmit pulse matrix, $\boldsymbol{T}$, and the field transfer matrix, $\boldsymbol{\Phi}$. The received data and transmit pulse matrices are time dependent. In the case where no transmit delays are applied, the diagonal entries of the transmit pulse matrix are identical, having the same amplitude at the same time point. The field transfer matrix is the two-way transfer function from a transmit element through the field and back to each receive element. Therefore, multiplying both sides of Eq (2-25) by the Hadamard transpose gives the field transfer matrix along with the transmit delay information for each element,

$$\boldsymbol{nIT\Phi = H^T R} \tag{2-25}$$

This decoded data is equivalent to synthetic transmit aperture data. It contains data received by element n as if only element m was active on transmit. The

decoded matrix contains the received data for all transmit-receive element pairs represented by Eq. (2-26).

$$\boldsymbol{H^T R = R_D} = \begin{bmatrix} \boldsymbol{R_{D1,1}} & \cdots & \boldsymbol{R_{D1,N}} \\ \vdots & \ddots & \vdots \\ \boldsymbol{R_{DN,1}} & \cdots & \boldsymbol{R_{DN,N}} \end{bmatrix} \tag{2-26}$$

Hadamard transmit coding provides a $\sqrt{n}$ improvement in SNR over conventional synthetic aperture techniques, where n is the number of rows in the Hadamard matrix. The number of required insonifications is still the number of elements in the aperture. Samson et al. [52] and Ceroici et al. [53] showed that the frame rate using a Hadamard approach can be increased by grouping elements and assigning the same polarization direction (i.e. using fewer rows of the Hadamard matrix). The degradation in image quality caused by increasing the effective pitch can be mitigated with beamforming techniques [52], but signal to noise is still decreased with fewer insonifications.

2.2.3 Field Modelling

Field II is a spatial impulse response simulation package used widely in ultrasound research [55], [56]. The software uses the approach outlined in [57] (based on concepts developed in [58]–[60]) to calculate the spatial impulse response of an arbitrarily shaped transducer. The program splits the total aperture into small mathematical elements and sums the response from each to

give the total aperture response. The spatial impulse response represents the emitted field at a given location and point in time in response to a delta function excitation. The field for any excitation is calculated by convolving the excitation function with the transducer impulse response and the spatial impulse response. This package makes it easy to define an array of ultrasound elements in any geometry, set time dependent apodization and delay profiles and analyze emitted pressure patterns or test new imaging techniques. All of the field simulations for this project were completed with Field II.

2.2.4 Imaging Performance Metrics

The response of the imaging system to a perfect point target (a radiation pattern or point spread function) is used to determine many of the performance measures of the transducer and the imaging technique. An example point spread function along the azimuth direction of a 1D phased array is shown in Figure 2-20. The example array operates at 40 MHz, with 64 elements at wavelength pitch. The focus was set at 6 mm (f-number of 2.5).

Lateral Resolution

The width of the central main lobe determines the lateral resolution or the ability to differentiate point targets side by side. The main lobe beamwidth,

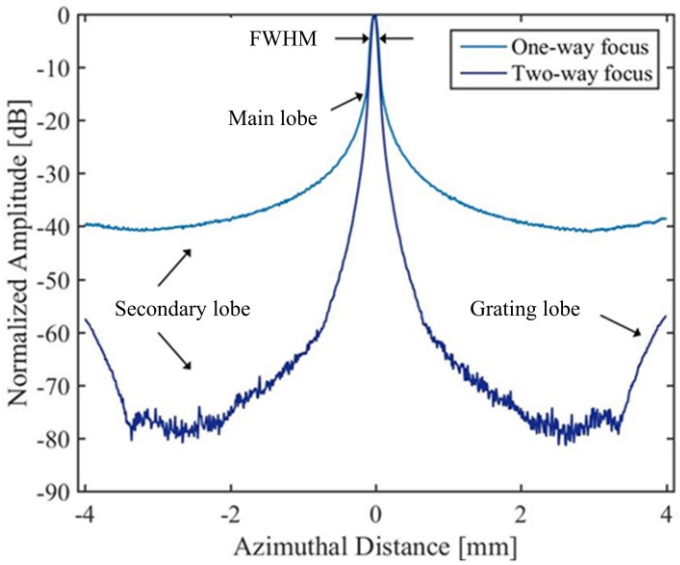

Figure 2-20 Example simulated results of one-way and two-way radiation patterns of a focussed phased array. Important features (secondary lobe level, main lobe and main lobe beamwidth or FWHM) are labelled.

$FWHM_{lat}$, is measured as the width of a two-way point spread function at -6 dB. The beamwidth can be estimated by,

$$FWHM_{lat} = \lambda F = \lambda \frac{z}{D} \tag{2-27}$$

where λ is the pulse wavelength, F is the f-number of the focus which is the ratio of the focal length (z) to aperture width (D).

Axial Resolution

The axial resolution determines the ability to differentiate point targets along the depth axis. The axial resolution can be measured at the -6 dB width of the envelope of an imaging line. As pulse bandwidth is increased, the axial resolution

is improved, and the pulse enveloped is shortened. The axial resolution can be approximated by,

$$FWHM_{ax} \cong \frac{1}{p} * \frac{\lambda}{BW} \tag{2-28}$$

where p is a proportionality constant that considers the shape of the pulse envelope. This can be measured experimentally, however, for a typical pulse, the value will be approximately 3.5.

Dynamic Range

To either side of the main lobe there is undesirable sensitivity we refer to as secondary lobes. The difference between the main lobe and secondary lobe level directly impacts the maximum dynamic range of the final image. If the secondary lobes are only 30 dB below the main lobe any signal from tissue at or below this level will be buried in the secondary lobe clutter. In Figure 2-20, a curve for a one-way focus as well as a two-way focus is plotted to illustrate the significant difference in energy in the secondary lobes for the two cases. In a one-way focus, the secondary lobes only decrease to -40 dB compared to the almost -80 dB of a two-way focus. In addition, the main lobe is broadened in the one-way focus case. This drastic difference in the secondary lobe level with a two-way focus will be important when comparing current 3D imaging techniques.

Signal to Noise Ratio

The signal to noise ratio (SNR) is the ratio of the signal generated by the tissue scatterers and the noise floor inherent to the system. Once noise sources have been mitigated, the best ways to improve SNR is to maximize the sensitivity of the transducer and consider the active aperture and beamforming technique.

Frame Rate

Another key consideration for an ultrasound imaging technique is the frame rate. It is most often required for a clinical ultrasound system to be capable of real time frame rates ($\geq 30\,Hz$) and for some functions much higher frame rates are necessary. The frame rate (FR) is given by the formula

$$FR = \frac{PRF}{N_{txrx}} = \frac{PRF}{N_L * N_t} \tag{2-29}$$

where the pulse repetition frequency (PRF) is the safe repetition rate based on the time required for a pulse to propagate from the array to the largest depth in the image and back. The frame rate is then reduced by the number of insonifications (N_{txrx}) required to build the image. In a conventional beamforming system, there would be N_L pulses corresponding to the number of imaging lines and that would be repeated N_t times for the number of transmit focal zones. When considering more complex imaging techniques determining the number of insonifications is not necessarily as straight forward. For our high

frequency (30 MHz) case and an 18 mm imaging depth, the pulse repetition frequency would be 40 kHz. Therefore, an imaging scheme could require 1300 insonifications and still generate real-time volume images (30 Hz).

Element Directivity

In an ideal model, each transducer element in an array acts like a perfect point source and emits a perfectly spherical wave but that is not the case in reality. The directivity measures the element's ability to radiate or receive energy in a specific direction. The smaller the array element, the more it acts as a point source and the wider the directivity function. A wide element directivity is desirable because more energy is insonifying the region and more elements will contribute to the focus. The lateral directivity function for an element is given by

$$D(\theta) = sinc\left(\frac{wsin(\theta)}{\lambda}\right) \tag{2-30}$$

and the angle range at FHWM is approximately [11],

$$\theta_{FWHM} = 2\sin^{-1}\left(\frac{0.6\lambda}{w}\right) \tag{2-31}$$

where w is the width of the element and λ is the wavelength in the medium.

Crosstalk

In an array of ultrasound elements some signal can be induced on an element due to the excitation of a neighbouring element. Beamforming becomes very difficult and image quality suffers if the element crosstalk is high. The signal crosstalk can be attributed to both electrical causes (i.e. neighbouring traces on

an interconnect circuit) or acoustic causes (i.e. the neighbouring element producing an acoustic pulse). The causes of the crosstalk are difficult to decouple, and a combined value of crosstalk is measured.

2.3 Two-Dimensional Arrays

Volumetrics Medical Imaging, Inc., in partnership with Duke University, created the first real-time 3D ultrasound system in 1998. Today, all the large ultrasound manufacturers offer volume imaging products (e.g. GE, Philips, Siemens, Fujifilm). An example transducer that highlights the capabilities of current 2D arrays is the xMATRIX array by Philips (Philips Medical Systems, Bothell, WA, USA). This 2D array can be operated in multiple modes. The array generates a conventional pyramidal scan with the size adjustable by the user. In the alternate modes, the imaging is either completed in two orthogonal planes or in a single plane that can be electronically rotated for faster acquisition (Figure 2-21). The software allows for many different image display and data sectioning

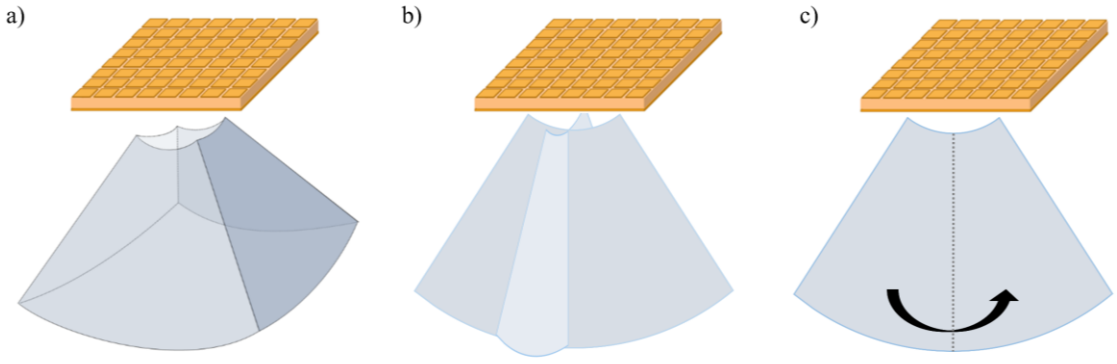

Figure 2-21. An illustration of a selection of modes of a fully sampled array, a) pyramidal scan b) a biplane image (two orthogonal planes) and c) electronic rotation of the 2D image.

options. The flexibility makes the probe appropriate for a wide variety of volume imaging applications.

2.3.1 Fully Sampled 2D Arrays

A fully sampled 2D array is the gold standard for comparison of 3D ultrasound techniques. An ideal 3D capable ultrasound array is a fully sampled square 2D array with $\lambda/2$ element pitch in both directions with the elements laid out in a grid. The energy from the array can be beam steered throughout the volume of interest, creating a two-way focus in the elevation direction and azimuth direction. A fully sampled 2D array requires a separate electrode and connection for each element in the array. For a square array, the number of electrical connections increases by a factor of the number of elements in the analogous 1D array (N^2 compared with N). The electronic channels that support the transmit and receive functions increase by the same factor. For example, to achieve the same resolution as a 128 element 1D array, a 2D array would have 16,384 elements. Building such an array is challenging, and even infeasible, for several reasons. In addition to the incredible fabrication challenges, the electrical impedance of the elements increases inversely with element size. The small elements required in a 2D array would have prohibitively high impedance, complicating the electronics interfacing with the transducer and most likely leading to a reduction in transmitted and received signal strength. Even the

thickness of the cabling for thousands of channels makes such an array impractical.

The challenges associated with fabricating a conventional 2D array are amplified at high frequencies. The element size scales inversely with frequency, making the physical fabrication require finer tolerances, element interconnections more difficult and the impedance mismatch even higher. Moreover, packaging into an endoscopic form factor is virtually impossible with thousands or tens of thousands of elements, at least with known microelectronic packaging technology.

Before fabricating fully sampled matrix arrays, sparse 2D arrays were designed. A sparse array is designed with only a small subset of elements active. Thus, reducing the number of connections significantly. Generally, sparse arrays have challenges with signal strength and secondary lobe levels because the active elements are a very small percentage of the array and are spread out over the aperture with large element to element pitch.

The first real-time 3D ultrasound imaging system was developed by researchers at Duke University [61], [62]. The original system used sparsely activated 2D arrays that create a pyramidal scan. The imaging system was limited in the number of available beamforming channels and sparsely activating the array was a solution to the system complexity. Previous work by Shattuck et al. [63] was leveraged to achieve real-time volume frame rates. The technique developed by Shattuck et al. uses parallel processing in a method called

Explososcan imaging to increase the acquisition rate for 2D imaging. In the Explososcan technique a broad transmit beam insonifies a region in the field of view allowing multiple receive imaging lines to be captured. The frame rate increases by a factor of the number of receive lines captured in parallel. In 3D imaging the number of image lines increases by a factor of the number of image lines in elevation. For focussed line-by-line ultrasound imaging the time required to focus to each limit is prohibitively high. This was a key challenge in commercializing a 3D capable ultrasound system. The system developed by Smith, Pavy and von Ramm at Duke University [61], [62] applied Explososcan imaging to 3D imaging and demonstrated the collection of 4992 image lines of a pyramidal volume at a rate of 8 volumes/s by collecting 8 receive lines in parallel. The Duke University system was commercialized by Volumetrics Medical Imaging, Inc.

Fully sampled 2D arrays (matrix arrays) have been developed and commercialized that use an ASIC (application specific integrated circuit) in the probe handle to reduce the number of signal channels in the cabling from the probe to the beamforming electronics [64]–[66]. In this type of approach, the beamforming is broken up into two stages. The first stage is accomplished by the ASIC, which beamforms the signals from groups of elements in the array or sub-arrays, reducing the number of channels in the cable to the number of sub-arrays. The second stage of beamforming is completed in the imaging system. This

technique is called micro-beamforming. While this technique allows real time 3D imaging to be completed, the solution does not address the complexity of connecting to thousands of array elements, which is prohibitive at high frequencies. These arrays exist only for low clinical frequencies (2-5 MHz) and the interconnect scheme only gets more difficult with increased frequencies. For our 30-40 MHz array the element size would be approximately an order of magnitude smaller.

There is a growing body of research reporting techniques to overcome the challenges associated with a fully sampled 2D ultrasound array by simplifying the array architecture. There are two main approaches reported to reduce array element count: 1) a sparse 2D array and 2) a crossed electrode array design. The array design is important for reducing cost and easing fabrication requirements; however, the performance of the array also greatly depends on the imaging scheme employed to build images. This is especially true for these unconventional array designs. This section provides a review of the literature reporting sparse 2D array designs and crossed electrode arrays as well as the beamforming approaches and the key performance measures.

2.3.2 Sparse 2D Arrays

A sparse array is designed with only a small subset of elements active. Thus, reducing the number of connections to a 2D array significantly. Generally,

sparse arrays have challenges with signal strength and secondary lobe levels because the active elements are a very small percentage of the array and are spread out over the aperture with large element to element pitch.

The literature surrounding sparse arrays attempts to determine the minimum number of elements that must remain active in a 2D array to produce high-quality images. In addition to element count, the pattern of elements chosen greatly changes the result. For a sparse array, it is desirable to spread elements over the aperture (increase effective aperture size, D) to minimize the main lobe width. However, one of the key considerations in increasing element spacing beyond $\lambda/2$ is the introduction of grating lobes. Grating lobes are an artifact that occurs when the element pitch is not fine enough ($> \lambda/2$ for phased arrays). These large off-axis regions of constructive interference occur at angles where the difference in the distance from the focus to each element is one wavelength (λ) [67]. Sparse 2D arrays with random element-to-element pitch in both directions were introduced as a solution to the introduction of grating lobes in sparse arrays [68]. Removing the periodicity of the array in a random arrangement suppresses grating lobes, however, secondary lobe energy is then increased. Smith et al. [61] showed that using a different transmit and receive aperture can reduce secondary lobe levels because the effective aperture is the convolution of the transmit aperture with the receive aperture. The transmit and receive aperture can also have different periodic spacing referred to as periodic or

Vernier arrays [44], [69]. Yen et al. [70] reported a study that compared the simulated point spread functions produced by several sparse 2D array patterns to determine feasibility for 3D imaging. The study included a periodic pattern, a random pattern and a Mills cross pattern and compared the results to a fully sampled 2D array. This detailed comparison makes it a good example for illustrating the trade-offs associated with the common sparse 2D array designs. The Mills cross is a concept borrowed from a radio antenna array design [71]. The 2D array is reduced to a crossed set of electrodes where the line of transmit elements are orthogonal to the line of receive elements. Mills cross arrays (Figure 2-22) have been built by several investigators [61], [72], [73]. Each of the sparse arrays in the comparison study by Yen et al. [70] was simulated using a comparable number of active elements. These arrays were very sparse in order to have a reasonable element count (one comparable to a 1D array). The active area

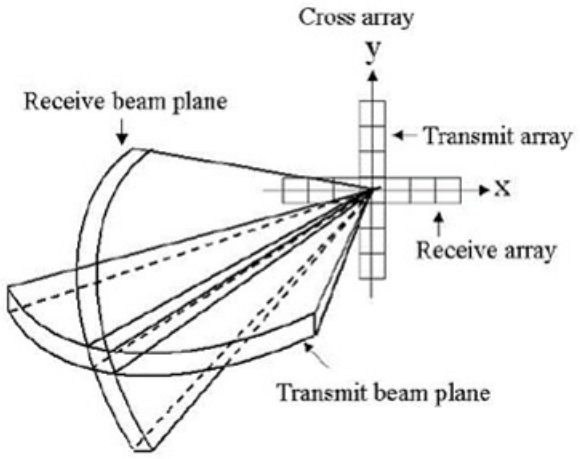

Figure 2-22 3D imaging with a Mills cross array Reprinted from [73], © 2004 IEEE.

is reduced to 1-3% of the total array area, which significantly compromises array sensitivity on transmit and receive. The ratio of average secondary lobe power to main lobe power is equal to $\frac{1}{N}$, where N is the number of active elements [67].

The beamwidth and sensitivity results from the simulations are summarized in Table 2-1 and Table 2-2 respectively. The big picture takeaways relate to the -40 dB beamwidths and the sensitivity results. Rather than quantifying a secondary lobe level, the authors provided this measure of beamwidth -40 dB down from the peak of the main lobe. What the results illustrate is that, while the main lobe width can largely be maintained, the Vernier array and random array's secondary lobe levels were greater than -40 dB since a measure for beamwidth could not be determined. Table 2-2 reports the pulse-echo sensitivity results which show the peak received signal normalized to the fully sampled case.

Table 2-1 Beamwidth results (in mm) for sparse array simulation. Reprinted from [70], © 2000 IEEE.

	Fully Sampled		Vernier		Random		Mills Cross	
dB level	Azimuth	Elevation	Azimuth	Elevation	Azimuth	Elevation	Azimuth	Elevation
On-axis beamwidths								
-6	0.52	0.52	0.54	0.54	0.42	0.49	1.1	0.58
-20	0.96	0.96	12	12	0.80	0.84	2.0	1.0
-40	1.73	1.73	Clutter floor	Clutter floor	Clutter floor	Clutter floor	5.8	3.5
Off-axis beamwidths								
-6	0.50	0.50	0.80	0.80	0.55	0.46	1.24	0.71
-20	1.1	1.1	19.5	19.5	0.88	1.06	2.4	1.48
-40	2.0	2.0	Clutter floor	Clutter floor	Clutter floor	Clutter floor	7.0	4.7

Table 2-2 Pulse-echo sensitivity results for sparse array simulation. The values are presented in dB compared to the fully sampled array case. Reprinted from [70], © 2000 IEEE.

	Array Type			
Focus	Fully Sampled	Vernier Array	Random	Mills Cross
(0, 0, 30) mm	0	-69.8	-61.9	-43.6
(16, 16, 30) mm	-3.3	-73.3	-65.0	-52.2

In all the example sparse cases the sensitivity is more than 40 dB (and as much as 70 dB) down from the benchmark. This highlights the crucial disadvantage of sparse array designs.

Sparse 2D arrays designs address the challenges associated with connecting to thousands of elements in a fully sampled 2D array as well as building electronics to support the thousands of channels. There is a harsh trade-off, however, between reducing the element count and maintaining image quality since, in general, secondary lobe and clutter levels are inversely proportional to element number. The loss in sensitivity will also contribute to poor imaging performance. In addition to these trade-offs, the elements in a sparse array are the same size as a fully sampled 2D array. This approach to 2D imaging does not address the challenge in electrical matching since the element impedance remains high very. High element impedance makes it more difficult to deliver power during transmit, introduces artifacts from cable reflections, and inherently has a higher noise floor since baseline noise levels are proportional to impedance.

2.3.3 Crossed Electrode Arrays

The second array architecture to discuss is the crossed electrode array. The crossed electrode array has an unconventional electrode pattern. The bottom of the array substrate has a set of linear electrodes, similar to the pattern for a 1D array. A second linear set of electrodes are patterned on the top of the array orthogonal to the bottom electrodes (Figure 2-23). Connections to the array are made to these electrodes only. Considerable parallels can be drawn between this architecture and the Mills cross sparse array design. An entire row or column can be addressed at a time depending on which set of electrodes are used.

This array addresses the challenges associated with high element count as well as small element size. For an array comparable to a fully sampled square 2D array the element count is reduced from N^2 to $2N$. The elements are elongated to the full length of the array and have a reduced electrical impedance. The crossed electrode array is effectively equivalent to two orthogonal overlapping 1D arrays. Research groups have attached different names to their array designs including a

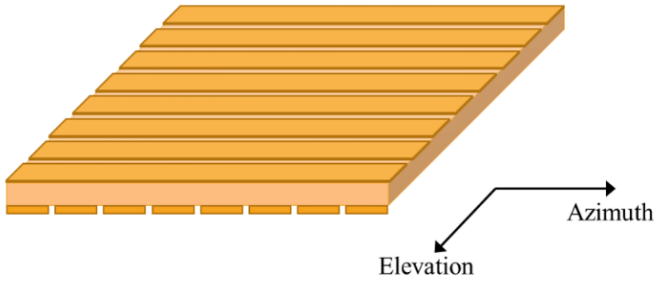

Figure 2-23 Design of a crossed electrode array.

row-column addressed array [74]–[83] a TOBE (top-orthogonal-to-bottom electrode) array [84]–[87], a biplane phased array [88] and a crossed electrode array [89]–[91]. Although there are significant differences across many of these previous designs (i.e. in active material, element addressing scheme, imaging scheme, etc.) they all share a commonality in that the array is built with two sets of orthogonal electrode patterns. In this document, the array architecture will be referred to as a crossed electrode array.

Several research groups [90], [92]–[94] have observed that the elongated elements and abrupt termination of the aperture in a crossed electrode array create edge waves that generate image artifacts. In a row-column addressed crossed electrode array there is no electronic control over the length of the element, and consequently, electronic apodization cannot be applied. Joyce and Lockwood [90] address this problem by poling the piezoelectric substrate using a radially variable electric field. The gradient in sensitivity of the array creates a permanent apodization. Christensen et al. [94] describe a solution to this problem using CMUT arrays. This design achieves integrated apodization by varying the effective CMUT membrane area. The number of cells in the transducer follows a circularly symmetric Hann function. The cells are densely packed near the centre and become sparse nearing the edges.

Row-Column Addressing

Creating a two-way focused 3D image in real-time is difficult with crossed electrode arrays because azimuth and elevation dimensions cannot be beamformed at the same time. Delayed pulses cannot be applied along the elevation dimension without disrupting the delayed pulses applied in the azimuthal dimension. Several groups have presented similar imaging techniques for the crossed electrode array where the top electrodes focus on transmit and the bottom, orthogonal electrodes focus on receive [76]–[80], [89]–[91]. Because there is a switch from activating the top electrodes (rows) to the bottom electrodes (columns) it is referred to as row-column addressing. This technique creates only a one-way focus in each plane, like the approach for a sparse Mills cross array.

As was shown in Figure 2-20, the secondary lobe levels are significantly increased in the radiation pattern of a one-way focus. Figure 2-24 shows an example 2D radiation pattern using a row-column addressing scheme. The secondary lobes along the azimuthal and elevational planes only decrease to -40 dB. In addition, the main lobe beamwidth is wider for the one-way case. To achieve resolution and secondary lobe levels comparable to a fully sampled 2D array using this crossed electrode array technique, it is necessary to double the aperture and number of elements. Unfortunately, this adjustment is not conducive to an endoscopic device. The key advantage of this technique is the ability to generate very high frame rate volumetric images. The transmit beam is

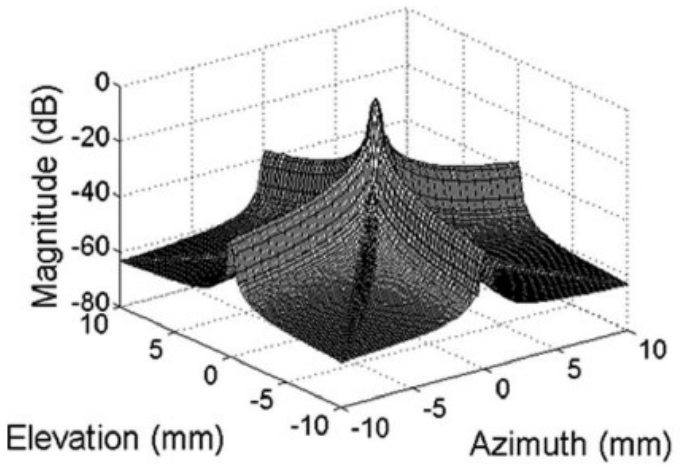

Figure 2-24 Typical radiation pattern of a crossed electrode array using row-column addressing. Reprinted from [78], © 2009 IEEE

focussed to select the 2D elevation slice in the volume. The RF data collected by the receive elements, in the orthogonal direction, can be beamformed dynamically throughout the 2D plane. In this way, a one-way focussed 2D image can be collected for each insonification, and the volumetric frame rate depends only on how many elevation slices are required. Demore et al. have shown that large fields of view (60° x 60° pyramidal scan) can be obtained at high frame rates (>20 volumes/s) by curving the array and defocusing the radiation pattern [89], [91].

Synthetic Aperture Imaging

Synthetic aperture imaging refers to any technique that uses the principle of linear superposition to synthetically build up an effective aperture, however, approaches and performance can vary. For example, in the 3D case, a synthetic aperture can be built in the elevation direction only or on receive only.

Investigators have presented work comparing synthetic aperture techniques for 3D imaging [80], [95]. In general, the trade-off is increased resolution for decreased SNR and frame rate. This is because generating a tight focus requires collecting the transmit/receive response from small elements across a large aperture. Consequently, only a small area of the array is active on each transmit event.

The application of bias-sensitive array substrates to the crossed electrode array design has introduced new possibilities in imaging approaches. Bias-sensitive materials, for example, electrostrictive ceramic or CMUTs, only produce a pressure response when a DC bias is applied. Furthermore, the polarity of the pulse changes with the sign of the DC bias and elements can be turned off by connecting the element to ground. In a previously described approach, the bias control of CMUTs has been used to address the 2D elements individually in a chosen plane (i.e. the bias is applied on a column and signal transmission and reception occurs on the rows). When imaging with this technique, pulse patterns are not limited to a whole row/column, but the pulsing sequences are usually based on some form of synthetic aperture focusing in at least one of the dimensions [80], [84], [85]. Again, these approaches generally attempt to balance the beamwidths achievable in both planes, low SNR resulting from synthetic aperture, and the number of transmit events per frame, making high-quality real-time imaging challenging.

A similar approach, titled Fast Orthogonal Row-Column Electronic Scanning (FORCES), has more recently been introduced to increase frame rate and SNR through bias encoding a Hadamard sequence during transmit in one plane, and, subsequently, decoding to acquire channel data for synthetic focusing on transmit [53], [54], [96]. Therefore, a one-way synthetic aperture is created with 100% of the array active during each transmit event. In the FORCES technique, the Hadamard encoding process improves the signal to noise ratio over single element synthetic aperture beamforming, however, the elevation plane is limited to a one-way focus.

2.4 Bias-Controlled Imaging

This project started with the idea that if an acoustic lens could be replaced with an electrically reconfigurable lens we could steer the ultrasound energy in elevation as well as azimuth and build a 3D image. A more general way to describe the goal is ultrasound imaging in a 2D plane by only changing a set of biases across a substrate (i.e. considering the elevation plane only). When visualizing the concept of bias-sensitive imaging it is useful to think about a single piezoelectric substrate with a single RF channel connection, it is analogous to rotating the coordinate system and looking at the array in the elevation-depth plane. Figure 2-25 illustrates the limitation of trying to image with this solid substrate and a single RF channel. We can apply a pulse to the element and

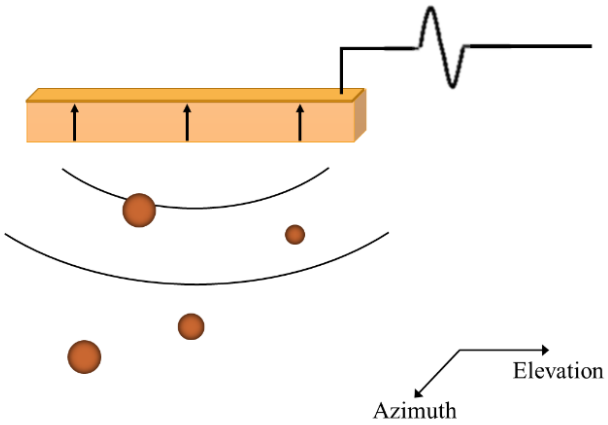

Figure 2-25 Imaging with a single solid substrate, with a single RF channel.

create an un-focused pressure wave, however, we cannot focus or steer to build an image. All the scatterers in the range of the pulse would appear to be in the same lateral location. This situation is an example of the simplest ultrasound system where a single A-scan line can be collected by transmitting a pulse and receiving the echoes. However, to collect a whole image worth of data the transducer would have to be physically scanned. This is the performance limitation if we only consider conventional piezoelectric materials.

The use of materials that allow the polarization direction in the substrate to be dynamically controlled allows for a reimagination of the possibilities of what this simple theoretical device can accomplish. A piezoelectric substrate with a positive polarization vector will expand in response to a positive voltage and contract in response to the negative voltage portion of the excitation pulse. This creates a positive pressure pulse. A piezoelectric substrate with a negative polarization vector will respond oppositely (i.e. contract in response to positive

high voltage and expand in response to negative high voltage). This creates a pressure pulse of opposite polarity, the negative pulse. Electrostrictive ceramic is an ideal material to accomplish pulse polarity control. By changing the pattern of positive and negative pulses across the material, the shape of the wave front generated when it is pulsed can be altered and exploited for imaging.

2.4.1 Reconfigurable Elevation Lens

One way to accomplish bias-controlled imaging is to create an electrically reconfigurable elevation lens. Figure 2-26 shows a 1D phased array with a fixed acoustic lens. The array is beamformed to focus on-axis in the azimuth direction and the acoustic lens provides the elevation slice selection on-axis. If that lens could be electrically steered through a set of elevation angles a 3D image could be collected very quickly. A lens can be created by controlling the pattern of positive

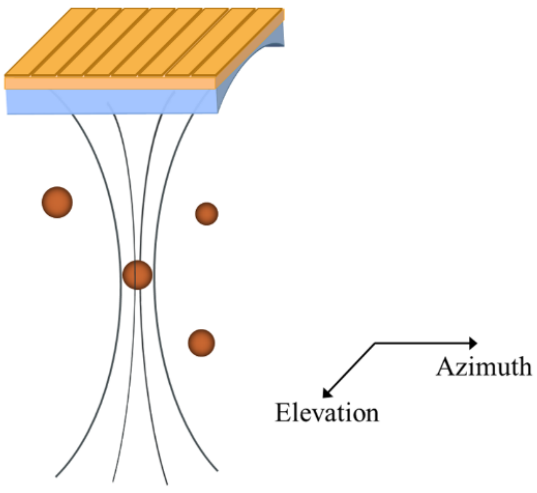

Figure 2-26 1D phased array with a fixed acoustic lens.

and negative polarization across the substrate to mimic a Fresnel lens (Figure 2-27 a)).

This creates an area of constructive interference at a focal point (Figure 2-27 b)). The pattern can be adjusted to steer the focus to an off-axis angle (Figure 2-27 c), d)). Therefore, using only a reconfigurable pattern of biases across an array we can focus and steer and, theoretically, build a 2D ultrasound image.

The Fresnel lens was invented by French physicist Augustin-Jean Fresnel. The design of the lens exploits the idea that the direction of light propagating within a medium does not change unless it encounters something to cause

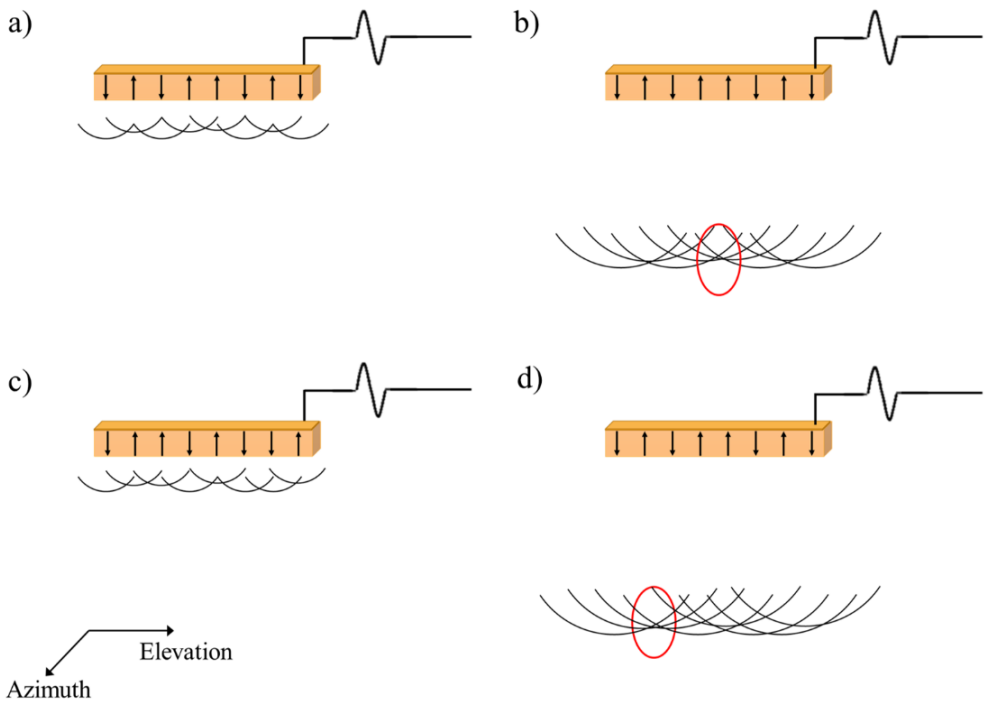

Figure 2-27 Wave propagation and interference from a bias pattern creating a Fresnel type focus a), b) on axis, c), d) off axis.

scattering. Instead, the propagating light changes directions at the boundaries of mediums. As a result, the bulk material in a conventional lens increases the size and weight of the lens without contributing to the focus. The Fresnel lens consists of a series of concentric rings, each maintaining the curved surface of a conventional optical lens. However, the lens is mostly flat because the material where more than a wavelength propagates is removed (Figure 2-28). A notable application for the Fresnel lens is collimating light in lighthouses, where size and weight are limited but the light originating from a close focus must be emitted and seen from distances far from the lighthouse. It is important to note that when high precision imaging is required, conventional optical lenses outperform the Fresnel lens because the discontinuities of the lens reduce resolution and cause some scattering.

A Fresnel zone plate is a similar design to the Fresnel lens but uses diffraction of light, rather than refraction, to create a focus. The Fresnel zone plate consists of alternating opaque and transparent regions (e.g. concentric rings or linear strips) shown in Figure 2-29. The zone switches from opaque to

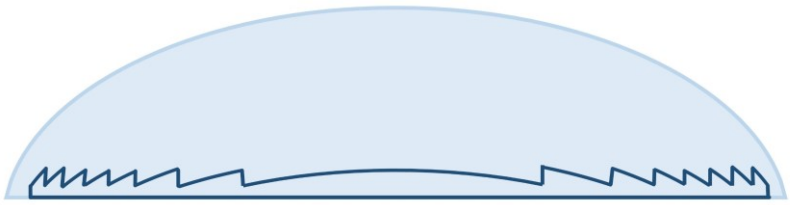

Figure 2-28 Diagram comparing the thickness of a conventional optical lens with a Fresnel lens.

transparent when the length from the point on the zone plate to the focal point, l_n, is $\lambda/2$ greater than the distance between the centre of the previous zone to the focal point, l_{n-1}. (Figure 2-29 b)) The transitions between the opaque and transparent zones, given as a distance from the centre, r_n, is as follows

$$r_n = \sqrt{n\lambda(z + \frac{n\lambda}{4})} \tag{2-32}$$

where n is the transition number, λ is the wavelength in the medium and z is the focal distance. Choosing the number of zones in the plate influences the resolution capabilities. The resolution or beamwidth, $FWHM_{fres}$, is given as follows

$$FWHM_{fres} = \lambda \frac{z}{r_N} = \lambda F \tag{2-33}$$

In short, increasing the zone plate size (or reducing the system f-number) improves lateral resolution. A phase-reversal zone plate (or Wood zone plate)

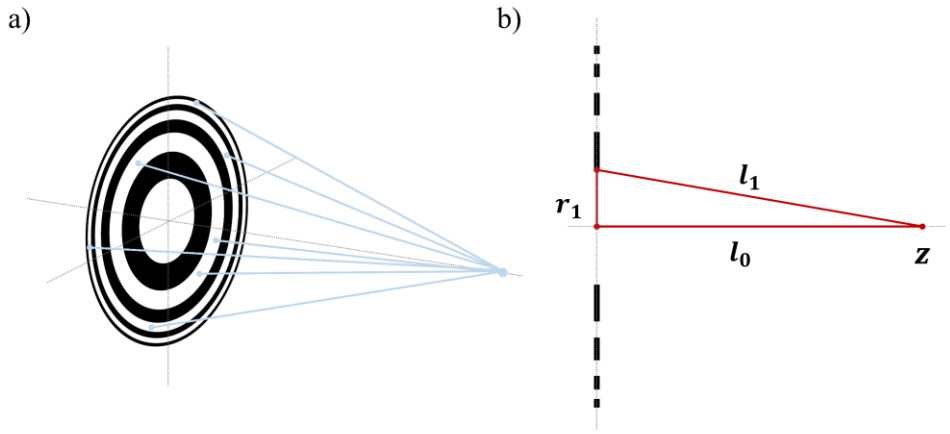

Figure 2-29 A Fresnel zone plate showing a) the focus as a result of the diffraction around the opaque zones and b) the path length difference between rings.

increases efficiency by replacing the opaque zones with transparent zones that cause a phase reversal in the wave [97], [98].

Acoustic waves, like light, can also be focused using a Fresnel lens or zone plate approach. Phase-reversal zone plates have the advantage of greater efficiency [98] and are an effective approach for passive ultrasound focusing [99], [100]. Implementing a Fresnel approach in an ultrasound transducer requires control of the pulse polarity. Arrays built on either electrostrictive ceramics or CMUTs are appropriate for this approach because the phase is controlled by the polarity of a DC bias. Electrostrictive ceramics such as PMN-PT (lead magnesium niobate-lead titanate) ceramic can be used as the array substrate in place of conventional piezoelectrics. This type of material is only piezoelectrically active while a bias voltage is applied, and the sensitivity is tunable with the amplitude of the bias voltage. When no voltage is applied to the transducer, the response is negligible, and when a DC bias is applied, the phase of the acoustic wave produced is quantized to either +90 or -90 degrees, depending on whether the bias is positive or negative. Elements defined on an electrostrictive substrate can be addressed individually and in parallel by turning the element on with applied bias. Reconfigurable Fresnel zone plates can be created by varying biasing patterns with positive and negative voltages across the substrate.

When creating a Fresnel type focus, the bias value for each element is calculated by considering the geometric path length between the element and the focus. The relative phase delay for that element is given by

$$\varphi_n = \frac{2\pi(z - \sqrt{x^2 + y^2 + z^2}}{\lambda} \tag{2-34}$$

Where x, y and z are the coordinates of the desired focus relative to the array element and λ is the wavelength of the center frequency of the excitation pulse in the medium. The sign of the bias (S_{bias}) is given as follows

$$S_{bias} = sign[mod(\varphi + \varphi_{offset}, -2\pi) - \pi] \tag{2-35}$$

This is a phase wrapped approximation of the relative phase delay for each element. The portion of the delay that falls within a single wavelength is then quantized as $+\pi/2$ or $-\pi/2$ radians. The quantized phase delay models the purely transparent regions and the phase inverted regions of the Fresnel zone plate (or Fresnel lens). An offset phase can be added in the calculation that shifts the reference phase of the center element [101], [102]. Therefore, there is not one unique Fresnel pattern for a given focal point. The pattern can be chosen to optimize for different beam shapes (e.g. main lobe width, secondary lobe level, sensitivity). An example Fresnel bias pattern is shown in Figure 2-30 a). This acoustic zone plate focus was simulated using Field II [55]. A 10 MHz, 64 element, 1D array positioned along the elevation direction was simulated and the

pattern of positive and negative pulse polarity was modelled by setting the apodization across the array to either +1 or -1. Figure 2-30 b) shows the two-way radiation pattern across the elevation direction at the focal depth. The result is a narrow main beam, indicative of the constructive interference at the focus. However, the secondary lobe levels (-25-30 dB) show that there is not ideal destructive interference off-axis. For high quality imaging we require the secondary lobe levels to be below -50 dB.

Creating an approximation of a Fresnel lens is one way to perform bias controlled imaging. The acoustic Fresnel lens can both focus and steer ultrasound energy over a 2D plane, collecting image lines and generate a conventional B-mode ultrasound image. This is all accomplished with a single RF channel and polarity control across the substrate. Because of this, the lens concept was chosen as the basis for this project. However, the quality of focus is not high enough for

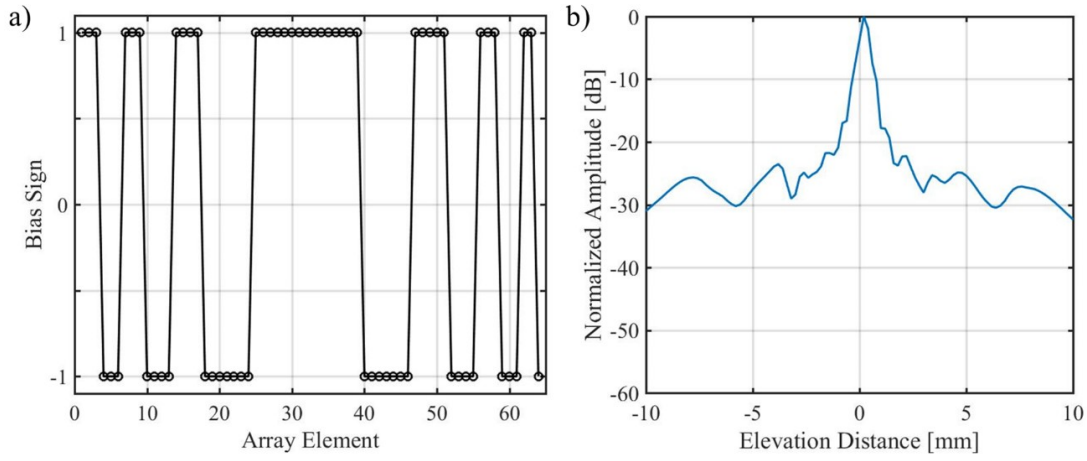

Figure 2-30 An example Fresnel focus showing a) the biasing pattern for a focus directly in front of the array (F=2.4) and b) the resulting simulated two-way radiation pattern profile.

this imaging technique to be directly applied to 2D or 3D imaging in this simple form. This dissertation discusses techniques that use an electrically reconfigurable acoustic Fresnel lens as a seed of an idea that evolves into newly developed techniques that can produce high-quality ultrasound images.

2.5 Clinical Three-Dimensional Ultrasound Imaging

A significant amount of work has been put into the clinical evaluation of 3D ultrasound across many fields of medicine. This section is a summarized review of the applications that have demonstrated the most success in adopting 3D ultrasound imaging. It is included to give context and support for the goal of creating a high frequency endoscopic ultrasound system. These few examples are meant to give a broad picture of where 3D ultrasound is being used and the reasons it is providing clinical value.

An advantage of 3D ultrasound imaging that repeats in the clinical literature is accuracy in volume measurement. In echocardiography, ultrasound images are captured very quickly and then compared to track blood volumes and heart movement through the cardiac cycle. 2D imaging has inherent limitations since its measurements rely on geometric assumptions and often underestimate heart chamber sizes because of foreshortened views [103], [104]. Because of the improved accuracy provided by 3D echocardiography, the published recommendations regarding cardiac chamber measurements have been updated to

include reference values and guidelines supporting 3D imaging [105]. Other applications that highlight 3D ultrasound's ability to accurately measure include atherosclerotic plaques and carotid artery stenosis in vascular imaging [106], [107] and thyroid volumes [108], [109].

Many papers have described the instinctive tendency of sonographers and physicians to mentally reconstruct the anatomical 3D volume from a series of 2D slices. 3D imaging eliminates the need for this skill. The volume image can be displayed in both a volume rendered image as well as a series of 2D slices in whatever plane is desired. 3D rendered ultrasound images are advantageous in the early diagnosis of several key areas of fetal abnormalities including facial [110]–[112], neural tube defects and skeletal malformations [113]–[117]. Prenatal ultrasound scanning gives ideal conditions for surface assessment since the fetus is surrounded by amniotic fluid [118]. In addition to the many views and cross-sections available, any structures obscuring the region of interest can be electronically removed while interpreting the images with an electronic scalpel.

Another common term in the literature is the "surgical" view or "en face" view which highlights a key advantage of volume imaging. Now, anatomy that is hard to access can be viewed from whatever angle is convenient for the physician. There are many example applications where visualizing the tissue from the direction they would if completing surgery is a compelling advantage. Coronal plane views in breast imaging have been shown to aid in surgical planning and

accuracy in typing benign and malignant tumours [119]. Also, face-on views of the mitral valve during dysfunctional operation aid in planning the repair [120].

Minimally invasive techniques are increasingly becoming standard of care across clinical disciplines because of the benefits to the patients, health care providers and the health care system alike. While two-dimensional imaging has been used to guide these types of procedures in the past, 3D imaging has the potential to provide more accurate guidance [121]. One example of a 3D ultrasound-guided interventional procedure is prostate brachytherapy. Using transrectal ultrasound guidance, radioactive seeds are carefully placed into the prostate to deliver a high radiation dose while sparing surrounding tissues [122]. An in vitro study of the variability and accuracy of seed placement under 3D guidance showed standard errors of less than 0.5 mm [123].

Needle biopsies are another example of interventional procedures that require accurate positioning within a volume. Breast biopsies are used to determine a diagnosis after suspicious results from regular imaging screening. 2D ultrasound can provide high quality, real-time images without a radiation dose, however, it is difficult to keep the needle in the image and confirm it is placed in the lesion. A phantom study showed that a biopsy needle under 3D guidance can be positioned within 1.16 mm of the target independent of needle direction [124]. In a study comparing 2D data to 3D ultrasound data in biopsy procedures in all cases but 1 (99.5%) the 3D data influenced the biopsy procedure either by revealing an out of

lesion hit or a marginal lesion hit which would prevent the need for a repeat procedure [125].

Since surgical views and interventional procedures have been highlighted as key advantages to 3D imaging, miniaturizing 2D array transducers for procedure guidance at the surgical site is a clear path for development. Transducer arrays packaged in laparoscopic, endoscopic or intra-catheter form factors can be fed into the body. The advantage of this approach is the reduction in penetration depth to get to the desired area which allows for an increase in frequency and higher resolution images.

CHAPTER 3

SIMULTANEOUS AZIMUTH AND FRESNEL ELEVATION (SAFE) COMPOUNDING: A FAST 3-D IMAGING TECHNIQUE FOR CROSSED-ELECTRODE ARRAYS

3.1 Preamble

This chapter largely includes content published in IEEE Transactions on Ultrasonics, Ferroelectrics, and Frequency Control [5]. Any introductory material previously covered in the Background Chapter has been removed or reduced for conciseness. Modifications have been made to unify this document both in terms of nomenclature and formatting as well as providing a clearer story of the relevance in the evolution of the project. Some relevant context for the imaging approach that did not appear in the original paper has been added. Permission has been granted by IEEE to include the figures and data published in the paper in this thesis. The main goal of this study was to develop a new bias-controlled elevation lens concept and show results on a proof of concept crossed electrode array.

3.2 Introduction

Ultrasound systems based on 2D matrix arrays capable of 3D imaging present several technical challenges including the number of elements/beamforming channels, electrical matching issues resulting from the high impedance of the small elements, and image acquisition time for a 3D volume. Crossed electrode arrays have addressed some of these issues, especially the huge reduction in the number of elements. However, creating a two-way focused 3D image in real-time is difficult with these arrays because azimuth and elevation dimensions cannot be beamformed at the same time. This typically forces one to use a synthetic aperture approach which is inherently slow, requires increased beamforming complexity over a 1D array, and may suffer from low signal to noise [76], [78], [126].

Previously, non-synthetic aperture crossed electrode arrays have also been described using an imaging scheme where the top electrodes focus on transmit and the bottom, orthogonal electrodes focus on receive [89]–[91]. This technique creates only a one-way focus in each plane. For resolution and secondary lobe levels comparable to a fully sampled 2D array, it is necessary to double the aperture and number of elements on the crossed electrode array. Another previously described approach has been to use the bias control of CMUTs to address the 2D elements individually in a chosen plane (i.e. the bias is applied on

a column and signal transmission and reception occurs on the rows). When imaging with this technique, pulse patterns are not limited to a whole row/column, but the pulsing sequences are usually based on some form of a synthetic aperture focusing in at least one of the dimensions [80], [84], [85]. These approaches generally attempt to balance the beamwidths achievable in both planes, low signal to noise resulting from synthetic aperture, and the number of transmit events per frame, making high-quality real-time imaging challenging. A similar approach, called Fast Orthogonal Row-Column Electronics Scanning (FORCES), has more recently been introduced to increase frame rate and signal to noise through bias encoding a Hadamard sequence during transmit in one plane and subsequently decoding to acquire channel data that can be used for synthetic focusing on transmit [53], [54], [96]. The Hadamard encoding process improves the signal to noise ratio over single element synthetic aperture beamforming, however the elevation plane is limited to a one-way focus.

A different approach is presented in this study, where a focus in the elevational dimension is generated using a reconfigurable acoustic Fresnel lens, while simultaneously beamforming in the orthogonal azimuth plane that has access to the RF channel data. Acoustic waves, like light, can be focused using a Fresnel lens or zone plate approach. Implementing a Fresnel lens in an ultrasound transducer requires control of the pulse polarity. Arrays built on either electrostrictive ceramics or CMUTs are appropriate for this approach because the

phase is controlled by the polarity of a DC bias. Passive acoustic lenses are generally used to focus the acoustic beam for 1-D linear array transducers in the elevation dimension. These lenses define the slice resolution and depth of field for the resulting 2D images. It is possible, however, to replace such a passive acoustic lens with a Fresnel zone plate pattern [102] applied to electrodes aligned in the elevation dimension. This is done by simply varying the direction of polarization across the piezoelectric elements. Since this type of active lens can be reconfigured to steer to moderate steering angles, a volumetric image can be captured without adding additional beamforming channels over a conventional 1-D array. Figure 3-1 shows the configuration of our crossed electrode array. The arrows along the elevation direction indicate the polarization vector for each elevational element and correspond to the sign of the applied DC bias. A similar

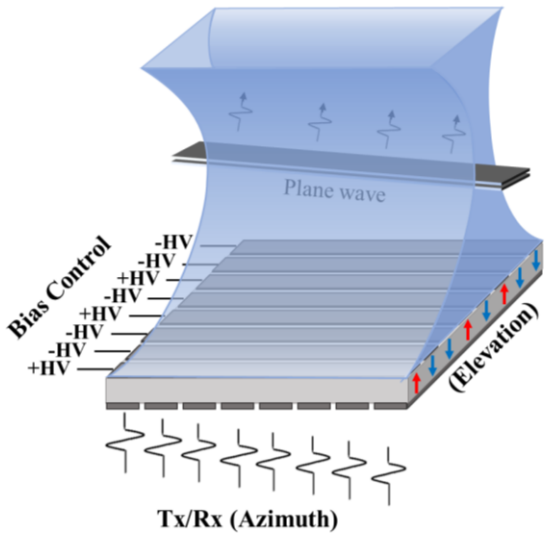

Figure 3-1 Crossed electrode array with elevation bias control. The arrows along the elevation direction indicate polarization direction with positive coloured coded in red and negative in blue.

crossed electrode electrostrictive transducer configuration has been previously described for a transducer intended for therapeutic applications [101], [127].

Because the back electrodes provide the active lens control in the elevation plane, the array requires only $2N$ (in our case 128) electrical connections but only N (64) beamforming channels. An alternative approach to capturing 3D image volumes with a conventional 2D array requires N^2 elements and beamforming channels (4096 in our case). The low beamforming complexity and minimal electrical connectivity used in this approach provide an enormous practical advantage over conventional 2D matrix array designs. This is especially important in endoscopic applications that have minimal packaging real estate. The electrical interconnect often becomes a significant fraction of the packaging, therefore, minimizing the number of elements required is essential.

An alternative version of this electrically reconfigurable Fresnel lens for high frequency imaging has been presented by our group previously [2] wherein the Fresnel lens was used in the elevation dimension on transmit and was combined with simultaneous transmit beamforming in the azimuth dimension. The biased channels would subsequently switch sides with the RF channels on the array between transmit and receive in order to achieve adequate beam profiles in 3D. In addition, a split and delay sub-aperture technique was used to preserve axial resolution while steering to wide angles with the Fresnel lens approximation. Drawbacks to this approach were 1) the complexity in switching the

beamforming channels between the front and back-side set of electrodes between transmit and receive beamforming and 2) achieving real-time 3D frame rates when using the sufficient number of A-scan lines, aperture splits, and transmit focal zones for high-quality volumetric imaging.

This study describes a new, fast, and simple 3D imaging approach that has been termed "SAFE" compounding, which stands for simultaneous azimuth and Fresnel elevation compounding [6]. The principle behind this technique is to perform plane-wave compounding with the front set of electrodes while implementing a reconfigurable Fresnel elevation lens with an orthogonal set of back-side electrodes. While this Fresnel lens design would usually result in unacceptable secondary lobe levels, these lobes can be suppressed by compounding multiple Fresnel patterns. Since plane-wave imaging already compounds the same slice repeatedly, multiple elevation Fresnel lenses can be simultaneously compounded to increase the elevation beam quality, resulting in no loss in frame rate. In addition, since a single elevational slice (a 2D plane wave image) can be generated at very high frame rates, many elevation slices can be collected while still maintaining real-time volumetric frame rates. In this study, the design, fabrication, and characterization of a crossed electrode array based on an electrostrictive ceramic is presented, and the SAFE compounding approach to volumetric imaging has been simulated and experimentally demonstrated.

3.3 Imaging Methodology

If this type of active Fresnel elevation lens is changed upon sequential pulsing to focus to 'n' spatially different focal spots that are nearby, but separate enough that the Fresnel pattern changes, the acoustic beam can be averaged (compounded) to reduce secondary lobe energy while preserving main lobe energy. Figure 3-2 illustrates the performance improvement with a set of simulated radiation patterns in elevation created by using a single Fresnel lens pattern then compounding sets of 8, 16, 32, and 64 Fresnel lens bias patterns. If a set of elevation elements is reconfigured with enough Fresnel patterns, it has the potential to replace a passive elevation lens with little loss in slice resolution or image quality. A compounded Fresnel lens such as this is also capable of steering, thus enabling the collection of multiple elevation slices with no added complexity

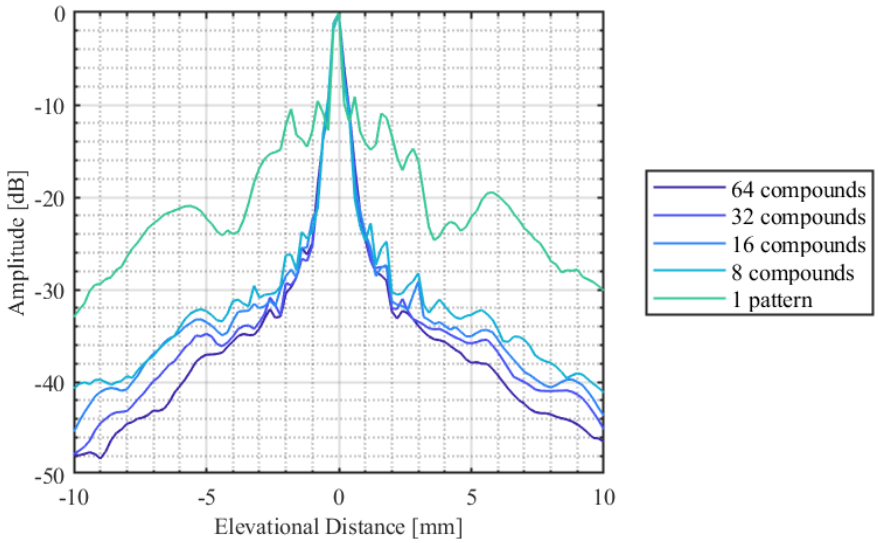

Figure 3-2 A set of simulated radiation patterns created by using a single Fresnel lens bias pattern compared to the results of compounding 8, 16, 32 and 64 patterns.

beyond changing a pattern of DC biases in the elevation direction that determine the polarization direction across the piezoelectric.

The effectiveness of the SAFE compounding technique comes from the fact that while a Fresnel lens is compounded and focusing on an elevational slice, conventional plane-wave compounding is concurrently used in the azimuth direction. The Fresnel lens pattern is changed for each angled plane wave, while still focusing to a spatial location that is very close (i.e. focusing to the same slice). Therefore, the synthetic transmit aperture can be built in the azimuth direction while, in parallel, suppressing the elevational secondary lobe energy. Coherently compounding the azimuth frame increases image quality in both planes simultaneously. A 3D image is then built up from the multiple 2D slices collected similarly. The same set of plane waves used to generate a compounded image is repeated for a different sub-set of Fresnel patterns, where each sub-set corresponds to a different elevational slice. This technique can form volumetric images very quickly ($>$ 7 volumes/s) due to the high speed at which high-quality plane-wave images can be generated in the azimuth dimension [47].

Figure 3-3 shows an example of simultaneous compounding patterns in the elevation and azimuth planes, for three sequential transmit events. This set of Fresnel patterns focusses to a 0° steering angle. For each transmit event, the f-number for the Fresnel lens is slightly adjusted such that the elevation focus is in very close proximity but moved just enough to change the Fresnel pattern. In

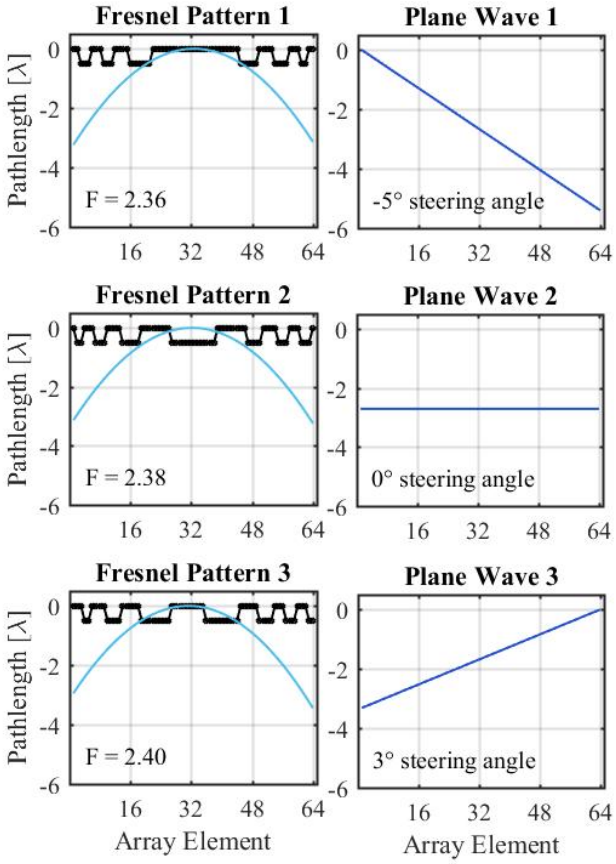

Figure 3-3 Example simultaneous compounding patterns in the elevation (Fresnel pattern) and azimuth (plane wave profile) planes, for 3 sequential transmit events.

the azimuth dimension, the plane wave angle is adjusted on sequential pulses so that a synthetic focus can be generated following the set of insonifications. On receive, the Fresnel lens still establishes a receive focus in elevation, and dynamic receive beamforming is performed in the azimuth plane from the channel data collected.

The phase is important when compounding the Fresnel lens patterns. To successfully compound the image frames the pulse produced by each Fresnel pattern must aligned in phase. However, because the Fresnel patterns

approximate a lens by setting positive and negative phases across the aperture, any change to the pattern produces a group change in the phase of the received echoes within the slice. Therefore, a frame to frame group phase compensation must be completed before compounding the frames. The value of the phase shift can be estimated by simulation using Field II [55], or could also be approximated using the angular spectrum method [11]. The receive beamforming delays describing the time required to travel from point (x, z) to element x_1 are given by,

$$\tau_{rx}(x_1, x, z) = \frac{\sqrt{z^2 + (x - x_1)^2}}{c} \tag{3-1}$$

where c is the speed of sound in the medium. The transmit beamforming travel delays to the point (x, z) for a given angle, α, and corresponding Fresnel pattern phase compensation group delay, τ_{fres}, is given by,

$$\tau_{tx}(i, x, z) = \frac{zcos(\alpha_i) + xsin(\alpha_i)}{c} + \tau_{fres,i} \tag{3-2}$$

Each point (x, z) in the image is determined by delaying the RF signals using both the transmit and receive delay contribution over the signal elements across the array. Afterward, the full frames are coherently compounded. Figure 3-4 shows pulses produced by four example Fresnel patterns before and after the phase compensation has been inserted to optimize the phase alignment. It is obvious from Figure 3-4 that phase compensation is required or else significant

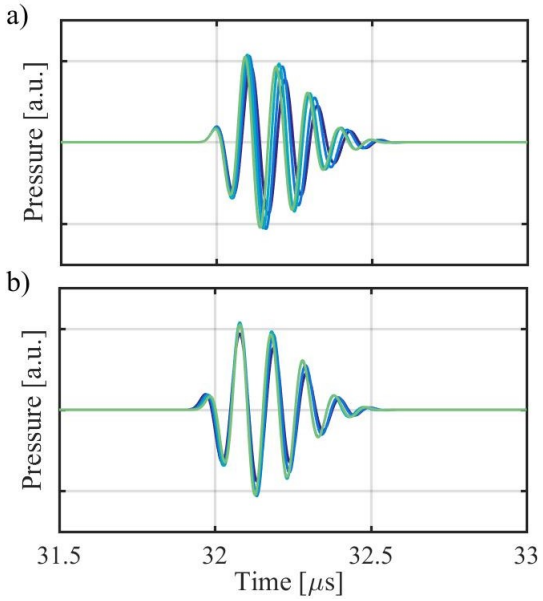

Figure 3-4 Pulses corresponding to four Fresnel patterns a) before phase compensation and b) after phase compensation.

destructive interference will result when compounding the on-axis pulses within the elevation slice.

Figure 3-5 shows an example of the destructive interference that occurs off-axis (outside of the focussing angle) for a 64 element Fresnel lens. Figure 3-5 (a) shows the individual off-axis (secondary lobe) pulses at an angle of 20° off the focal axis at 0° for 64 different Fresnel patterns and Figure 3-5 (b) shows the compounded off-axis pulse. Generally, a trend of $\sqrt{N_C}$ suppression of secondary lobes results, where N_C is the number of different Fresnel patterns destructively interfering.

One of the main design challenges with 3D ultrasound imaging schemes is the optimization of the number of transmit events required to generate a

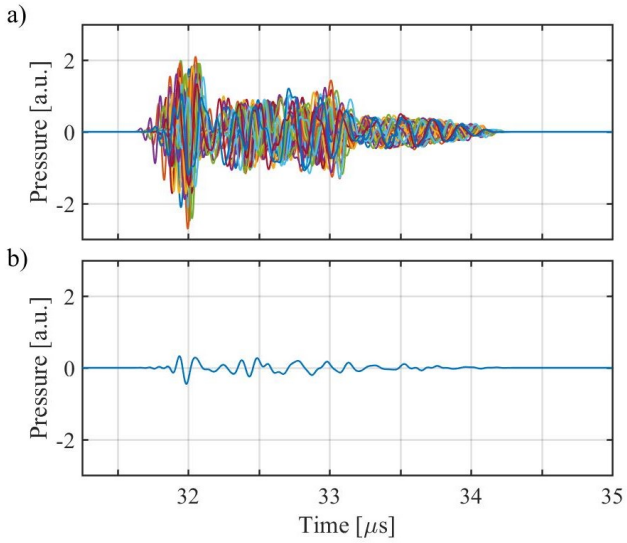

Figure 3-5. Simulated pulses 20° from the focal angle a) for each of 64 Fresnel patterns and b) the average of the 64 Fresnel patterns.

volumetric image. The frame rate for SAFE compounding imaging depends on the number of compounds necessary for desired elevation beam quality and the number of elevational slices chosen for the volume. The formula for volumetric frame rate (FR) is given by

$$FR = \frac{PRF}{N_C * N_S} \tag{3-3}$$

Where PRF is the pulse repetition frequency for the imaging depth, N_C is the number of compounds per slice and N_S is the number of elevation slices in the 3D image. For example, if the acceptable PRF for a 10 MHz centre frequency is 15 kHz (based on a 5 cm time of flight) and 32 compounds and 32 elevation slices are used, a frame rate of 14.6 volumes/s is achieved. It has previously been shown that to obtain image quality equivalent to conventional transmit-receive beamforming, $>$ 45 plane wave angles are required [47]. Therefore, it is desired to

gain sufficient elevation quality with a similar number of compounds to avoid decreasing the volumetric frame rate. In this study the number of simultaneous compounds have been limited to 64 and the number of elevation slices to 32. Therefore, for a 15 kHz pulse repetition frequency, the volumetric frame rate is limited to 7.4 volumes/s, which is still considered to be near real-time volume imaging.

3.4 Imaging Simulations

It is important to note that this study is intended to prove the feasibility of a newly developed imaging technique, but the technique has not yet been optimized for general applications and array geometries. The aperture size and number of elements in the array have a significant influence on the resulting resolution and secondary lobe level in the elevational radiation pattern. In this study, the number of signal channels and bias channels have both been limited to 64. This is because the planned progression of this project was to package a high frequency crossed electrode array into an endoscopic form factor similar to the 40 MHz 64-element array previously described [128]. The endoscopic array fabrication is described in Chapter 4. Increasing the number of channels significantly past 64 azimuth by 64 elevation, spaced at λ pitch, results in a prohibitively large endoscope using our current packaging/interconnect technique. If an alternate design with a smaller element pitch (e.g. $\lambda/2$) was proposed for

our goal of a 30 MHz endoscopic phased array, the element fanout inherent to doubling the number of wire-bonding pads would result in prohibitively large packaging. It should also be pointed out that we have limited the center frequency in this proof of concept prototype to 10 MHz instead of our intended frequency of 30 MHz. This was due to our limitation on the sampling rate for the experimental imaging system (Verasonics Vantage 256, Kirkland, WA) used to capture and compound the data at the time. In summary, due to future packaging considerations, and signal capture hardware limitations, our prototype design had a fixed number of elements (64 azimuth, 64 elevation), a fixed element pitch (λ), and a maximum operating frequency of 10 MHz.

A 10 MHz, 64 x 64 element crossed electrode array with λ element pitch, was simulated using Field II in both the elevation and azimuth directions simultaneously. The pattern of positive and negative biases across the elevation direction was modelled by simply applying +1 and -1 apodization values. Two-way radiation patterns were simulated by placing a scatterer at each of the field points and measuring the strength of the echo after beamforming. The elevation focus was set to 23 mm. The two-way radiation patterns across the elevation direction and azimuth direction for 1, 8, 16, 32, and 64 compounds are shown in Figure 3-6 and Figure 3-7 for both an on-axis focus and off-axis focus respectively. A single Fresnel pattern produces secondary lobe levels in the elevation dimension that are unacceptably high (-25dB), however, after

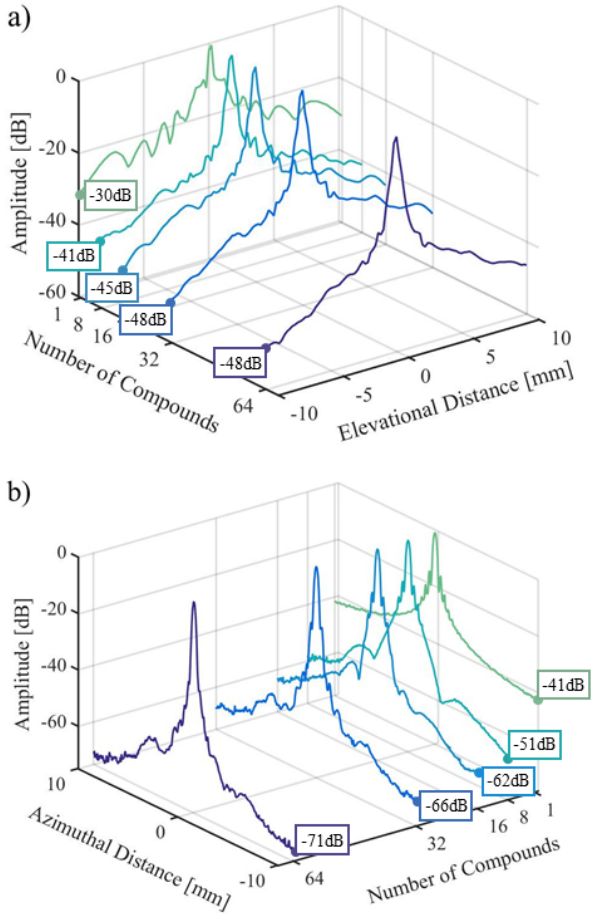

Figure 3-6 Simulated radiation pattern on axis for an increasing number of compounds in a) the elevation direction and b) the azimuth direction.

compounding multiple Fresnel patterns, the secondary lobes outside of the focus increasingly destructively interfere. After 64 compounds the secondary lobe levels in the elevation dimension are approximately -50 dB below the main lobe, which would be characterized as acceptable for many clinical applications. In the azimuth dimension, which is beamforming using conventional plane-wave compounding, the secondary lobe levels begin at approximately -40 dB with a single insonification, are suppressed to less than -65 dB after 64 compounds. The beamwidths achieved do not vary significantly with increasing compounds but it

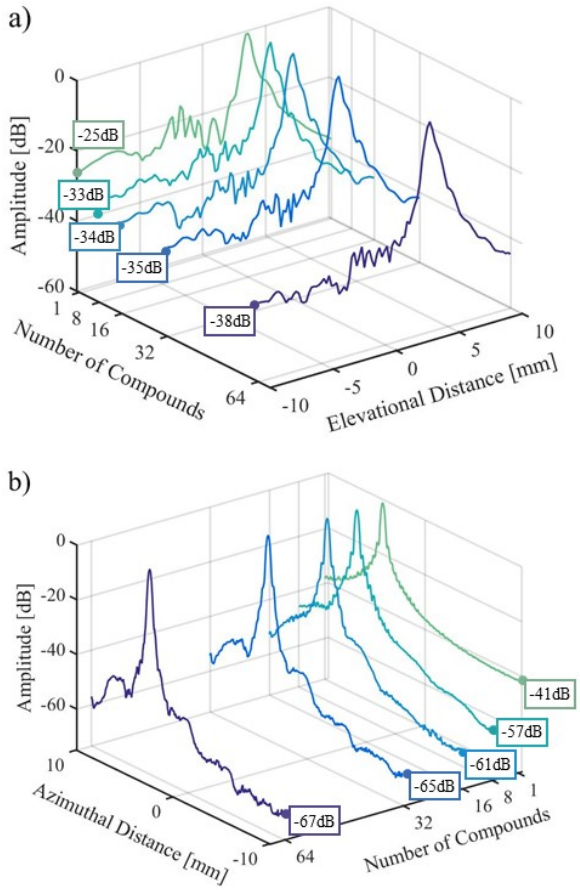

Figure 3-7 Simulated radiation pattern off axis for an increasing number of compounds in a) the elevation direction and b) the azimuth direction.

is the secondary lobe energy that shows the improvement. The simulations show a 531 µm -6 dB beamwidth in elevation and a 357 µm -6 dB beamwidth in azimuth for an on-axis focus. For a focus steered to the edge of the array the -6 dB beamwidth in elevation is 780 µm and in azimuth is 428 µm.

A problem inherent to approximating a Fresnel lens using a single Fresnel pattern is the degradation of axial resolution with steering angle. The pattern of positive and negative biases cannot correct for path length differences greater than half of a wavelength, therefore, when the path length delays are much

greater than λ/2 the combined pulses from across the array lead to an elongated, multicycle pulse. The pulse increases in length with increasing lens steering angle. We have previously described a split and delay sub-aperture technique that preserves axially resolution [2], however, this SAFE compounding technique can produce similar results without reducing the aperture size. The discrepancy between the element path length differences and the Fresnel phase adjustment creates destructive interference in the tail portion of the pulse while preserving the constructive interference in the first portion of the pulse. Figure 3-8 shows the pulse length when the Fresnel aperture is steered to the edge of the array and the drastic improvement after compounding. The axial resolution deteriorates with increased elevation steering angle. This example was chosen because it shows the worst-case scenario for the axial resolution. For this example, 64

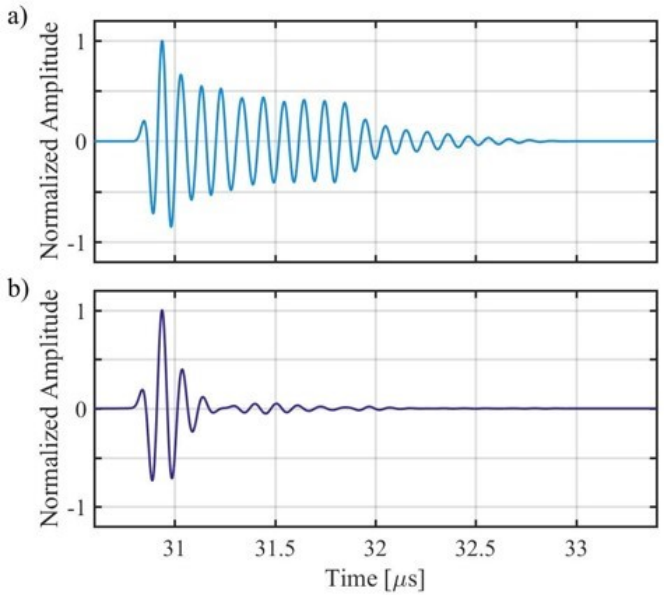

Figure 3-8. Simulated pulse at a focus steered to a wide angle using a) a single Fresnel pattern compared with b) 64 compounded Fresnel patterns.

compounds were used, and the ringing was suppressed by as much as 20 dB. The SAFE compounding approach can maintain axial resolution throughout the image window.

3.5 Electrostrictive Ceramic Transducers

Electrostrictive ceramic is not widely used in ultrasound literature, mainly because it is not piezoelectric without the applied bias. Apart from in specialized cases, the need for the bias complicates the system unnecessarily and the ceramic performance is approximately equal to many standard PZT compositions for imaging. The transducers in this thesis were built using PMN-PT (PMN38, TRS technologies, Penn State, PA, USA) [129], [130]. The performance properties of the electrostrictive ceramic have strong dependencies on temperature and bias voltage. Single element electrostrictive transducers were made to gain confidence

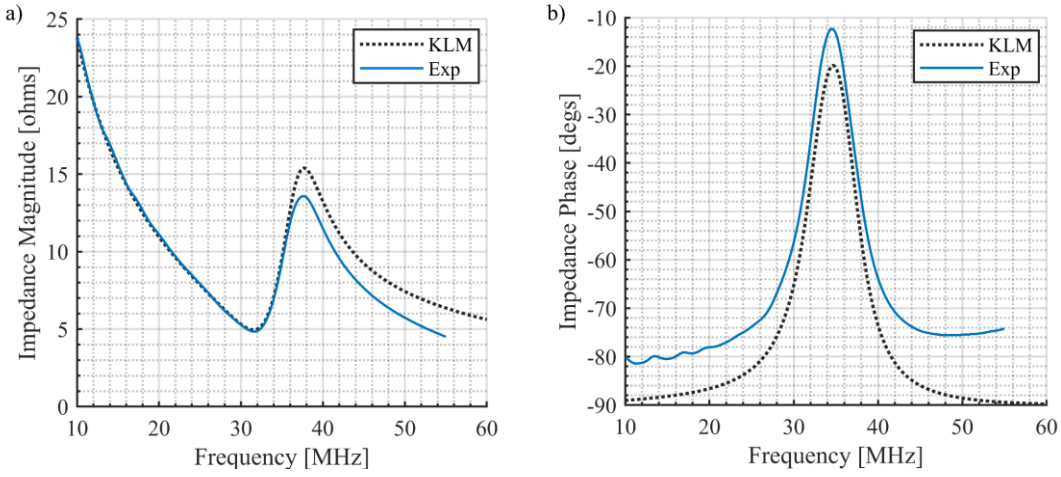

Figure 3-9 The measured impedance and KLM match for a 1 mm diameter, single element, PMN38 transducer.

Table 3-1 Electrostrictive ceramic properties of a single element transducer determined from impedance measurements 40 V (6.2 kV/cm).

Density	ρ	kg/m^3	7800
Dielectric constant	K^T		5800
Speed of sound	c	m/s	4770
Frequency constant	N_t	$Hz * m$	2020

in the material properties under the operating conditions of the crossed electrode array. The transducers were made from solid PMN38 ceramic discs (1 mm diameter) and backed with insulating epoxy (EPO-TEK 301 epoxy loaded with 3 µm alumina powder at 6 MRayl). The impedance of the unmatched transducer was measured in air and matched to a KLM model. Figure 3-9 shows the measured impedance from an example transducer compared with the simulated KLM impedance. The matched properties based on a 40 V (6.2 kV/cm) applied

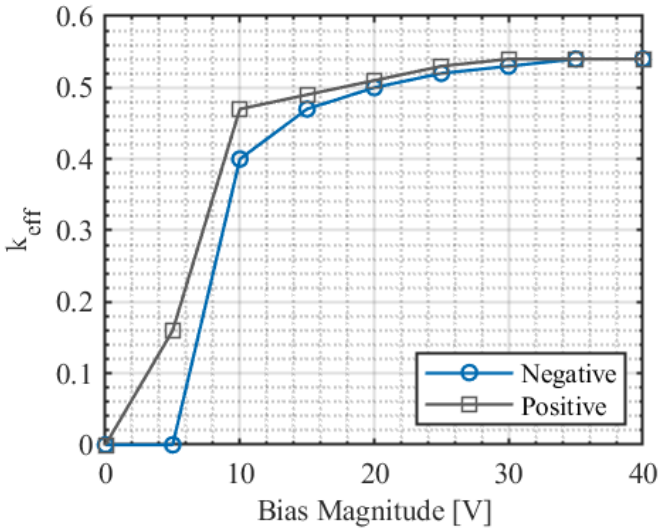

Figure 3-10 Effective electromechanical coupling factor as a function of bias voltage for a 1 mm diameter, single element, PMN38 transducer.

bias are shown in Table 3-1. The bias dependent properties can be easily demonstrated by measuring the impedance at increasing bias voltage amplitudes. Figure 3-10 shows the effective electromechanical coupling factor as a function of bias voltage for both a positive applied bias and negative applied bias. This captures the polarization behaviour in both directions in the thickness of the disc.

3.6 Array Fabrication

A 10 MHz, 64 x 64 element crossed electrode relaxor array was fabricated on an electrostrictive 1-3 composite substrate. A composite substrate was chosen to reduce crosstalk and increase the element directivity. The composite was made with a dice and fill method using electrostrictive ceramic (PMN38, TRS technologies, Penn State, PA) and EPO-TEK 301 epoxy (Epoxy Technology Inc., Billerica, MA). A micro dicing saw (DAD 3202, Disco Technologies, Tokyo, Japan) was used to cut 25 µm kerfs leaving 51 µm ceramic pillars (45% volume fraction). The composite design was chosen such that there are two composite pillars per array element to provide equal active material for each element and consistent ceramic surface area to aid in the wire bonding process. After dicing the substrate into pillars (Figure 3-11 a)) and filling the kerfs with epoxy, both sides were lapped flat and to thickness and copper electrodes were evaporated onto the front and back surfaces. The front and back-side elements were defined by scratch dicing the composite substrate with λ pitch using the same 25 µm

blade on the dicing saw. At the same time, the array was cut to its final size of approximately 10.3 mm x 10.3 mm, which leaves 230 µm of extra room on all sides to allow for space for the wire bonds outside of the active area of the array. An interposer board was designed to interface with custom high voltage biasing electronics. The board was made with a hole in the center where the array is mounted. There are wire bonding pads on both the top and the bottom of the board that align with the locations of the array elements. With the interposer board and the array mounted to a glass slide, 18 µm diameter aluminum wire bonds were placed to connect the wire bonding pads to the array element on the back-side (Figure 3-11 b)). An insulating epoxy (EPO-TEK 301 epoxy loaded with 3 µm alumina powder) was used to cover the backside wire bonds and act as a backing layer for the array. The alumina/epoxy composite was mixed with a 30% volume fraction which achieves a 5.5 MRayl acoustic backing impedance [131]. The array and interposer board assembly were flipped over and

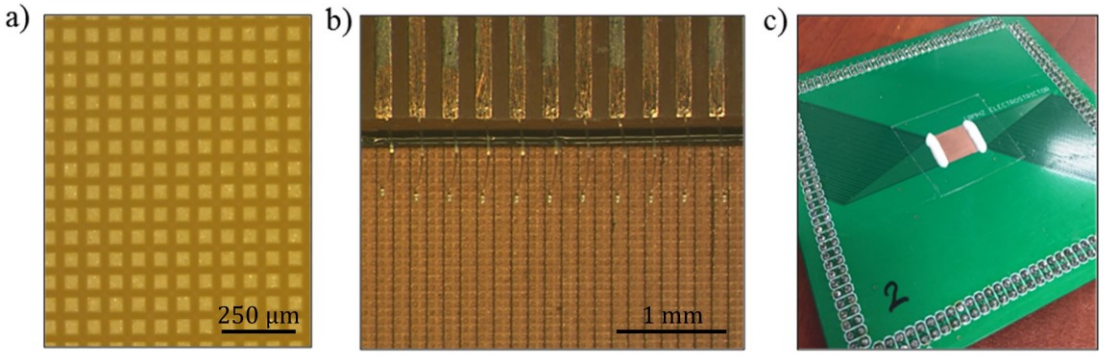

Figure 3-11 Fabrication steps showing a) the diced pillars of the 1-3 composite b) wire bonds for top side electrodes, and c) the completed crossed electrode relaxor array (10 mm x 10 mm array size).

wire bonds were placed connecting the interposer wire bonding pads to the front side elements. The wire bonds were covered with the same insulating epoxy. A single quarter wavelength matching layer applied by depositing 50 μm of Parylene-C (Specialty Coating Systems, Indianapolis, IN). The completed array is shown in Figure 3-11 c).

3.7 Array Characterization

Pulse echo experiments were completed by biasing the entire back-side of the array, pulsing a single element on the front side of the array, and measuring the echo reflected from the surface of the water bath (air-water interface). Figure 3-12 shows a representative pulse echo with a measured two-way pulse bandwidth of 60%. The center frequency was measured to be 10.9 MHz. The electrical impedance of individual array elements was measured using an RF impedance analyzer (4294A, Agilent Technologies Inc., Santa Clara, CA). The electrical impedance magnitude on resonance was measured to be 90 Ω with a phase angle of -35 degrees. The electrostrictive composite array has a measured electromechanical coupling coefficient (k_t) of 0.62 with a bias voltage of 90 V. Figure 3-13 shows impedance magnitude and phase curves for a representative array element.

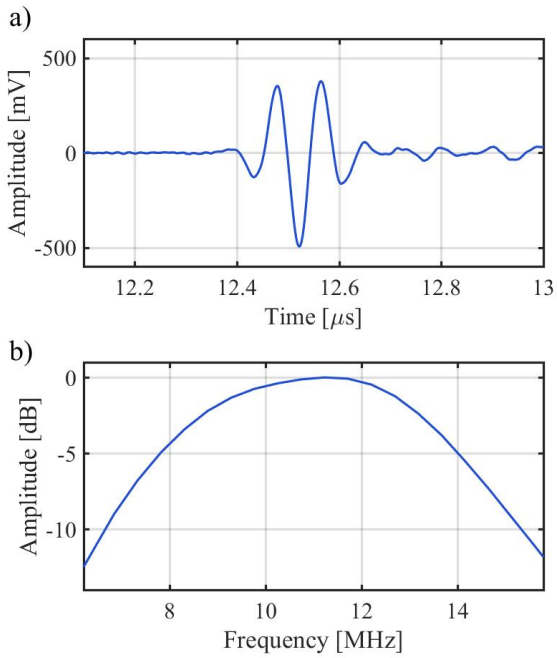

Figure 3-12 a) the pulse echo response of a single element off the surface of a water bath at a depth of 9 mm and b) the magnitude of the pulse spectrum.

The bias tunable response of the relaxor array is imperative for this new imaging technique to be successful. The relationship between pulsed response and bias voltage measured by recording the peak-to-peak pulse echo amplitude at increasing DC bias voltages, both positive and negative. The results are shown in Figure 3-14. Based on the material information for the electrostrictive ceramic

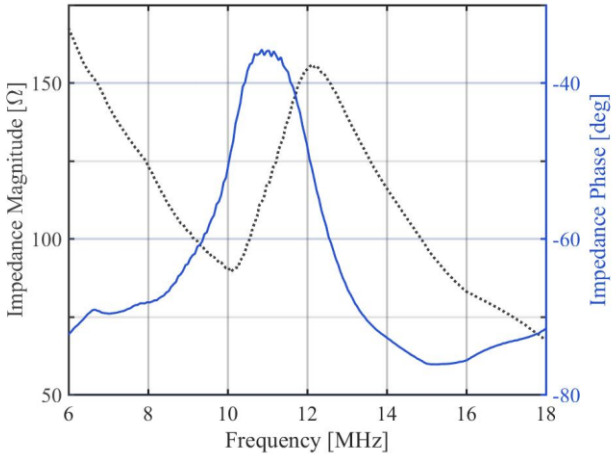

Figure 3-13 Impedance magnitude and phase of a representative array element.

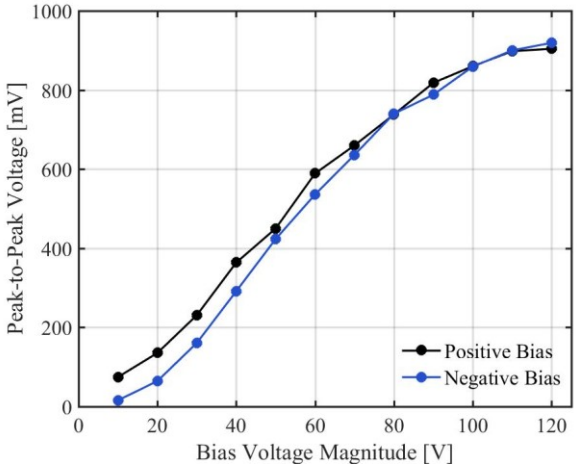

Figure 3-14 The pulse echo peak to peak amplitude with increasing bias voltage.

provided by TRS [129] the electromechanical coupling increases with voltage and plateaus at a bias voltage of approximately 5 kV/cm or 90 V for the 10 MHz array thickness. The amplitude response-bias voltage relationship agrees well with this specification, beginning its plateau near 90 V. The change in pulse polarity with the sign of the bias was confirmed with hydrophone measurements (Precision Acoustics Ltd., Dorset, UK). Figure 3-15 a) shows the measured pressure pulse with a positive bias and the opposite polarity pulse produced with a negatively biased array. Figure 3-15 b) confirms that once the bias magnitude surpasses a threshold value the phase does not change.

The electrical crosstalk was measured by applying a 3 cycle, 40 V pulse to the element under test, and measuring any voltage resulting on other elements on the array. The average nearest element and next nearest element electrical crosstalk was measured to be less than -31 dB. The next nearest element

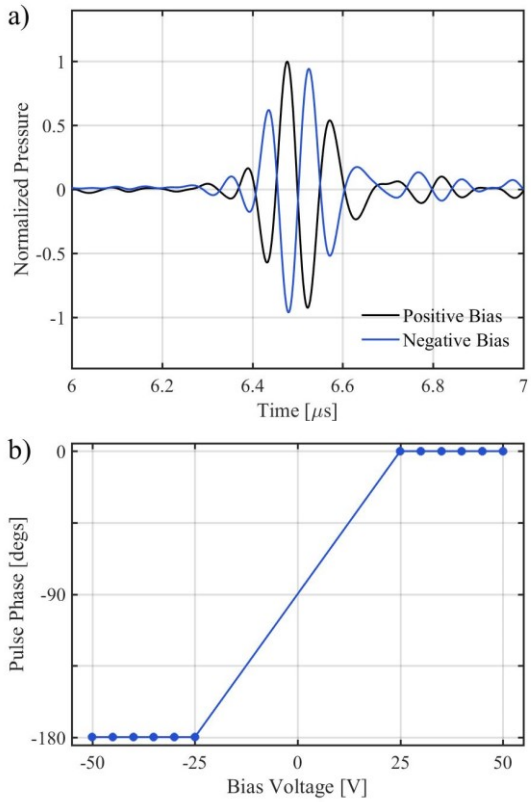

Figure 3-15 a) Normalized pressured measurements of the pulse from a single array element with a positive bias applied to the array and a negative bias applied to the array and b) Pulse phase measurements with changing bias voltage.

neighbors are also a focus because the even channels and odd channels lie close together on the interposer board and, for that reason, have the potential to interfere.

3.8 Experimental Results

Images were generated using a Verasonics Experimental Ultrasound System (Verasonics Vantage 256, Kirkland, WA) and a custom interface board containing the preamplifiers as well as the bias switching electronics. Bias control was achieved using a microcontroller controlling a bank of relays switching

between +60/-60 V biases and this circuit is described in [54]. The DC voltage rating of the relay banks prevented the operation of the array at maximum electromechanical efficiency. Plane-wave compounding was implemented in the azimuth while simultaneously compounding the Fresnel lens in elevation as described above. For each elevation slice, 64 simultaneous compounds were used per slice and a total of 32 elevation slices were collected. Radiation patterns were built in azimuth and elevation directions separately by imaging a single 18 µm wire target, at a depth of approximately 23 mm, oriented along the elevation and

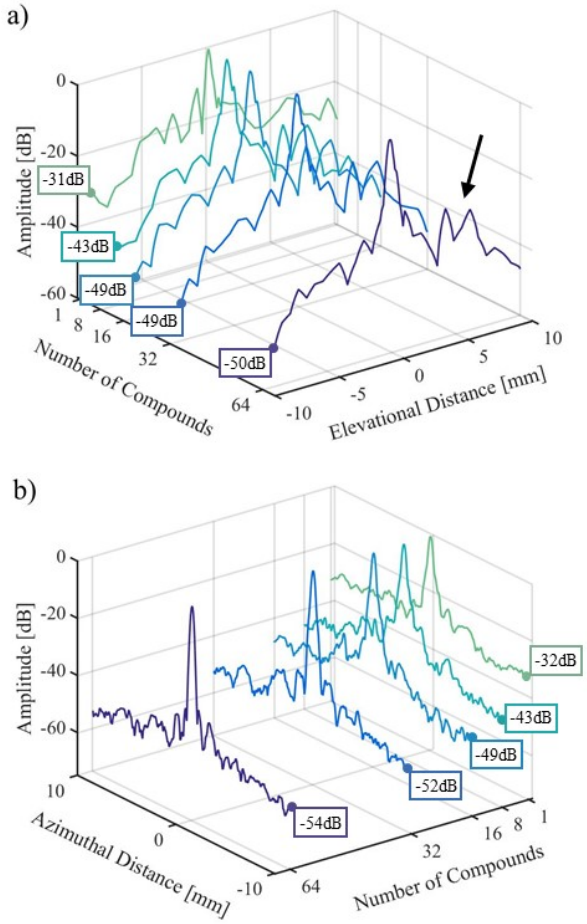

Figure 3-16 Experimental radiation pattern on axis for an increasing number of compounds in a) the elevation direction and b) the azimuth direction.

azimuthal directions respectively. The two-way radiation patterns across the elevation direction and azimuth direction for 1, 8, 16, 32, and 64 compounds are shown in Figure 3-16 and Figure 3-17 for both an on-axis focus and off-axis focus respectively. The radiation pattern produced using a single Fresnel pattern is highly variable. Some patterns create much more destructive interference in the secondary lobe areas than others. The single compound plots for the elevation direction show an example result. The experimental radiation patterns show a

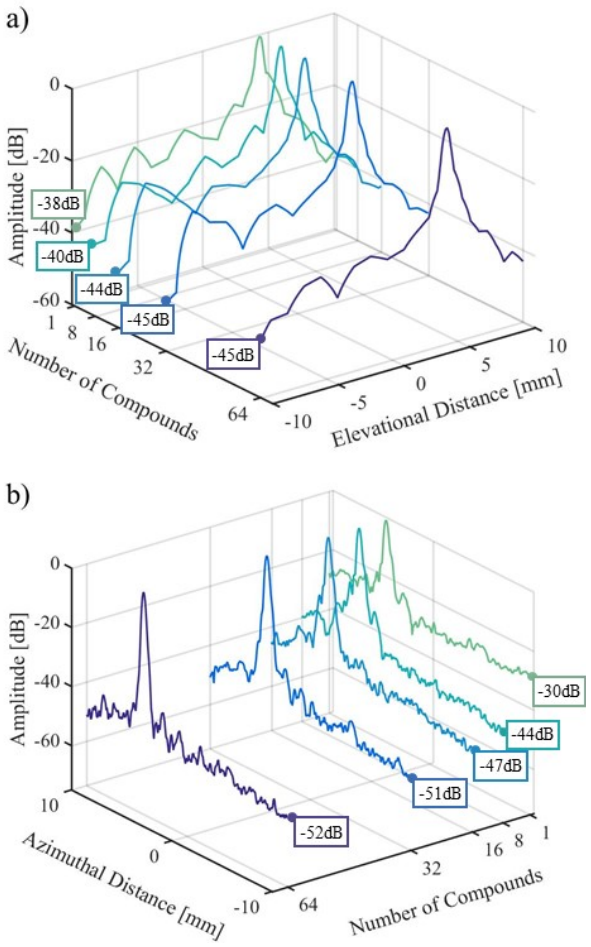

Figure 3-17 Experimental radiation pattern off axis for an increasing number of compounds in a) the elevation direction and b) the azimuth direction.

587 µm -6 dB beamwidth in elevation and a 380 µm -6 dB beamwidth in azimuth for an on-axis focus. For a focus steered to the edge of the array the -6 dB beamwidth in elevation was measured to be 718 µm and 429 µm in azimuth. The arrow in Figure 3-16 a) highlights a portion of the secondary lobe that was not suppressed as effectively as the opposite side of the radiation field. This is likely due to a defect in the array (e.g. damage to a portion of the array affecting a set of elevation elements) since it always occurred on the same side of the array no matter what set of Fresnel patterns were used.

2D images were generated by imaging a two-wire phantom in a water bath using the SAFE compounding technique, 32 elevation slices separated by 2λ were collected (i.e. a 3D volume) and images were reconstructed offline using MATLAB. The two wires (18 µm in diameter) were positioned perpendicularly to each other and were offset in depth by 4 mm. The images in Figure 3-18 show two elevation slices separated laterally by 8λ (1.2 mm) where the wire target in

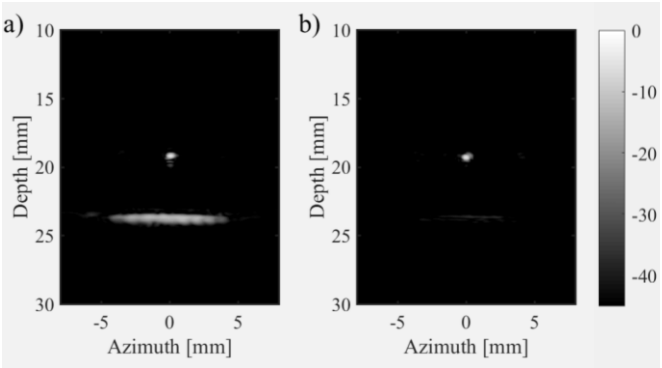

Figure 3-18 Experimental image of two perpendicular wires where (a) the on-axis elevational slice is selected and (b) the elevational slice 4 lines from center is selected. The image is displayed with 45 dB dynamic range.

parallel to the elevation planes is directly in plane for one slice a) and barely visible in the out of plane slice b). The images are displayed with 45 dB dynamic range and the decrease in signal from the wire in the out of plane elevation slice corresponds closely to the radiation patterns collected. This demonstrates the ability of the SAFE compounding technique to steer in elevation and collect a 3D volume.

Finally, a 3D rendering of the SAFE compounding image is shown in Figure 3-19. The image was reconstructed from 32 elevational image slices. The bump in the elevational side lobe is also shown in the 3D image. The image was rendered using 3D Slicer software [132] and is displayed by making the pixels below -40 dB transparent. The artifact resulting from what is assumed to be a defect in the array can also be visualized on one side of the wire target in the elevation

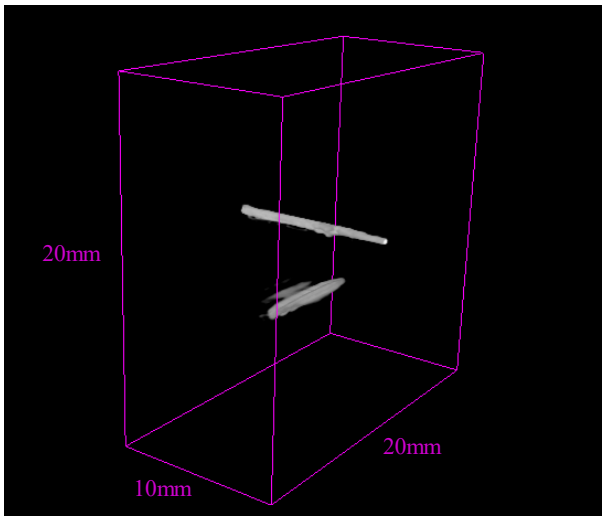

Figure 3-19 Three-dimensional rendering of the SAFE compounded 3D image. The image is displayed with 45 dB dynamic range.

dimension. The level of this artifact agrees very closely with the secondary lobe levels measured on one side of the radiation pattern (- 26 dB see Figure 3-16 a)).

3.9 Discussion

This study demonstrated the concept of an electrically reconfigurable lens on a crossed electrode array for 3D imaging. More broadly, an approach to imaging in a 2D plane that requires only a single RF channel and bias control across the array. This solves the problem of being unable to beamform the overlapping azimuthal and elevational elements on a crossed electrode array simultaneously. The azimuthal elements were beamformed normally and the electrically reconfigurable Fresnel lens was used to select the elevational slice in the 3D volume. Both the azimuth and elevation planes were compounded simultaneously to improve image quality in both dimensions. Because the SAFE compounding approach is implemented on a crossed electrode array, it requires only $2N$ electrical connections to the array. The only other complexity added, compared with a 2D imaging system, is N controllable DC bias channels. While plane wave imaging was the modality chosen to demonstrate the imaging and compounding in the azimuth direction this approach could be implemented with other 2D imaging techniques. As an example, diverging wave imaging also requires compounding to improve imaging quality and would increase the width of the imaging window.

The crossed electrode array has the advantage of larger effective element size compared with a conventional 2D grid array, therefore, the element impedance is much lower in the crossed electrode array. In addition, the electrostrictive ceramic has a large dielectric constant which also decreases the impedance given the element area. The result in the final 10 MHz crossed electrode array design with a single element impedance of 90 Ω on resonance while biased. This element impedance matches the cable impedance (75 Ω) and pre-amplifier closely enough to maintain signal sensitivity with no electrical matching required.

The SAFE compounding approach was demonstrated first in simulation then using a custom 10 MHz, electrostrictive composite crossed electrode array. When interpreting the Fresnel compounding results, it is important to note that the result from a single Fresnel pattern is variable, some patterns produce better radiation patterns than others. For example, one pattern might produce a narrow, tightly focused main lobe but have high constructive interference in the secondary lobe region. Another pattern might have a better balance between main lobe width and secondary lobe energy. The results shown both in simulation and experiment for the single Fresnel compound are representative examples and not a best or worst case. When compounded, the simulated radiation patterns show secondary lobe levels just below -50 dB with a main lobe width comparable to a conventional beamformed focus. The radiation patterns in the azimuth

direction are largely unaffected by the Fresnel dimension. Although the simulations in this study were used to investigate the compounding results using different sets of Fresnel patterns, optimizing the set of patterns used is part of the suggested future work. We expect to be able to improve the destructive interference produced through compounding by choosing Fresnel patterns that optimally cancel each other out in the off-axis regions. Also, the Fresnel pattern can be changed between transmit and receive. If the receive Fresnel pattern is chosen based on the pressure radiation pattern produced by the transmit Fresnel pattern, the single transmit/receive Fresnel focus can be optimized. Complementary transmit/receive Fresnel patterns can be determined by choosing a receive Fresnel pattern that produces nulls in pressure where the transmit pattern produced peaks and vice versa.

In the azimuth direction, the main lobe width matches simulation, but the secondary lobe levels deviate from simulation (54 dB in experiment vs. 71 dB in simulation). In the elevation direction, both main and secondary lobes match simulation. However, the radiation pattern has an additional pedestal shape not anticipated by simulation. The -6 dB beamwidths in both planes are given in Table 3-2. The discrepancies between the secondary lobes in the azimuth direction, as well as the elevation radiation pattern, are likely due to using a line

Table 3-2 Comparison of simulated and measured -6 dB beamwidths.

	Simulation	Experiment
	On-axis	
Azimuth	357μm	380μm
Elevation	531μm	587μm
	Off-axis	
Azimuth	428μm	429μm
Elevation	780μm	718μm

wire target (opposed to a point target in simulation) and the associated challenges in wire target alignment. In addition, five dead elements became open-circuited during the fabrication process that would have contributed to the discrepancies between the simulated and experimental radiation patterns. These values are within expected error given the discrepancies between the ideal simulation and the challenges in experimentation.

An unexpected and interesting advantage of compounding the Fresnel patterns is the regaining of the axial resolution of the compounded pulse off to wide elevation steering angles. By compounding a set of Fresnel lenses focused to slightly different locations, the extended pulse inherent to Fresnel type beamforming is shortened and the disadvantage of having a long element path length across the array is eliminated without adding any more complexity. This effect may be optimized by tailoring the set of Fresnel patterns that optimize the destructive interference in the tail portion of the pulses at wide elevation angles.

The imaging window in the azimuth direction was limited only by the compound imaging technique employed (i.e. plane wave, diverging wave, etc.) and therefore, is capable of steering to conventional phased array steering angles. In this initial proof-of-concept study, plane wave imaging was implemented and the width of the image window is approximately equal to the width of the array aperture. In the elevation dimension, however, there are more limitations on how wide of an angle the Fresnel lens can still produce high quality focused beams. Steering past angles of approximately ± 15 degrees results in rapidly increasing the level of secondary lobes and the pulse lengths become prohibitively large.

Performance in the elevation dimension can also be further improved by reusing the data collected for neighboring elevational slices in the current slice. If the neighboring slice data is phase corrected for the current slice, this effectively increases the number of elevational compounds. The improvement in elevational imaging performance comes without a cost to frame rate because the data is reused. Because the phase difference across the field of view for each Fresnel pattern is being compensated, the focus does not have to be directly on top of the elevational image slice to contribute to the compounded focus. Therefore, the Fresnel patterns that focus to the elevational slice on either side of the current slice can be used if we adjust the phase compensation to the current slice. In doing so transmit events are recycled and the volumetric frame rate increases. Figure 3-20 shows the two-way radiation patterns for 64 compounded Fresnel

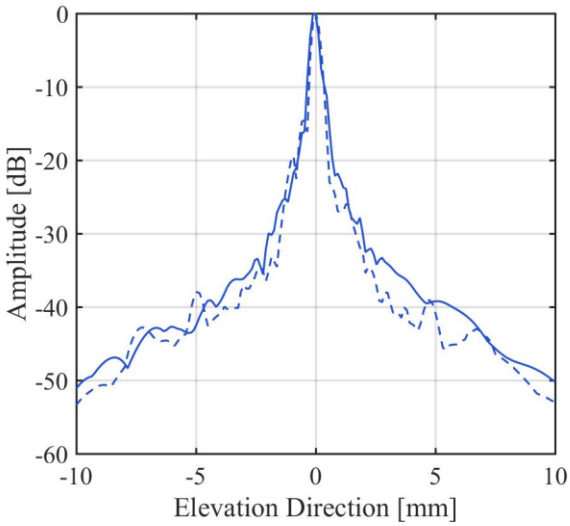

Figure 3-20 Simulated radiation patterns compounding with 64 Fresnel patterns on a single elevation slice (solid) and compounding with 63 Fresnel patterns split across three neighboring slices (dashed) resulting in a 3x frame rate increase without any loss in beam quality.

patterns on a single elevation slice compared to the result when using 63 compounded patterns total, but by reusing the data from three neighboring elevational slices (21 compounds per slice). In this case, the extra 42 patterns were re-used from elevation slices on either side of the current slice and, therefore, do not contribute to increasing the frame rate. The frame rate is effectively increased by 3x with no effect on the elevation beam. Alternatively, the neighboring slice approach could be used to maintain the same frame rate, while increasing the quality of the elevation radiation patterns. The image quality and frame rate can be optimized by adjusting the number of compounds per slice and reusing the data from neighboring slices for a given application. An added advantage of multi-slice compounding with more Fresnel patterns focused to

different spatial locations is increased axial resolution at wide steering angles (more destructive interference in the tail of the pulse).

The frame rate using the SAFE compounding approach is determined by the number of compounds chosen per elevation slice and the number of elevation slices to complete the volume. If a pulse repetition frequency is chosen based on the time-of-flight for a 5 cm depth with 64 compounds per slice and 32 elevation slices per volume, a frame rate of 7.4 volumes/s can be achieved. Continuing the example of reusing the neighboring elevation line data, if 21 Fresnel patterns are used per elevational imaging slice the frame rate would increase to 22.5 volumes/s with equivalent elevation slice selection resolution. Montaldo et al. [47] measured the increase in plane wave image quality with increasing number of compounds. Their results show no increase in resolution and only a moderate increase in contrast and SNR after 45 compounds. Using 45 compounds in our SAFE compounding approach would decrease the frame rate to 10.5 volumes/s but further improve the elevational beam profile if neighboring elevation slices were re-used as described above. For our desired 30 MHz endoscope, where the pulse repetition rate is based on a time of flight for at most a 20 mm depth, the volumetric frame rate would be increased by 3x. It should be noted that the volumetric frame rates suggested are the PRF limited frame rates and rely on the hardware and software having the ability to keep up with the data acquisition and beamforming arithmetic. This should be feasible as the complexity of this

technique is very low. A volume image is equivalent to generating 32 sequential plane-wave images while simply varying the DC bias of the elevation electrode pattern.

A case could be made for replacing a conventional passive acoustic lens on a 1D array with an electrically reconfigurable Fresnel lens and implementing SAFE compounding for 2D imaging. The compounded Fresnel lens produces a beamwidth marginally larger than from an acoustic lens (490 µm vs. 380 µm respectively, from simulation), however, the depth of field of the focus of the Fresnel lens is much larger than the acoustic lens. Figure 3-21 compares a 2D map of the two-way radiation pattern for a compounded Fresnel lens and an ideal

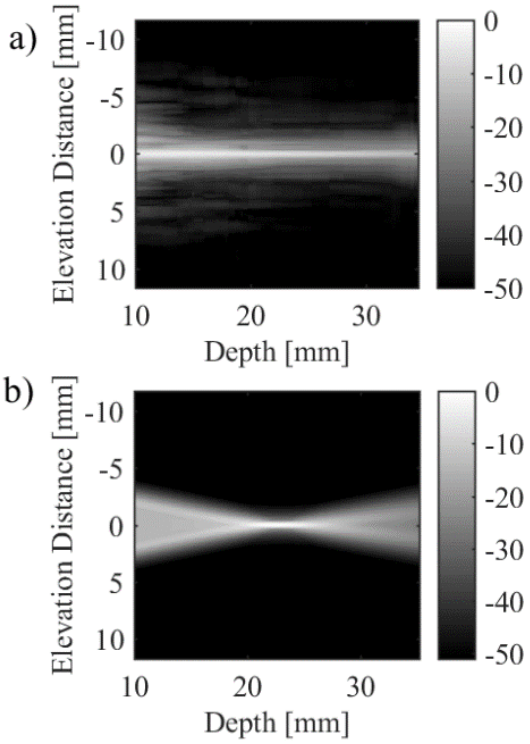

Figure 3-21 Two-way simulated radiation pattern from a) Fresnel lens compounded 64 times and b) an ideal acoustic lens.

mechanical acoustic lens (no attenuation modelled). The collimation of the energy improves slice resolution at depths outside of the lens focus. In addition, there is the advantage of having no attenuation through a physical lens medium, which becomes increasingly important at higher frequencies. High frame rates could still be achieved even though compounding is required to improve the Fresnel lens quality if a compounding approach is simultaneously used in the azimuth dimension.

The SAFE compounding technique is a novel 3D imaging approach that uses the ability to simultaneously improve image quality along perpendicular imaging planes to generate high frame rate 3D images. This study has demonstrated the performance of the 3D imaging technique on a custom 10 MHz electrostrictive composite crossed electrode array using offline image reconstruction.

CHAPTER 4

A 30 MHZ, 3D IMAGING, FORWARD-LOOKING MINIATURE ENDOSCOPE BASED ON A 128-ELEMENT RELAXOR ARRAY

4.1 Preamble

This chapter largely includes content accepted for publication (In press) in IEEE Transactions on Ultrasonics, Ferroelectrics, and Frequency Control under the same title. Any introductory material previously covered in the Background Chapter has been removed or reduced for conciseness. Modifications have been made to unify this document both in terms of nomenclature and formatting as well as providing a clearer story of the relevance in the evolution of the project. Permission has been granted by IEEE to include the figures and data published in the paper in this thesis. The main goal of this second study was to fabricate and demonstrate the performance of a high frequency crossed electrode array packaged into an endoscopic form factor, using the imaging technique described in the first study (Chapter 3).

4.2 Introduction

Miniaturized ultrasound imaging arrays have many potential clinical applications, specifically, in guiding surgical procedures. The ability to image from within the body enables valuable real-time guidance for minimally invasive surgical approaches. Recently, considerable research effort has been put towards miniaturizing one-dimensional linear ultrasound arrays for endoscopic applications [128], [133]–[137] (intravascular, intracardiac, spine, laparoscopic, neurosurgery, etc.). The inherent strengths and drawbacks of high-frequency transducers align well with these applications by providing high resolution yet low penetration depth images. By miniaturizing the form factor into a small endoscope, applications requiring visualization of fine anatomical structures from within the body are possible.

3D capable probes are also particularly suited to endoscopic applications because of the large amount of information that can be gathered without being sensitive to the position of the tool in a confined space from within the patient. A 3D dataset can provide information in hard to access planes, accuracy in volume measurements and flexibility in image display.

Unfortunately, the inherent fabrication challenges for miniaturizing a high-frequency linear array are made exponentially more challenging for a 2D array. Most of these challenges relate to the huge number of very small elements.

Generally, the electrical interconnect takes up a significant percentage of the endoscope package, even for the case of just a 1D array. Squaring the number of connections for a 2D array presents major challenges, specifically, in developing a fabrication process for making the electrical connections that will also fit into miniaturized packaging. Previous work has shown 2D arrays that have been miniaturized, however, at lower operating frequencies (5-10 MHz) [138]–[144] and, with relatively small apertures to fit in endoscopic catheters (7-14 Fr for forward-looking devices). The applications targeted for these devices include intracardiac echocardiography (ICE), transesophageal echocardiography (TEE) and laparoscopic surgical guidance. The electrical connections are made on the back of the forward-looking 2D grid arrays using high-density multilayer flexible circuits. The connection between the array elements and pads of the multilayer flexible circuits are made using conductive epoxy, however, these circuits have a minimum pitch of 150 µm [145]. A similar approach utilizes fine (20 µm) pins attached in a grid to the interconnect board [146]. The pins can be pressed into a conductive backing to complete the electrical connections. Still, the pitch is restricted to 110 µm or greater with this technique.

The number of connections and bulk of the cables feeding through a catheter can be minimized by applying a sparse array design [70], [140], however, images collected with sparse arrays suffer from low signal to noise ratios since only a small percentage of the array is active for each transmit event. Alternatively,

fully sampled 2D arrays have been built that use application specific integrated circuits (ASICs) to perform some beamforming and multiplexing within the probe minimizing the number of cabled connections to the beamformer electronics, where the final beamforming is completed. This staged beamforming approach results in increased image quality over sparse 2D arrays because the whole aperture can be active on transmit and receive [64], [147], [148]. There has been recent work in developing ASIC integrated devices using both piezoelectrics [149] and CMUTs [150] in miniaturized packaging for intracardiac and general endoscopic applications. These devices operate in the 5–7 MHz range. The work in forward-looking intravascular ultrasound (IVUS) imaging devices are more closely relevant to this study since the operating frequencies are up to 13-20 MHz [151]–[155]. The device presented by Janjic et al. [151] has a total of 80 elements (16 transmit and 64 receive) in an optimized spatial arrangement and requires only four coaxial cables fed down through the catheter. Gurun et al. [154] created a dual ring design in their forward-looking device with a 56 element transmit ring and a 48 element receive ring using only 13 coaxial cables. Both examples show promising imaging results but the constraint of fitting onto a catheter has forced the aperture to become small relative to the operating frequency.

An alternate way to reduce the number of beamforming channels is to change the type of array architecture. Using a crossed electrode (row-column, Top Orthogonal to Bottom Electrode) array design requires only $2N$ elements rather

than the N^2 elements required for a fully sampled 2D array aperture. However, even using $2N$ elements, there remain practical challenges in packaging a high-frequency crossed electrode array into an endoscopic form factor. Specifically, the issue of how to connect to elements on the front and back-side of the array without adding bulk to the packaging. Many groups have fabricated versions of the crossed electrode array [75], [76], [78], [81], [82], [85], [90], [156], [157] with some notable examples of using the bias sensitive nature of CMUTs [75], [82], [85], [156], [158]. However, up to now, there has not been a focus on either high-frequency devices or miniaturization.

Small animal imaging is a well-established application for high frequency ultrasound imaging [159], [160]. Probes with small packaging have an advantage in small animal imaging because it makes clear exactly what region is being imaged due to the small profile. In addition, and only a small acoustic window is required. This allows, for example, just a small craniotomy window for rodent brain imaging, which is an exciting new application in pre-clinical imaging [161]–[164]. The miniaturized device presented here is packaged suitably and has an appropriate center frequency for this application. A 30 MHz center frequency is capable of between 15 and 20 mm of tissue penetration, more than the full depth of mice and rat brains.

For clinical applications, I believe that the probe is suitable for guiding several minimally invasive surgical procedures. The overall trend in modern

surgical techniques is to move towards minimally invasive procedures, where the operation is performed through a small burr-hole or key-hole. This type of surgery has the advantage of faster recovery times, less blood loss, etc. since the entire operation is performed using only small sub-5 mm endoscopic tools. Unfortunately, conventional ultrasound probes are too large to follow the surgical pathway and are limited to imaging from the surface. Although the probe described in this paper could be modified to be suitable for several endoscopic procedures by adjusting the frequency and aperture size for the given application, there are a couple applications that the Authors believe this aperture and frequency are suitable for: Burr-hole neuro-surgery, and general spine surgery. Recently, there has been some exciting studies in both 2D and 3D ultrasound imaging of the brain during large craniotomies where larger more conventional probes are used [165]–[167]. A 5 mm endoscope, however, will fit down the surgical pathway in burr hole neural surgeries created by the aspirator (e.g. The CUSA). The choice of a 30 MHz center frequency was determined based on in-house human cadaver brain imaging and the resolution required to visualize tissue margins between primary tumors and healthy tissue. Defining the margin to resect is often very challenging in many brain tumor resections using optical surface imaging alone and defining too large or too small of a margin around a tumor both have severe consequences. For example, removing acoustic neuromas without cutting into the either the brain stem or auditory nerve is an extremely

delicate procedure. The center frequency might again shift up or down for a given tumor type and size. For example, it may be more desirable to have a larger visualization window for guiding the resection of large sprawling glioblastoma tumor and therefore a lower center frequency might be more optimal. However, the size of the endoscope would typically be required to remain sub-5mm in order to follow the surgical pathway of the aspirator. To accommodate the requirements for these types of procedures the probe handle would be adjusted to a bayonet style, which would allow for guidance of probe placement with a surgical microscope.

Spine surgery is another surgery that is rapidly moving towards a minimally invasive approach. In these procedures, the ability to visualize the small nerve rootlets coming from the spinal cord and located in the cerebrospinal fluid would be of great benefit to the surgeon, as this would allow them to directly check for nerve decompression. Again, we believe that the aperture size and frequency are close to optimal for these procedures as 30 MHz can penetrate the whole spinal cord and has enough resolution to clearly visualize and check for compressed nerve rootlets. Due to the limited size of the access window and the long pathway to reach the spinal cord, the endoscopic instruments need to be sub-5mm in size. The length of the endoscope current prototype would need to be extended to a total length of approximately 15 cm.

Our approach to a 3D capable endoscopic ultrasound device was to build a 30 MHz, 128 element (64 x 64) crossed electrode array on a 1-3 relaxor composite substrate. A new fabrication process was developed, that utilizes a picosecond 355 nm laser to micro-machine the 30 MHz composite substrate and 64 x 64 orthogonal elements. A process has also been developed that uses a thinly diced strip of flexible circuit board to bring the back-side connections to a front-facing bond surface, which allows the final size of the forward-looking endoscope to measure only 6 mm x 5 mm. The design, fabrication, and characterization of this 128-element crossed electrode array in a miniature endoscopic form factor is described in detail.

4.3 Array Design

The crossed electrode array was designed for 30 MHz center frequency with an element-to-element pitch of just under one wavelength (48 µm). The array substrate has 64 elements on the top and an equal, orthogonal set on the bottom. The design choice of 64 elements at 48 µm pitch was made for multiple reasons. First, our group has previously developed a custom 64 channel, high-frequency beamformer [168]. To utilize this resource for this 3D imaging array, we were limited to 64 beamforming channels. For each 64-element side of the array, 48 µm pitch was chosen to maintain an aperture size that provided high lateral resolution, and grating lobes located at sufficiently wide angles (greater than +/-

30°). Moreover, at 30 MHz, reducing the pitch any further would require an element fanout pattern so that the electrodes were large enough for wire bonding.

The array was fabricated on a 1-3 composite substrate. There are two main advantages of a composite that generally drive the design choice for this transducer. First, the high percentage of epoxy significantly lowers the acoustic impedance of the composite compared to a solid piezoelectric ceramic. Therefore, the acoustic impedance of the array is more closely matched to tissue and eliminates the need for more than one matching layer to achieve acceptably broad bandwidth ($> 60\%$). Second, the piezoceramic is no longer clamped laterally, thus, it operates more efficiently in pillar mode. The electromechanical coupling coefficient of a composite material is designed to be higher than bulk ceramic operating in plate mode. In addition to these two general advantages for the design of the array substrate, the composite was also chosen to increase the mechanical separation between elements and increase directivity. A two pillar per element composite design was chosen to ensure equal active area across elements. The composite has 17 µm pillars and 7 µm kerf, corresponding to a 50% volume fraction and a pillar aspect ratio of 3.

Previously, fabrication of a composite near these dimensions has not been successful using a mechanical dice and fill method. The pillars either break from the base or sustain microcracks from the mechanical dicing process. This composite was cut using a laser dicing process and the laser used was a custom

355 nm (8 µJ/pulse, 30 ps pulse length), picosecond laser (Oxford A-Series Laser System, Oxford Lasers Ltd, Oxford, United Kingdom) with an adjustable focal spot size down to 3 µm and 3-axis positional resolution of 50 nm and repeatability within 80 nm. The laser machining approach can make very narrow, high aspect ratio cuts with very little mechanical damage and very little heat damage.

The 3D imaging approach developed for this crossed electrode array design, as described in [5], [9], requires that the polarization direction across the substrate be electrically controllable. An electrostrictive ceramic (PMN38, TRS technologies, Penn State, PA, USA) was chosen because its piezoelectric properties depend on a DC bias and the polarization direction can be reversed by changing the sign of the applied bias. Elements of an electrostrictive array can also be effectively turned off by removing the DC bias. This flexibility increases the number of possible imaging techniques to implement on the crossed electrode or row-column array architecture. For these purposes, the back-side elements along the elevation dimension are designated bias channels. The front-facing elements along the azimuth are reserved for signal channels.

A simple bias tee network is used on each bias channel to separate the low frequency, bias electronics from the high frequency pulser (Figure 4-1). The bias tee provides a low resistance path from the front-side signal element through to the back-side and RF ground. The bias ground path is through RF ground using

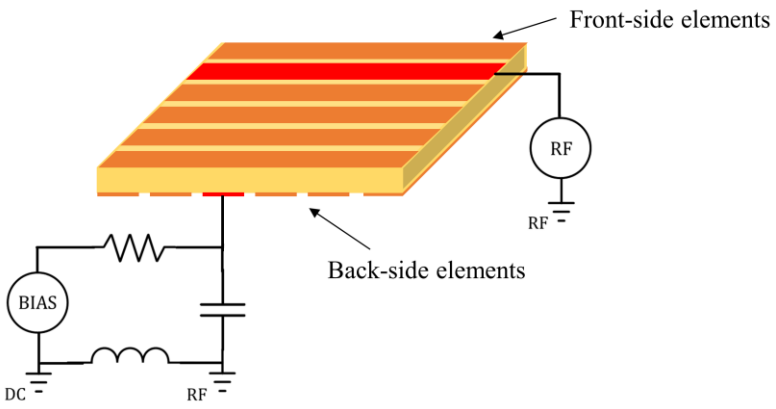

Figure 4-1 Schematic of the bias passives and their connection between front-side signal channels and back-side bias channels.

an inductor. The components of the bias tee were chosen to filter the sharp transitions of the bias switching, reducing any erroneous pulsing from the bias transitions.

4.4 Fabrication

The main fabrication steps are outlined in a diagram in Figure 4-2. The fabrication process began with laser dicing a 1-3 composite pattern from a 5 mm x 5 mm ceramic sample (PMN38, TRS technologies, Penn State, PA, USA). The diode pumped, solid state picosecond laser dicing system was used to create the 7 µm wide kerfs. The laser dicing path was defined so that only every other line was cut from one edge of the sample to the other. The sub-diced lines were then cut to span only the final size of the active array (3.1 mm). This pattern was chosen so that there would be solid ceramic under the wire bonding pads to promote well adhered, robust bonds. The alternating kerf lines between elements

were cut to the edge of the sample so that the epoxy fill would wick into the kerfs without trapping air. The perpendicular kerfs were then made completing the definition of the square composite pillars (Figure 4-2 a)). After laser dicing, the composite was filled with epoxy (West System epoxy, Gougeon Brothers Inc., Bay City, MI, USA) and, after curing, the excess epoxy was lapped away to just a few microns less than the original sample thickness (Logitech PM5, Glasgow, Scotland). The lapped composite is shown in Figure 4-3 a). A chrome-copper electrode layer was vacuum deposited and then the laser was used to etch the

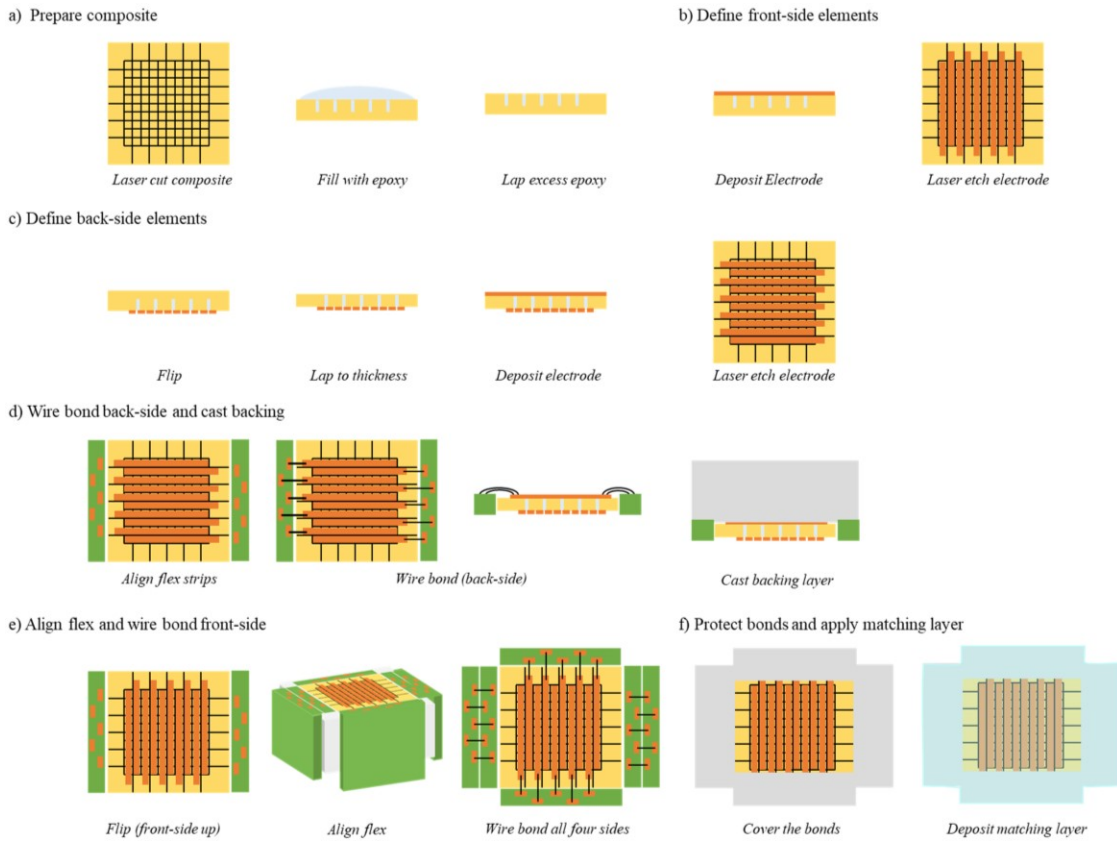

Figure 4-2 Diagram outlining the steps of the fabrication including, a) preparing the composite, b) defining the front-side elements, c) defining the back-side elements, wire bonding the back-side and casting the backing layer, e) aligning the flex boards and wire bonding the front side and f) protecting the bonds and applying the matching layer.

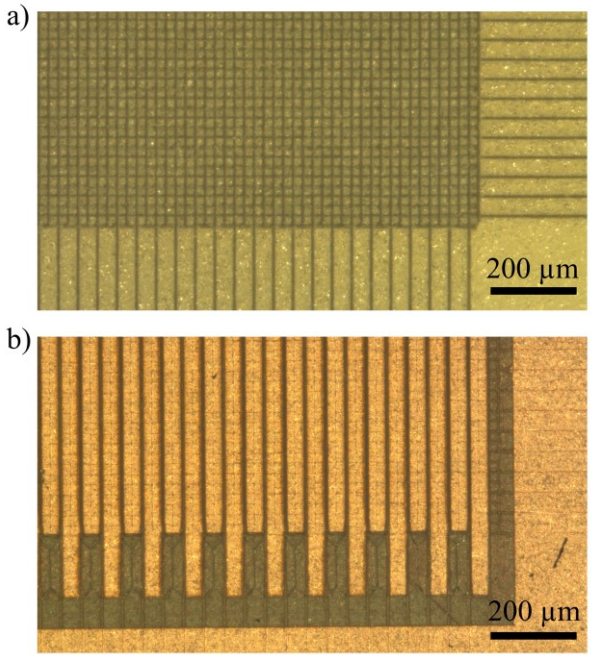

Figure 4-3 Photograph of a) the laser diced composite pattern after filling and lapping and b) the electrode pattern after laser etching.

array electrode pattern in alignment with the pattern of composite pillars (Figure 4-2 b)). Aligning the elements with the composite pillars promotes good element to element uniformity and maximizes the active area of the elements. The pattern was defined as 40 µm wide elements with 8 µm spacing, shown in Figure 4-3 b). The elements are extended on alternating sides to provide wire bonding pads on top of the solid ceramic sections of the substrate. The bonding pads do not overlap with the active transducer area. This set of electrodes will become the front face of the crossed electrode array. Next, the composite was flipped and re-bonded to a glass slide. The composite was lapped to its final thickness of 55 µm and the second chrome-copper electrode was vacuum deposited. The second, orthogonal electrode pattern was laser etched in the same manner as the first and

was once again aligned with the composite pillars (Figure 4-2 c)). The substrate was then mechanically diced to the final, unpackaged array size, approximately 3.1 mm x 3.1 mm. At this step the composite array substrate with front and back-side elements defined was complete.

The crossed electrode array design requires $2N$ electrical connections compared to N connections for its 1D counterpart. Previously, a wire bonding and miniaturized packaging design was presented by Bezanson et al. [134] for a 1D array. It was developed for the fabrication of a 45 MHz endoscopic phased array. In this technique, the acoustic stack is fixed to the end of a plastic mount and the flexible circuit boards are laid flat along a side of the mount with the end flush with the face of the array. The flex circuits are manufactured with either solid filled copper vias or thick copper traces and the thickness of the trace acts as the wire bond pad. The array elements were then wire-bonded to the thickness dimension of the flex circuit avoiding any bend radius associated with conventional flexible interconnects. Using this technique, the 45 MHz, 64 element phased array was packaged with a final size of less than 3 mm x 3 mm.

The method for electrically connecting to the $2N$ crossed electrode array is an important design step for miniaturizing this 2D forward-looking endoscope because the electrical connections can take up a significant portion of the endoscope profile. The main challenge that was not present in the 1D array design, is miniaturizing an interconnect that enables the electrical connections to

both the front and back-side elements while adding minimal bulk to the profile of the endoscope. We incorporated the approach from the 1D array for wire-bonding the front face electrodes but have developed a new technique to bring the back-side connections to the front side. In doing so, four flexible circuit boards can be placed along the four sides of a plastic mount with the array on its tip.

The back-side connections were brought to the front by unconventionally utilizing the flex. When a thin strip is cut off the end of the flex circuit board (approximately the thickness of the array) the thick copper traces provide a solid connection from the back-side to the front (Figure 4-4). The flex strip was fixed with wax beside the array and the wire bonds to the back-side elements were connected (Figure 4-5 a)). A backing layer made of insulating epoxy (EPO-TEK 301 epoxy loaded with 3 µm alumina powder) was cast to the back of the array, covering the 64 bonds (Figure 4-2 d)). The alumina/epoxy composite was mixed with a 35% volume fraction which achieves a 6 MRayl acoustic backing

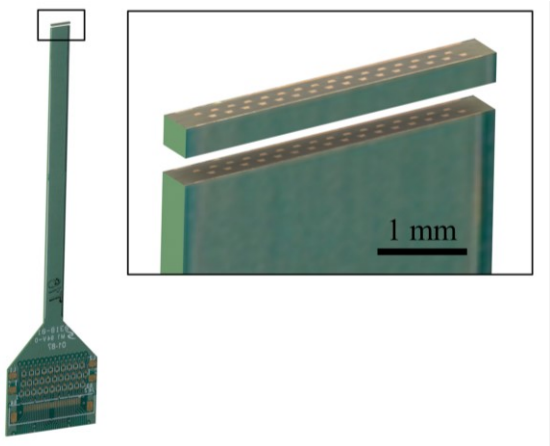

Figure 4-4 The strip of flexible circuit board used to bring the back-side array connections to the front face.

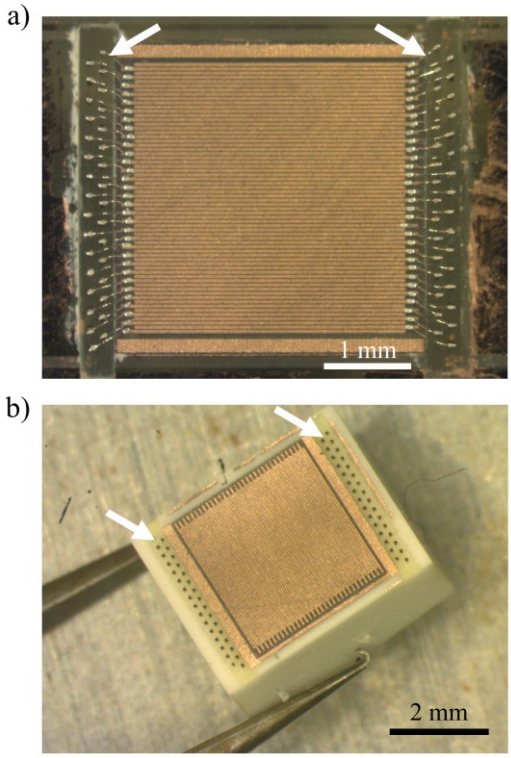

Figure 4-5 Photo of a) the backside of the array with the wire bonds between the array and strips of flexible circuit board completed and b) the array and backing layer stack showing the front face of the array with the strips of flexible circuit board accessible. The strips of flex are highlighted with arrows.

impedance [131]. The acoustic stack, consisting of the crossed electrode array and backing layer, was diced to its final size. The stack was then flipped over revealing a series of wire bonding pads that now face forward along the two sides of the array perpendicular to the front side electrodes. Each bonding pad in the flex strip is connected to a back-side element. On the other two sides of the front face, the elements are also ready to be wire bonded directly to the element electrode pattern resulting in wire-bonding access to 32 elements per side for all four sides. The array stack is shown in Figure 4-5 b). Four full flex circuits can then be placed along the four sides of the array connected to a plastic mount

with the ends flush with the array face. The front side elements were then wire bonded to the thickness dimension of the flex (64 bonds) and the back-side connections were completed by bonding the pads from the strip to the thickness dimension of the other two flex circuits (64 bonds). The whole bonding process requires 192 bonds for 128 electrodes (Figure 4-2 e)). The front face of the array with the flex mounted and electrical connections completed is shown in Figure 4-6. The final size of the packaged endoscope is less than 6 mm x 5 mm.

The final step of the array fabrication was the creation of the quarter wavelength matching layer (Figure 4-2 f)). The matching layer was vacuum deposited using a conformal coating system with Parylene C (SCS Coatings, Indianapolis, IN). The acoustic impedance for the ideal, single quarter wavelength is given by [12],

$$Z_{1/4} = (Z_p {Z_m}^2)^{1/3}, \tag{4-1}$$

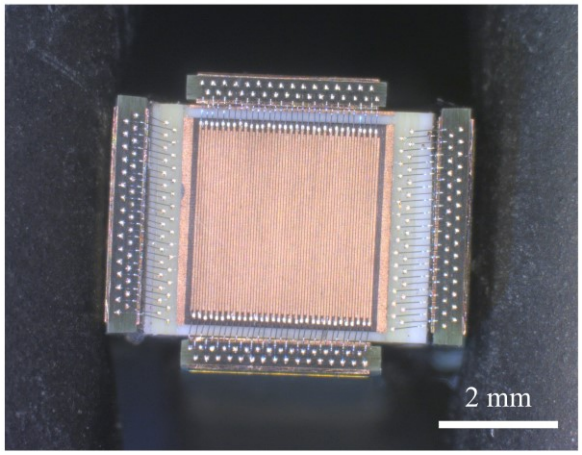

Figure 4-6 Picture of front face of the array with the four flexible circuit boards mounted flush with the array and the 128 wire bonds completed.

where Z_p is the acoustic impedance of the piezoelectric substrate and Z_m is the acoustic impedance of the transmission medium (i.e. water/tissue in medical ultrasound). Given that the approximate acoustic impedance of the composite is 16 MRayl, the ideal matching impedance between the composite and water is 3.3 MRayl. Thus, the acoustic impedance of Parylene (2.5 MRayl) is a close match to the optimal quarter wavelength matching layer and was chosen for this design.

At the system end of the flex PCBs, connectors were mounted such that a commercial 128 wire coaxial cable could be plugged in (Comfort Plus, TE connectivity, Schaffhausen, Switzerland) and connected with the previously developed high frequency beamformer. A photograph of the completed 30 MHz, forward-looking, crossed electrode array with the endoscopic packaging is shown in Figure 4-7.

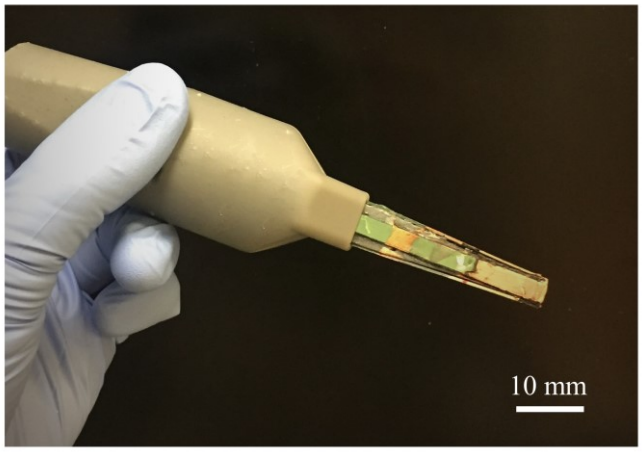

Figure 4-7 Photo of the completed array packaged into the endoscopic for factor.

4.5 Characterization

The electrical impedance of individual array elements was measured using an RF impedance analyzer (4294A, Agilent Technologies Inc., Santa Clara, CA). There is a bias function on the impedance analyzer that was used to provide a 40 V bias to the element under test. Figure 4-8 shows impedance magnitude and phase curves for the 64 signal elements measured in water. The measurements show 94% of the elements have largely uniform impedance, however, two pairs of elements are outliers. These element pairs are next to each other on the array and have a low impedance path between the elements (a few ohms). Likely this was caused by a small piece of the electrode that was not removed in the laser

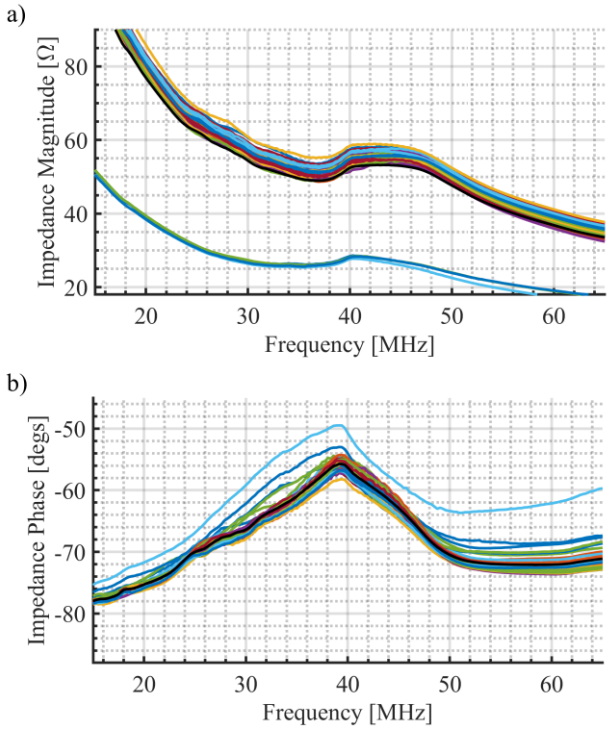

Figure 4-8 Water loaded impedance measurements from all array elements showing a) impedance magnitude and b) impedance phase.

etch or a piece of leftover debris. Likely, this could be eliminated in future builds with some combination of adjusting the laser etch power or number of etch passes and ultrasonic cleaning after etching. The electrical impedance magnitude on resonance has a measured mean of 49 **Ω** with a standard deviation of 7.3 **Ω** and a mean phase angle of -55.5° with a standard deviation of 1.5°. Despite having a small area, the impedance of the element is low and well-matched to the cable (50 **Ω**) because of the high dielectric constant inherent to electrostrictive ceramic.

Pulse echo experiments were completed by biasing the entire back-side of the array, pulsing a single element on the front side of the array, and measuring the returned echo from a wire phantom in a water bath. Figure 4-9 shows a

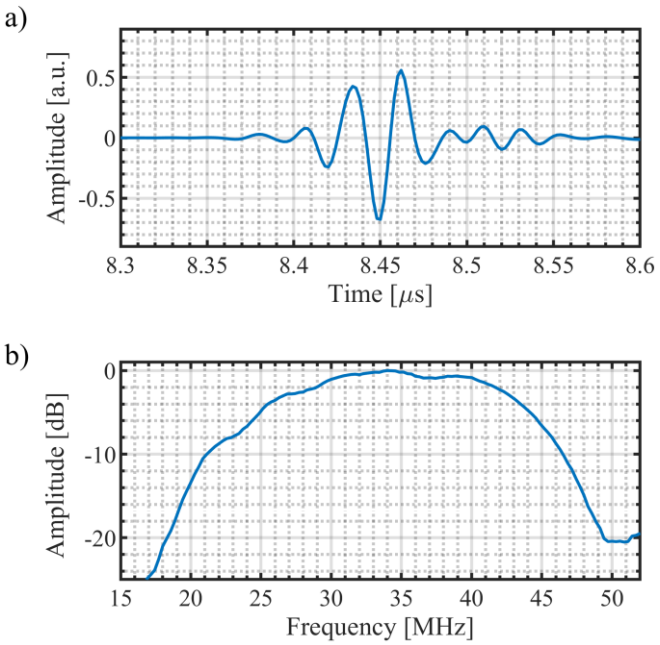

Figure 4-9 Pulse echo response off a wire target in a water bath, a) the received pulse and b) the magnitude of the pulse spectrum.

representative pulse with a measured -6 dB bandwidth of 60% and a center frequency of 34 MHz.

The electrical crosstalk was measured by biasing the back-side of the array, exciting a single channel, then recording the peak to peak signal amplitude on neighbouring elements. The average measured crosstalk on the nearest neighbouring element was -37 dB. The next-to-nearest elements had a relative signal of -29 dB. All elements beyond the first two nearest neighbours had a crosstalk level below -30 dB. The crosstalk is higher on the next-to-nearest elements because the even elements are connected to one flexible circuit board and the odd are on the second board, therefore, the biggest contribution to the element crosstalk is from electrical crosstalk in the flex PCB.

Finally, switching speed tests were completed to determine how quickly the electrostrictive ceramic could change polarity. This measurement is of importance for imaging approaches that require a different pulse polarity on transmit and receive. The polarization must be set for the duration of the transmit pulses and then switch quickly and be polarized in the opposite direction in time for the receive data collection window. In this case, for 30 MHz operation, the imaging window begins approximately 5 µs after the transmit pulse. One-way experiments were completed by measuring the pressure pulse with a needle hydrophone (Precision Acoustics Ltd., Dorset, UK) in a water bath and reducing the time between changing the bias and pulsing the element. Figure 4-10 shows the results

from three conditions. Figure 4-10 a) and b) compare the pulse produced when changing the bias from positive to negative and pulsing 2.9 µs later and changing the bias from negative to positive and pulsing 2.9 µs after the transition. The resulting pressure pulses have opposite polarity and approximately equal amplitude. In Figure 4-10 c) the delay between the change of bias polarity and transmit pulse is extended to 350 ms. The measured pulse is of equal amplitude to the case where only 2.9 µs of polarization time was allowed. When the delay between bias switching and the transmit pulse is reduced below 2.9 µs, the pressure output reduces severely. Chen and Gurguraja [169] reported the polarization time for PMN-PT to be 30 µs using a 2 kV/cm bias, however, it is expected that the time required for polarization to be related to both the

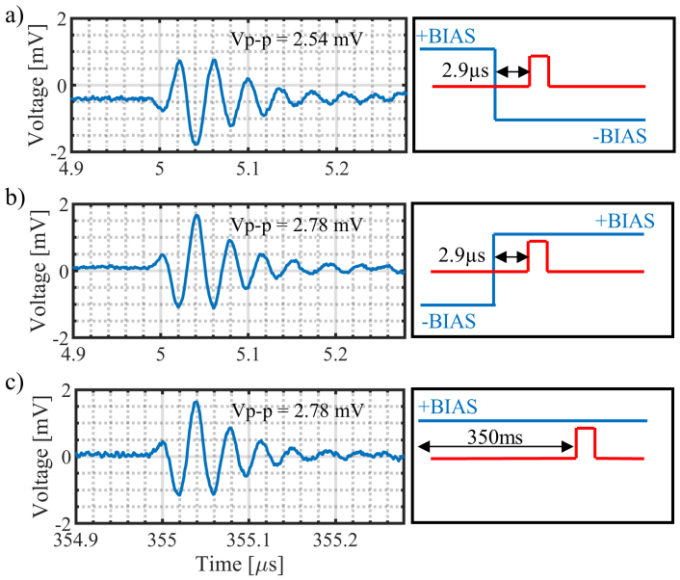

Figure 4-10 Hydrophone measurements under different bias switching delay conditions, a) the bias switched from positive to negative 2.9 µs before the transmit pulse, b) the bias switched from negative to positive 2.9 µs before the transmit pulse and c) the bias switched from negative to positive 350 ms before the transmit pulse.

transducer thickness and the bias strength. Two-way pulse echo experiments were also completed to test the receive polarization switching as well as the transmit. Again, the time delay between switching the bias and pulsing the element was reduced in steps. When the time delay was decreased to 4 µs following the transition, the peak-to-peak voltage of the received pulse was still 95% of the signal from a fully saturated DC bias.

4.6 Imaging Results

To demonstrate the imaging performance of the array, a simple three-dimensional wire phantom in a water bath was imaged. The imaging technique that was previously developed (Chapter 3) is referred to as Simultaneous Azimuth and Fresnel Elevation (SAFE) compounding [5]. In this technique, an electrically reconfigurable lens is created in the elevation dimension. This lens is designed to mimic a Fresnel lens or zone plate. To improve the focus quality in elevation, multiple Fresnel lens approximations can be used to compound the imaging data and improve the resulting focus. When an ultrafast compounding technique such as plane wave or diverging wave imaging is employed in the azimuth direction using the signal channels, both planes can be compounded simultaneously to improve the beam profile and image quality.

Two-way beamformed radiation patterns were collected by moving a glass point target in the water bath and repeating the data collection for the same

elevational slice. The experimental radiation patterns were compared to simulated patterns that were modelled in a similar manner. Crossed electrode array radiation patterns were simulated using Field II [55], [57]. The radiation patterns were generated for a 30 MHz, 64 x 64 crossed electrode array to demonstrate the 3D imaging performance of the endoscope. The control over polarization was replicated by applying apodization values of either +1 or -1. The crossed electrode array architecture was modelled by applying the same delay profiles across elevational elements and the same apodization profiles across azimuthal elements. The radiation pattern profiles are shown in Figure 4-11. The

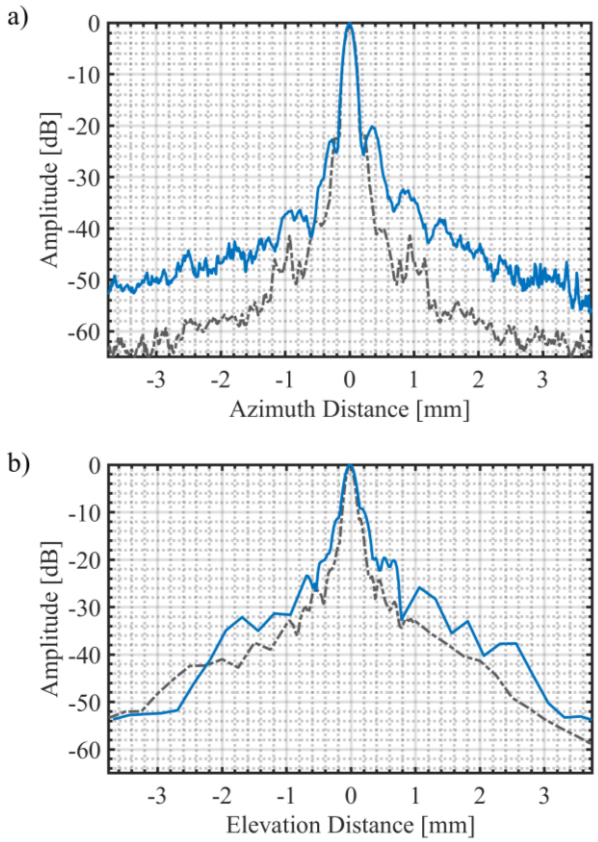

Figure 4-11 A comparison of simulated (dashed grey) and experimental (solid blue) two-way beamformed radiation patterns in the a) azimuth and b) elevation direction for the 30 MHz, endoscopic crossed electrode array.

simulated azimuthal and elevational -6 dB beamwidths were both 190 µm. The experimental beamwidths compared well at 200 µm and 238 µm in the azimuth and elevation respectively. The secondary lobes are comparable between the simulations and experiment, however, the small discrepancy can likely be explained by the imperfection of the glass point target, small errors in the beamforming delays and nearing the noise floor of the system.

The 3D image is built up elevation slice by elevation slice by simply reconfiguring the compounded Fresnel lens focus. The experimental setup includes a custom 64 channel beamforming system with a 3D imaging module that provides the 64 reconfigurable, fast switching biasing channels. The imaging results from a wire phantom of two crossed, depth offset wires in a water bath are shown in Figure 4-12 using two views. The perpendicular wires were offset in depth by 1 mm and were 20 µm in diameter. Figure 4-12 a) shows the centre 2D slice with a dynamic range of 50 dB. A 3D rendering of the two crossed wire is shown in Figure 4-12 b) where the values below 40 dB have been set to be transparent.

4.7 Discussion

This study has presented the fabrication and characterization of a 30 MHz, 64 x 64 element crossed electrode relaxor array miniaturized into an endoscopic

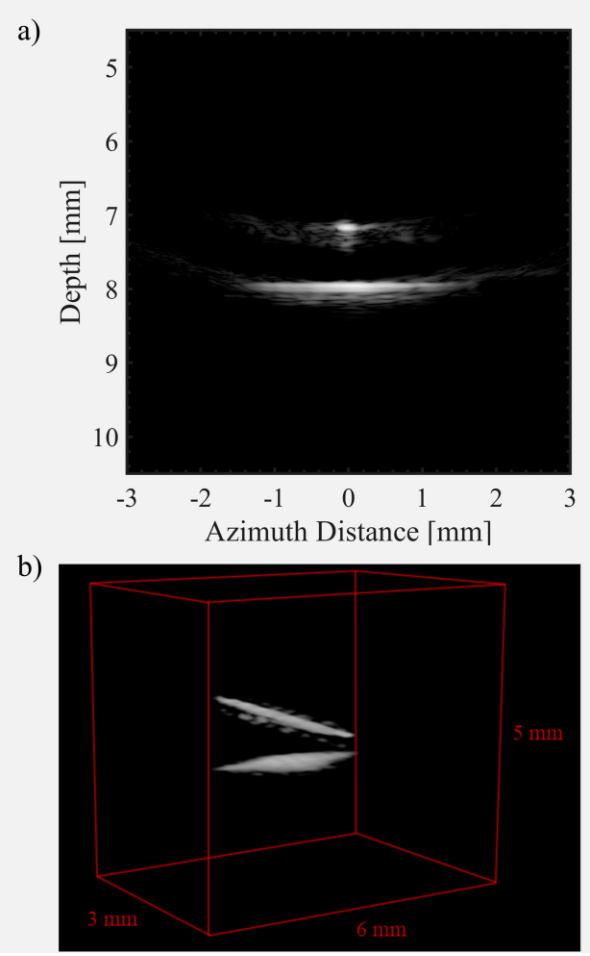

Figure 4-12 Imaging results from two crossed wires in a water bath from a) an azimuth-depth slice in the centre of the volume image (50 dB dynamic range) and b) a 3D rendering of the volume image.

form factor. A significant challenge to miniaturizing a crossed electrode array is electrically connecting the back-side elements without adding bulk to the packaging. A process has been developed that uses a thinly diced strip of flexible circuit board to bring the back-side connections to a front-facing bond surface. The cross-sections of the thick circuit traces are well suited to act as wire bonding pads. When this process is combined with a previously described packaging technique that mounts the end of the flexible interconnect boards flush

with the array face, the overall size of the electrical connections, including the connections to the back-side is minimized to less than 60% of the face of the forward-looking array. Some tolerance was given when cutting out the array and backing stack to its final size. The packaged size could be reduced by at least 0.5 mm in each direction.

Some interesting features of the fabrication process were made possible with a laser dicing system. Previously, mechanically dicing 1-3 composites for operation around and above 30 MHz has yielded poor results. The smallest blade size for a dicing saw is 10 µm which automatically limits composite design in the >30 MHz range. The narrow pillars that are required to ensure that spurious lateral modes are pushed outside of the transducer's bandwidth are susceptible to breaking. In some cases, the breakage is obvious, and the pillars completely break off the sample. More often, there is microcracking that extends, from the surface, 5-10 µm into the pillar. When a pillar is less than 25 µm this type of microcracking can significantly degrade performance. A diode pumped, solid state laser dicing system (Oxford A-Series Laser System, Oxford Lasers Ltd, Oxford, United Kingdom) was used to machine the 1-3 composite that acted as the substrate of this array. The laser dicing approach can make high aspect ratio cuts with a very small spot size with the expectation of no mechanical damage and little heat damage. The composite can be laser cut in 4-5 hours so there is not a significant time disadvantage compared to mechanical dicing. Previous work has

demonstrated processes for laser micromachining high frequency arrays using excimer [170], UV [171], copper vapor [172] and tripled Nd:YAG [173] lasers. This body of work has shown that laser micromachining is a viable method for the fabrication of high frequency ultrasound devices, however, more work is required to determine the optimal laser settings to achieve uniform, high aspect ratio kerfs without damage or depoling. A clear alternative for fabricating high frequency 1-3 composites is deep reactive ion etching (DRIE) [146], [174]. Composite fabrication with DRIE can produce fine features with high aspect ratio pillars without causing damage. Its main disadvantage is the complexity and time required, making it difficult to adopt in research and prototyping. As a test for this work, single element transducers were fabricated using a mechanically diced composite (DAD 3202, Disco Technologies, Tokyo, Japan) and a laser diced composite, both using 30 MHz composite designs. The electromechanically coupling coefficient was measured to be 0.38 and 0.58 for the mechanically diced and laser diced respectively. Both transducers were biased with 40 V (7 kV/cm). Although limited characterization information exists for this electrostrictive ceramic, the available datasheets give maximum values of k_t and k_{33} of 0.52 and 0.64. This test gave confidence that the laser diced composite suffered from very little mechanical damage. At the very least, it does not exhibit the same damage of the mechanically diced composite. Still, more work characterizing laser diced high frequency composites will follow using different piezoelectric materials.

The laser system also provides advantages to the process flow and reliability of fabrication. The laser cut paths are defined in software and are not limited to the straight full sample width cuts of the dicing saw. This allowed us to define the composite cut paths such that the area under the wire bonding pads is solid ceramic. The even, solid surface provides a large increase in the yield and reliability of the wire bonds. With composites of this scale, the composite pillars are much smaller that the foot of the wedge wire bond. When the transitions between ceramic and epoxy are even slightly uneven, the integrity of the bond is likely to be compromised. The laser system also replaced the photolithography step. Again, the photolithography yields can be reduced on a composite surface. With the laser system, the electrode patterns are defined in CAD software without the need for physical masks to be made. Laser etching the element electrode pattern has been precise, repeatable and, importantly, allows for fast iterations in the pattern shape and etch depth.

The results from the imaging experiments show excellent agreement with designed theoretical predictions. The electrical impedance measurements show a good on-resonance electrical match to the cabling and consistent impedance across the array. The signal elements of the crossed electrode array produced pulses with a two-way bandwidth of 60%. The pulse centre frequency of 34 MHz was slightly higher than designed and can be attributed to a slightly lower speed of sound in the composite substrate than predicted. The crosstalk measurements

alleviated any concern about unwanted signal coupling in both the azimuthal and elevational direction because of the crossed electrode array design.

The testing of the electrostrictive array has shown that the polarization direction within the ceramic can reverse direction in less than 3 µs. However, it has become clear that the polarization can turn on almost immediately because the transducer can produce a pulse when the bias switches with a sharp transition. These erroneous pulses can create artifacts in the image just above or below a true scatterer. To reduce these image artifacts the switching of the biases is filtered using the bias tee passives. The RC time constant was chosen to be 1 µs. The impedance of the capacitor is much lower than the resistor at the operating frequency, so the pair still act as a bias tee. This filter reduced the bias switching pulses compared with previous arrays, however, the time constant could be increased further and eliminate the unwanted pulsing.

3D capable ultrasound arrays have been difficult to fabricate, especially under the requirement of an endoscopic form factor. The traditional 2D array grid introduces challenges related to the huge number of elements. This challenge presents itself in fabricating the array as well as in providing the necessary beamforming electronics. A crossed electrode array design alleviates both aspects of the problem. First, only requiring $2N$ elements significantly reduces the number of electrical connections to fit into endoscopic packaging. Second, the beamforming system does not require more signal beamforming channels than a

similar 2D imaging system for 1D arrays. In this case, the 64 channels of fast switching biases were the only addition to our custom 64 channel beamformer allowing the transition from 2D to 3D imaging. These choices make it possible to build a relatively low-cost 3D ultrasound system.

As a final characterization of the endoscopic array, volume images were generated of a crossed wire phantom. These preliminary wire phantom experiments demonstrate the performance of the 2D array using our previously described 3D imaging method. Future work regarding the crossed electrode array endoscope involves demonstrating new 3D imaging techniques in detail and exploring the performance in clinically relevant tissue for the endoscopic imaging application (e.g. brain imaging). This study has demonstrated the ability to fabricate a high frequency crossed electrode array in a miniaturized form factor. The 3D capable device could be used in many new applications requiring high resolution, endoscopic imaging.

CHAPTER 5

A NEW 3D IMAGING TECHNIQUE INTEGRATING ULTRAFAST COMPOUNDING, HADAMARD ENCODING, AND RECONFIGURABLE FRESNEL LENSING

5.1 Preamble

The content of this chapter will be submitted for peer review to IEEE Transactions on Ultrasonics, Ferroelectrics, and Frequency Control under the same title. Any introductory material previously covered in the Background Chapter has been removed or reduced for conciseness. Modifications to the journal article manuscript have been made to unify this document both in terms of nomenclature and formatting as well as providing a clearer story of the relevance in the evolution of the project. The main goal of this study was to demonstrate the performance of a new bias-controlled imaging technique that used a Fresnel type lens on transmit combined with Hadamard receive coding to create the elevation focus on a crossed electrode array.

5.2 Introduction

Over the last few decades, there has been significant engineering effort towards improving 3D ultrasound imaging, both in the design of the imaging transducer and in the image building methods. The engineering work has been driven by the clinical demands for practical, fast, high-quality volumetric imaging as the niches for 3D ultrasound have become more and more clear. 3D ultrasound provides flexibility in visualization, increased accuracy in volume measurements and real-time guidance of interventional procedures across many medical specialties (e.g. obstetrics, cardiology, vascular surgery, interventional radiology) [10]. These applications of 3D ultrasound highlight the advantage of an endoscopic, 3D capable probe. A 3D imaging endoscope can provide surgical guidance with high resolution images for applications where a large probe imaging from outside the body would not be adequate (i.e. imaging fine structures that are not superficial or are shadowed by strong reflectors).

Ultrasound systems based on 2D matrix arrays present several technical challenges including the number of elements/beamforming channels, electrical matching issues resulting from the high impedance of the small elements, and image acquisition time for a 3D volume. However, a 2D array of some kind is necessary to avoid the complexities of mechanically scanning a 1D array. A sparse element 2D array is one approach that limits the number of electrical connections and beamforming channels. The work developing sparse arrays has

focused on optimizing the sparse element pattern that balances main lobe width, as well as secondary lobe and grating lobe levels with element count and SNR [70], [175]–[177].

A second approach to reducing the channel count of a 2D array is the crossed electrode array architecture (i.e. row-column addressed array, Top-Orthogonal-to-Bottom-Electrode (TOBE) array). Crossed electrode arrays address some of the challenges associated with 2D arrays, mainly by reducing the number of elements to $2N$ from N^2, compared to the equivalent 1D array. However, creating a two-way focused 3D image in real-time is difficult with these arrays because the azimuth and elevation dimensions cannot be beamformed at the same time. This typically leads to using a synthetic aperture approach which often suffers from low signal to noise [76], [78], [126]. The choice of array architecture is important for reducing cost and easing fabrication requirements; however, the performance of ultrasound arrays also depends on the imaging scheme used to build images. This is especially true for these unconventional array designs, including both sparse 2D arrays and crossed electrode arrays.

Crossed electrode array imaging schemes have been discussed in Chapter 2 and Chapter 3. The main options include row-column addressing [89]–[91], synthetic aperture imaging [80], [84], [85], Fast Orthogonal Row-Column Electronics Scanning (FORCES) [53], [54], [96] and our first technique of SAFE compounding [5].

This work describes a new 3D imaging technique that performs ultrafast imaging with the elements along the azimuth dimension while combining a bias-controllable transmit lens and receive Hadamard coding using the elevational elements. When the received data is decoded, we effectively gain synthetic receive aperture data for the elevation elements even though there is effectively only one channel in that dimension. Each slice is collected, decoded and beamformed and the 3D volume is built up quickly.

The imaging technique is demonstrated on a 30 MHz, 128-element crossed electrode array in a miniature, endoscopic form factor (described in Chapter 4). The performance of the volume imaging technique is demonstrated with two-way radiation patterns in both planes, wire phantom images and ex-vivo rat brain images.

5.3 Imaging Methods

The new 3D imaging approach that has been developed uses the flexibility of bias sensitive (i.e. pulse amplitude and polarity depend on a DC bias) substrates to create a high-quality elevation focus on a crossed electrode array. The principle behind this technique is to perform conventional compound imaging (e.g. diverging wave imaging) with an azimuth set of electrodes while implementing a bias controllable elevation lens with an elevation set of electrodes. Figure 5-1 shows the crossed electrode array architecture with the signal and bias

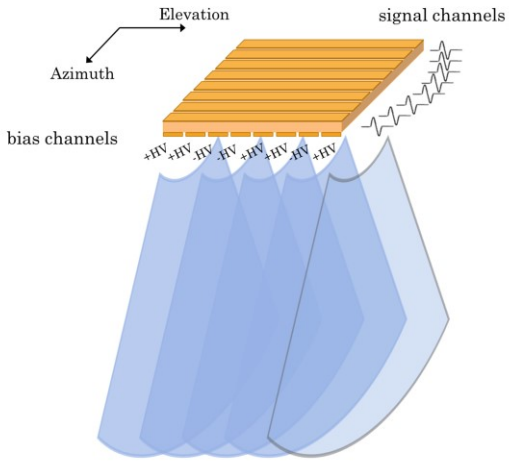

Figure 5-1 Diagram showing the signal channels along the azimuth direction, bias channels along the elevation direction and slice-by-slice acquisition of a volume image.

channels assigned to the top and bottom electrodes respectively. On transmit, the biases are chosen to mimic a Fresnel lens. Then, on receive, Hadamard coding is implemented along the elevation dimension. After N pulses and N orthogonal receive patterns the data can be decoded for the current image slice.

Hadamard based coding has been used in various forms in ultrasound imaging, first largely to improve SNR in an alternative to traditional synthetic aperture imaging [49]–[52] and, more recently, to provide a transmit elevation focus on crossed electrode arrays [53], [54]. A Hadamard matrix is made up of entries equal to +1 or -1 with the property that each row is mutually orthogonal. When the elements across an aperture, in this case, the receive elevation, are Hadamard encoded (given either a positive or negative polarity) we can perform a simple matrix calculation on the set of received signals to decode and retrieve the equivalent of the RF data from each element across the array. The decoding

step uses the properties of orthogonal matrices. The transpose of an orthogonal matrix multiplied by the matrix is equal to an identity matrix with a gain term, n.

$$\boldsymbol{H^T H = nI} \tag{5-1}$$

The Hadamard matrix is given by $\boldsymbol{H}$. A vector of raw RF data lines as a function of time, t, received for each coded receive bias pattern (R_{rxn}) for each azimuthal element is given by $\boldsymbol{R}$. The field transfer matrix, $\boldsymbol{\Phi}$, is the transfer function from the transmit lens aperture, through the field and back to each receive elevation element. The decoded RF data at time, t, for each element is given by $\boldsymbol{R_D}$.

$$\boldsymbol{H^T R}(t) = \boldsymbol{H^T H \Phi}(\boldsymbol{t}) = \boldsymbol{R_D}(t)$$

$$\boldsymbol{R}(t) = \begin{bmatrix} R_{rx1} \\ R_{rx2} \\ \vdots \\ R_{rxN} \end{bmatrix}_t \quad , \quad \boldsymbol{R_D}(t) = \begin{bmatrix} R_{ele1} \\ R_{ele2} \\ \vdots \\ R_{eleN} \end{bmatrix}_t \tag{5-2}$$

If the number of rows in the Hadamard matrix, N, is equal to the number of elevational bias elements, the decoding step results in the received signals from each elevational element, as if only one elevational element was active at a time on receive. With this data, we form a synthetic receive aperture and can dynamically receive beamform at all image depths, with the advantage of having 100% of the aperture active during each transmit/receive event. On transmit, a focus is created with the Fresnel lens so, in sum, a two-way focus is the result. For 3D imaging, the process repeated for each elevational slice in the volume

image. Figure 5-2 shows how the process repeats in elevation to build the volume. When imaging each slice, a new Fresnel mimicking lens is chosen and, while that bias pattern is kept constant, the receive bias patterns switch through the Hadamard codes in N transmit/receive events. Next, the transmit Fresnel pattern is changed to focus to the next 2D slice and the receive Hadamard patterns repeat. During each set of N transmit/receive events ultrafast compound imaging can be completed in the azimuth direction simultaneously similar to SAFE compounding. Using 64 elevational elements (corresponding to 64 orthogonal

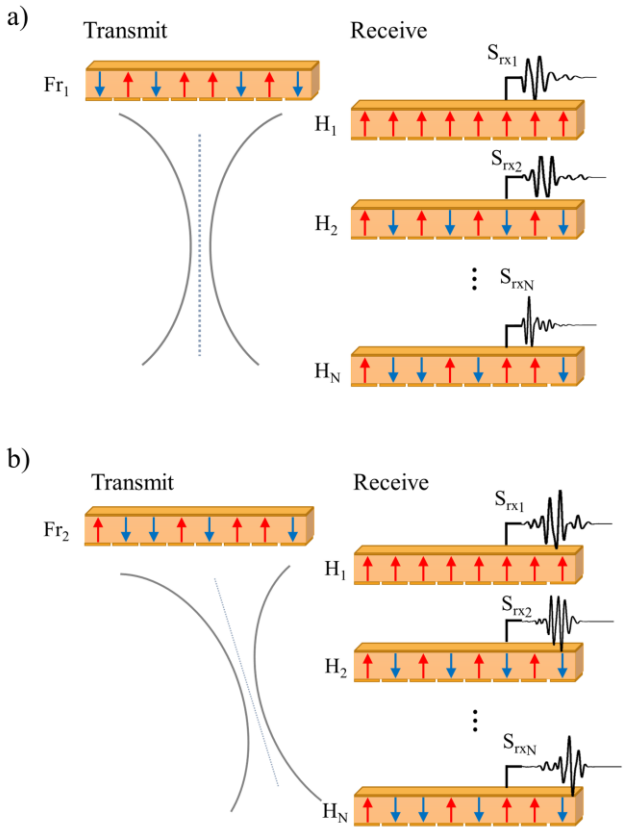

Figure 5-2 Diagram showing the imaging technique in the elevation dimension, an elevation slice is selected with a bias controlled Fresnel on lens a) on-axis or b) off-axis. For each elevation slice a set of bias coded signals are collected and decoded to build an elevation focused image.

receive codes) and 32 elevation slices, this technique has a potential volumetric frame rate of 19.5 volumes/s. As a comparison, implementing a synthetic receive elevation aperture with a crossed electrode array requires the same number of transmit/receive events, however, only one elevational element is active for each receive. The number of transmits/receive events become costly when building a traditional two-way synthetic elevation aperture. The number of transmit events increase to N^2, rather than N. In an extended acquisition time, it can be difficult to maintain phase for compounding and the system becomes susceptible to motion artifacts. We can limit the acquisition to N pulses per elevational slice while maintaining an approximate two-way focus because we are using an electrically configurable, Fresnel mimicking lens on transmit. In addition, synthetic aperture suffers from low signal to noise ratio, especially when implementing a two-way synthetic aperture. Implementing Hadamard coding on receive gives an N times improvement in decoded signal strength or 36 dB improvement in SNR. In a two-way synthetic elevation aperture approach, the effect is squared and the signal is reduced by 72 dB compared with a fully active aperture.

The imaging technique was simulated using Field II [55], [57]. A 30 MHz 2D array was modelled to demonstrate the 3D imaging performance. The control over polarization was replicated by applying apodization values of either +1 or -1. The crossed electrode array architecture was modelled by applying

diverging wave delay profiles across azimuth elements and the +1 or -1 apodization profiles across azimuthal elements. The receive signals across the elevational elements were summed to reduce the RF data to one signal channel in elevation for each azimuthal element (emulating the crossed electrode configuration). The simulated two-way beamformed radiation patterns in both imaging planes are shown in Figure 5-3. Figure 5-3 a) and b) show radiation patterns for the centre elevation slice and Figure 5-3 c) and d) show the radiation patterns for the farthest elevation slice located 1.3 mm from the centre. There are

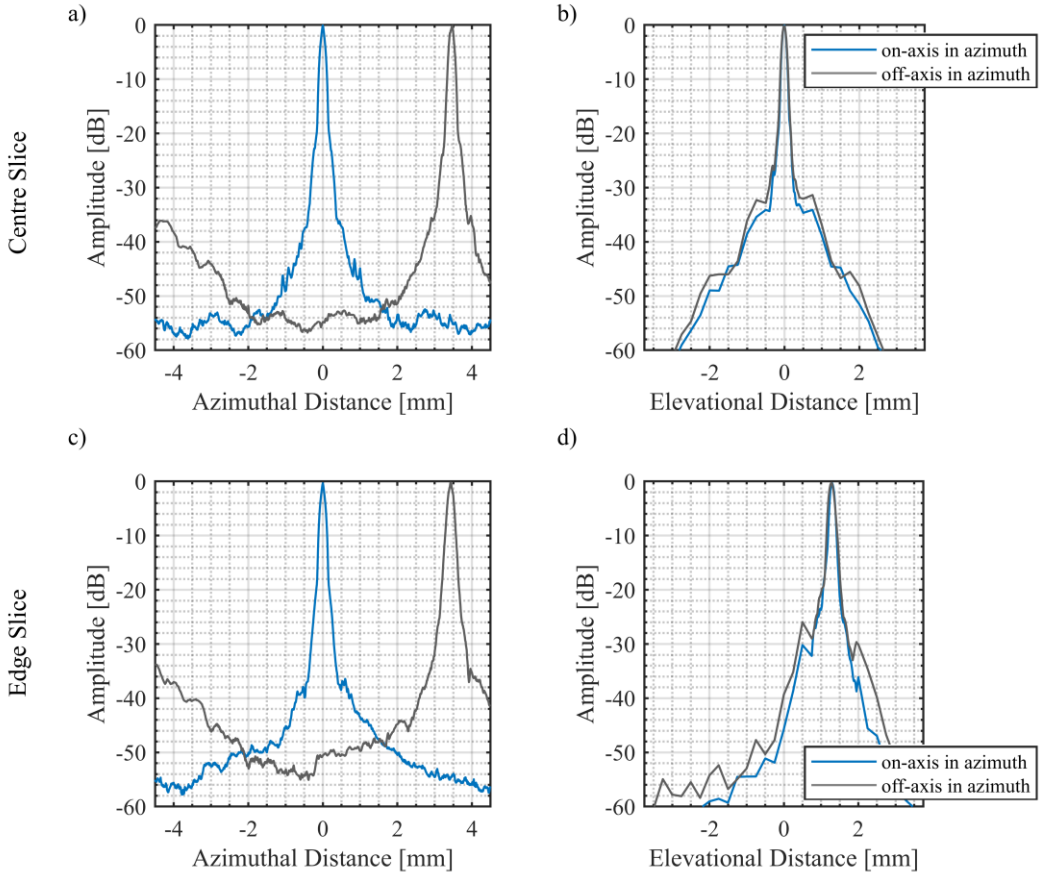

Figure 5-3 Simulated radiation patterns illustrating the performance in the centre elevation slice (a) and b)) and the edge elevation slice 1.3 mm from centre (c) and d)). For each slice the radiation pattern for an on-axis azimuth focus is shown in blue and the steered azimuthal focus is shown in grey.

representative radiation patterns for steering on and off-axis in the azimuthal plane. The point spread functions deteriorate with steering angle. Therefore, the on-axis, center slice result shows the best case focus while the off-axis, edge slice case shows the worst case focus for the imaging technique. The -6 dB beamwidths are summarized for each condition in Table 5-1. A mostly isotropic focus is maintained throughout the field of view.

The electrically reconfigurable lens has inherent limitations. The transmit focus uses the concept of a Fresnel lens or zone plates and approximates the delay profile by phasing the pulses across the aperture with only $\pm\frac{\pi}{2}$ values. This approach directs the energy on-axis quite well. However, the energy at the focus reduces as the focus is steered in elevation. This steering limitation dictates the imaging window in elevation. Figure 5-4 shows the simulated beamformed directivity of the elevation dimension of this imaging technique. The elevation dimension can be steered +/- 1.5 mm (+/- 12 degrees) and be within 6 dB of the peak beamformed amplitude on-axis.

Table 5-1 -6 dB beamwidths for the simulated radiation patterns.

	Azimuth [µm]	Elevation [µm]
centre slice – on-axis	175	150
centre slice – off-axis	190	160
edge slice – on-axis	176	160
edge slice – off-axis	215	210

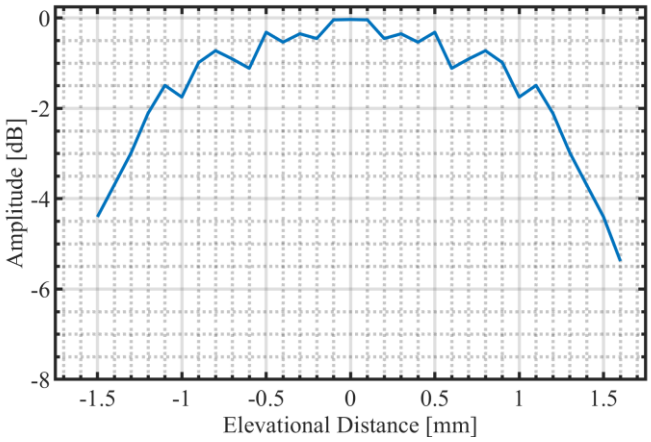

Figure 5-4 Beamformed directivity simulation for the elevation dimension.

An advantage of this approach is that data from neighbouring imaging slices can be reused and beamformed to improve the central slice. The receive data is collected unfocused in elevation so there no pre-beamformed slice selection on receive. Also, the transmit Fresnel focus overlaps its neighbouring elevation slices and there is energy on transmit spanning several elevation slices. Reusing the data on neighbouring slices has a compounding effect on the transmit focus. This strategy is used to mitigate the degradation of the Fresnel transmit focus with the increasing elevation steering angle.

5.4 Array Design

A 30 MHz, 128 element crossed electrode relaxor array was fabricated on an electrostrictive 1-3 composite substrate and packaged into an endoscopic form factor. A full description of the array and characterization data is outlined in Chapter 4.

Previous studies have reported the potential for decoding errors arising from the inability to produce pulses that are perfectly inverted [50], [96] (i.e. maintain the same amplitude and shape). The advantage of choosing electrostrictive ceramic as the active substrate material is its ability to produce perfectly inverted pulses because the polarization within the material changes direction with bias. Therefore, it is an ideal candidate for this type of spatial coding, even on commercial systems where the transmit pulse shape cannot be altered channel to channel. Figure 5-5 demonstrates the pulse inversion on an experimental pulse echo. Both pulses are transmitted with a positive bias voltage, but one echo is received after switching to a negative bias between transmit and receive. The size of these pulses can be easily adjusted by changing the positive and negative bias levels. Also, the polarization direction can be switched very quickly. The material

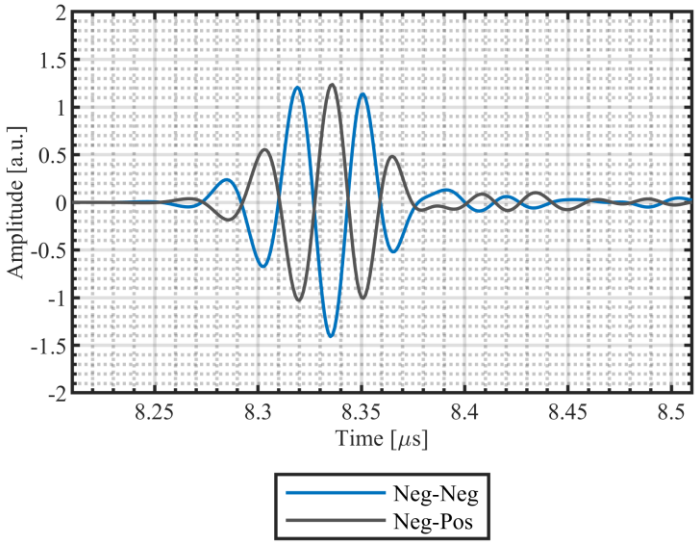

Figure 5-5 Pulse echo data demonstrating the symmetry of the inverted pulse in two states, when the bias is held negative on transmit and receive (blue) and when the bias changes from negative to positive between transmit and receive (grey).

generates over 90% of the full piezoelectric response less than 4 µs after applying or inverting the bias.

5.5 Imaging Experiments

Imaging performance was tested using a custom 64 channel beamforming system with a 3D imaging module that provides the 64 reconfigurable, fast switching biasing channels. 3D images were generated by imaging a phantom using a reconfigurable acoustic Fresnel lens and Hadamard receive coding to focus to a series of elevation slices and build the volume image slice by slice. An ultrafast compounding scheme was implemented in the azimuth direction using diverging wave imaging. In both the elevation and azimuth directions, 64 insonifications were used to compound and reconstruct each 2D slice, corresponding to the 64 elements in the elevational aperture. The system was used in a configuration that collected channel data and the beamforming was completed offline.

First, data was collected from wire phantoms in a water bath. The N receive coded data sets from all N signal channels were stored then decoded and beamformed offline. Figure 5-6 shows the data received by a representative azimuthal element before and after decoding. After decoding, the data becomes uniform in amplitude and has the appropriate delay profile for the reflection from a point target (i.e. the signal is received by the center element first and the edge

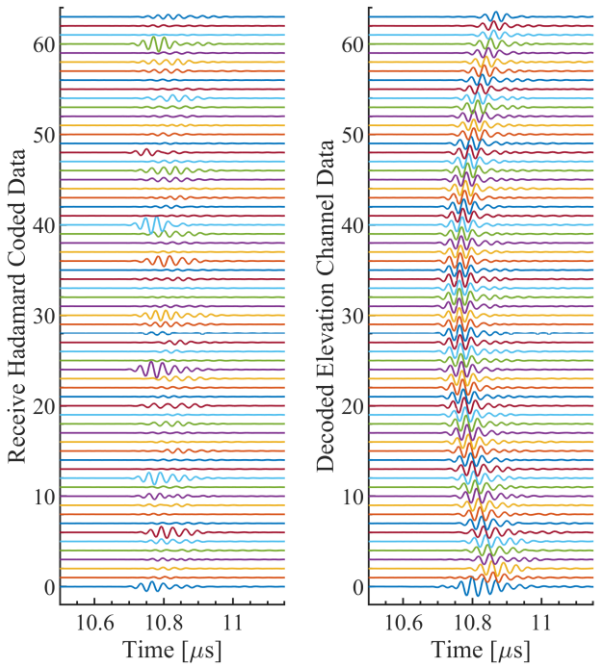

Figure 5-6 A dataset after N insonifications collected from an example signal channel and displayed before decoding (left) and after Hadamard decoding (right).

elements last). Bias channel 1 is the only outlier and may indicate that this element has lost its electrical connection. This elevational channel was removed from the beamformed images.

The phantom experiments were completed with a glass point target (approximately 50 µm in diameter) at the end of a narrow glass fibre that may be visible below the point scatterer. The experiments with the glass point target were completed to compare imaging performance in the volume and compare the focussing in both planes against the simulated predictions. The point spread functions in both planes for the centre elevation slice and an edge slice are shown in Figure 5-7. The lateral resolutions (-6 dB beamwidths) are listed in Table 5-2.

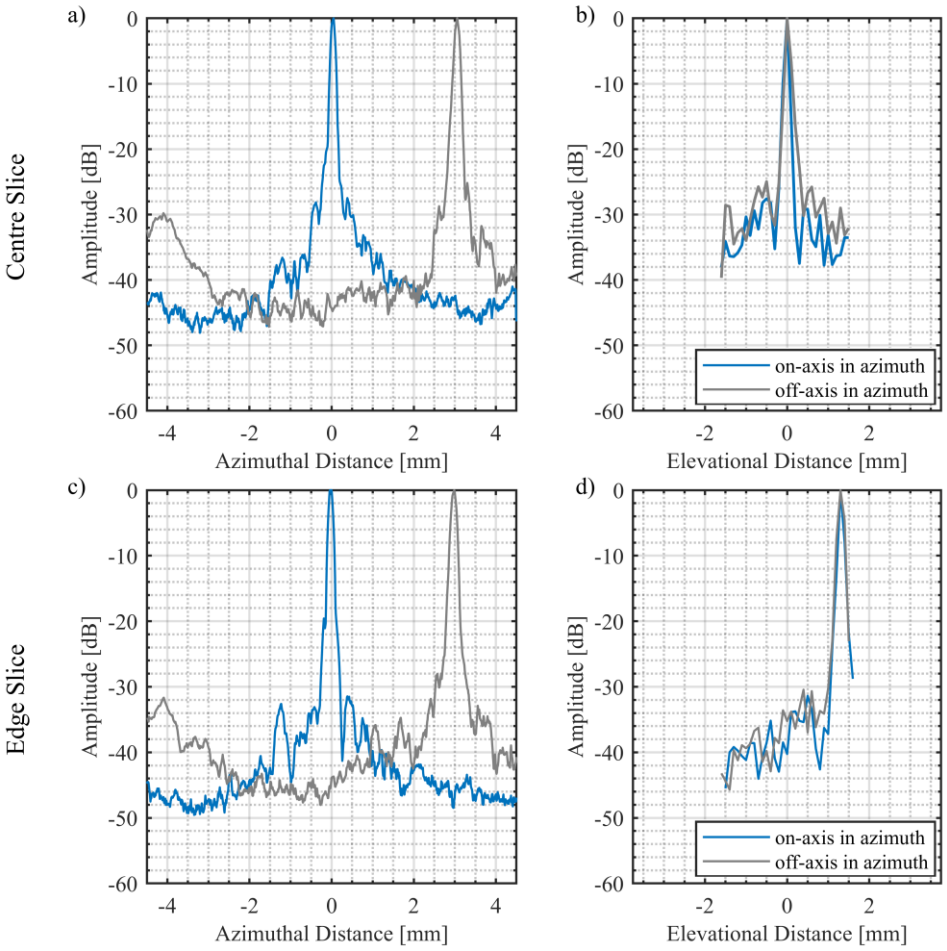

Figure 5-7 Measured radiation patterns illustrating the performance in the centre elevation slice (a) and b)) and the edge elevation slice 1.3 mm from centre (c) and d)). For each slice the radiation pattern for an on-axis azimuth focus is shown in blue and the steered azimuthal focus is shown in grey.

Finally, ex vivo imaging experiments were completed on a rat brain to test the performance of the probe and imaging technique on a clinically relevant tissue. The probe was positioned above the cerebellum and the full 32 elevation slices were collected, decoded and beamformed. Figure 5-8 a) and b) shows example slices of a volume in the azimuth and elevation planes respectively. For this acquisition, the azimuth is aligned with the coronal plane. Figure 5-8 c)

Table 5-2 -6 dB beamwidths for the measured radiation patterns.

	Azimuth [µm]	Elevation [µm]
centre slice – on-axis	155	162
centre slice – off-axis	178	161
edge slice – on-axis	158	161
edge slice – off-axis	180	175

shows biplane images from another volume acquisition where the probe was rotated so the azimuth is showing the sagittal plane. In each biplane image, the position of the slice in both azimuth and elevation is shifted to show that the detail in the planes matches throughout the volume.

5.6 Discussion

For crossed electrode arrays, accessing channel data in the elevation dimension is key for providing a high-quality elevation focus and an isotropic point spread function throughout the volume. An electrostrictive substrate can be used to provide an electrically configurable elevation focus in a novel way. Combining a Fresnel lens on transmit with receive Hadamard coding allows a two-way focus to be created in the elevation dimension of these 2D arrays. In addition, the elevation plane can be dynamically receive beamformed without the sacrifice of SNR inherent to conventional synthetic aperture approaches.

The principle behind this imaging technique relies on the assumption that what is happening in one plane does not significantly affect the other plane. The

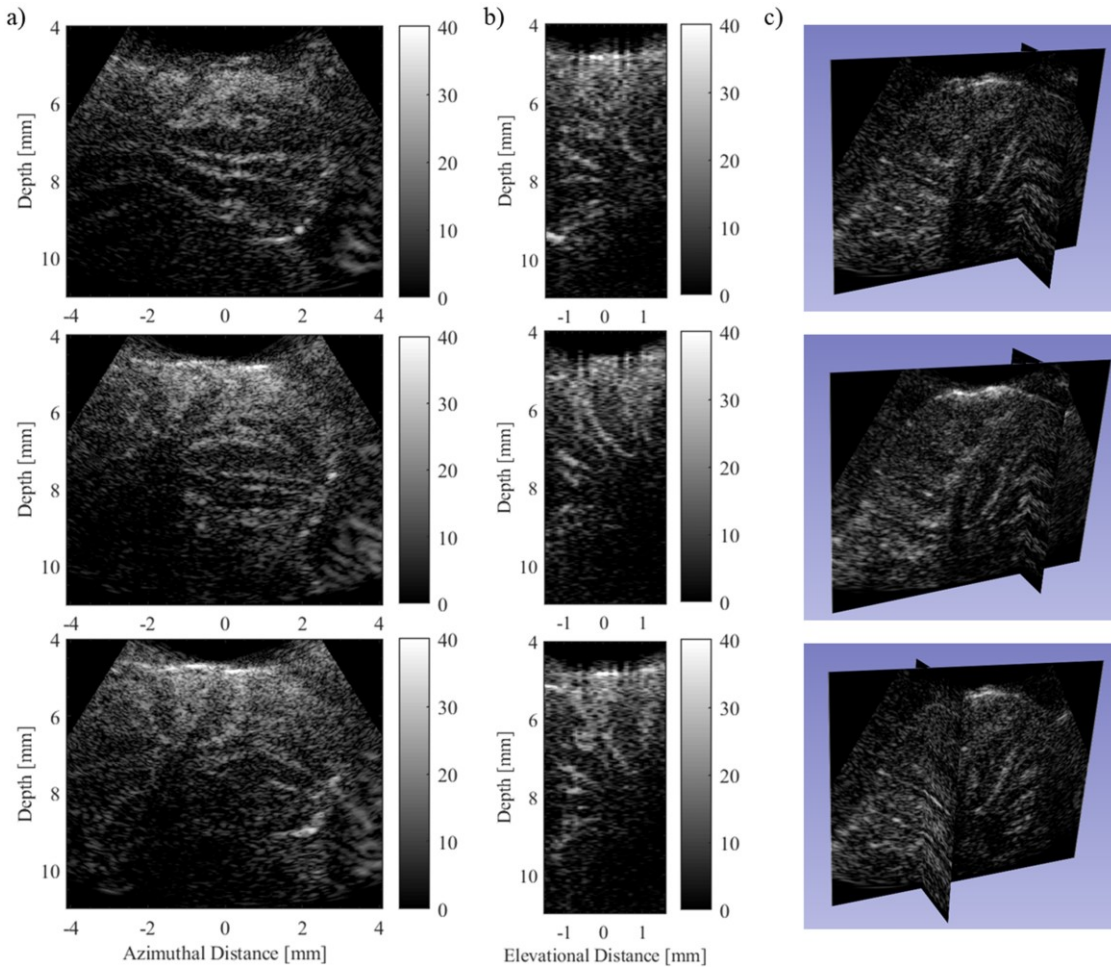

Figure 5-8 Volume images of a rat cerebellum, a) and b) show example slices in the azimuth and elevation planes and c) shows biplane images of a different volume acquisition.

simulations show that this is largely true. However, it only holds true if the transmit delays are compensated for before elevational Hadamard decoding. This is a complication that is added when implementing Hadamard coding on receive. In most cases, especially on a 1D array, the advantage of Hadamard coding is on the transmit side and all elements are connected to and used to dynamic receive beamform. When Hadamard coding on receive, the changing transmit delay profiles will cause large errors in the decoding. Fortunately, there is a straight

forward solution. The order of the decoding and azimuthal beamforming step does not matter. The equation for the beamformed set of 2D slices is given by (5-3),

$$B_{az}(\theta, r, n) = \sum_{k=1}^{N} h_{k,n} \sum_{m=1}^{N} r_{k,m}(t - \tau(\theta, r, n, m)) \tag{5-3}$$

where m and n are indexes for azimuthal and elevation elements respectively, k indexes the rows in the Hadamard matrix and τ represents the round-trip beamforming delays. The order of the summations does not matter; therefore, the azimuthal beamforming can be completed before decoding. Then, before demodulation and envelope detection, the images can be decoded and elevation beamformed. When the images from the N elevational elements are phase-aligned and added, the compounding in both planes is completed. This streamlined beamforming approach has larger advantages to system implementation. If the received data could be beamformed and decoded in hardware, the data transfer requirements would be reduced and the beamformed frame rate would increase.

The imaging technique presented here does not have an equal azimuthal and elevational field of view. The diverging wave imaging allows a large sector ($\pm$ 35°) to be scanned in the azimuthal plane, limited by the wavelength element pitch. However, in the elevation plane, the field of view is approximately $\pm$1.5 mm ($\pm$ 12°). The field of view was chosen based on the beamformed directivity of the transmit lens using a Fresnel type bias pattern, however, the

brain images did not appear dim in the far slices so the elevation field of view could be expanded.

Imaging experiments were completed on ex vivo rat brains, specifically the cerebellum. The transitions between folded layers of cerebellar tissue are present on the ultrasound images (i.e. cerebellar fissures, white matter layers, granular and molecular cell layers) and the shapes change as the slice is moved through the volume. This was the first set of tissue imaging experiments completed with this 3D imaging system. The lab was limited both in access to the brains and time to complete the experiments due to restrictions associated with the COVID-19 pandemic so the images presented here are the results from a single experiment. The images demonstrate the potential of this 3D imaging technique. Accessing the channel data across the elevation dimension by Hadamard encoding/decoding is an important step in achieving an isotropic beamformed focus. The increased hardware requirements over a conventional 1D array system are only a simple set of biasing channels in the elevation dimension, and the resolution in the images as high in the elevation plane as the azimuth. This imaging technique, along with the array architecture, address 3D ultrasound challenges associated with channel count, volumetric frame rate, signal-to-noise, and the creation of a high-quality elevation focus.

CHAPTER 6

CONCLUSION

This dissertation presented a high frequency, bias-sensitive, forward-looking crossed electrode array packaged into an endoscopic form factor along with novel imaging approaches for 3D imaging using crossed electrode arrays generally. The supporting electronics are relatively simple when compared with other 3D ultrasound systems. The crossed electrode array required the same number of RF channels as an analogous 1D array. A module was added to a 64 channel beamformer that supplies and dynamically controls the 64 biasing channels. The result is a low channel count 3D imaging system. The crossed electrode array design has enabled the packaged tip of the array to be 5 mm x 6 mm, a size appropriate for endoscopic tools in many minimally invasive, burr hole neurosurgeries. The 30 MHz device provides appropriate penetration depth (up to 20 mm) and resolution (~50-200 µm) for small animal imaging, brain and spine surgeries and other minimally invasive surgeries.

6.1 Simultaneous Azimuth and Fresnel Elevation (SAFE) Compounding: A Fast 3D Imaging Technique for Crossed Electrode Arrays (Study 1 – Chapter 3)

Study 1 introduced the new, fast and simple 3D imaging approach termed Simultaneous Azimuth and Fresnel Elevation (SAFE) compounding. The principle behind this technique is to perform conventional plane-wave compounding with a back set of electrodes while implementing a reconfigurable Fresnel elevation lens with an orthogonal set of front electrodes. While a Fresnel lens would usually result in unacceptable secondary lobe levels, these lobes can be suppressed by compounding different Fresnel patterns. The azimuthal and elevational planes can be simultaneously compounded to increase the beam quality with no loss in frame rate. A 10 MHz, 64 x 64 element crossed electrode relaxor array was fabricated on an electrostrictive 1-3 composite substrate to demonstrate the SAFE compounding approach. Experimental radiation patterns were collected and on-axis beamwidths were measured to be 380 µm and 587 µm for azimuthal and elevational plane respectively. These measurements are within the expected experimental error of the simulated values of 357 µm and 531 µm. Experimental 3D images of wire phantoms were collected using a Verasonics Vantage Imaging System and displayed with 45 dB dynamic range

One of the goals of this study was to demonstrate the ability to control the polarity across the substrate to create a focus and image in that plane. A second

goal was to demonstrate that the compounding occurred simultaneously in the azimuth and elevation planes. We found that the compounding in each plane is completed without a large effect on the other orthogonal plane (the beamwidth and secondary lobe levels do not deteriorate). The prototype 10 MHz crossed electrode array successfully demonstrated the two-way Fresnel lensing and the improvement to the focus with compounding. Each elevation slice can be collected at very high frame rates (235 Hz) so many elevation slices can be collected while still maintaining near real-time volumetric frame rates. Thus, the frame rate depends on the number of compounds per elevation slice and the number of elevation slices.

A challenge during this study was the lack of information about the electrostrictive ceramic. The electrostriction adds complexity to the material properties of the ceramic (i.e. dependence on bias, frequency, temperature, etc.) and, without a large body of literature exploring the performance of electrostrictive ultrasound transducers, we were forced to learn as we built. The experimental setup was a limitation to the imaging experiments. Bias control was achieved using a microcontroller controlling a bank of relays switching between ± 60 V biases. This presented two problems. First, the switching was slow and slowed acquisition well below real-time rates. While this functioned for wire phantom images, the objective of the project was to collect the images in real-time. Also, we were developing other imaging approaches that required bias

switching between transmit and receive so a different bias switching design was necessary. The second problem with the relay banks was because of the limitation to ±60 V biases. The bias was limited to about 3 kV/cm and prevented the operation of the array at maximum electromechanical efficiency. The final limitation to highlight is the azimuthal field of view in plane-wave imaging. When the entire array is active and pulsing at the same time the directivity is very poor. The field of view was limited to the space in front of the array (±12°). This limit is not ideal, especially for a phased array design. In future iterations, a diverging wave scheme should be used to expand the azimuthal field of view.

6.2 A 30 MHz, 3D Imaging, Forward-Looking Miniature Endoscope based on a 128-element Relaxor Array (Study 2 – Chapter 4)

Study 2 describes the design, fabrication and characterization of a 128-element crossed electrode array in a miniature endoscopic form factor suitable for minimally invasive procedures. Crossed electrode arrays address some of the key challenges surrounding probe fabrication for 3D ultrasound imaging by reducing the number of elements required ($2N$ compared to N^2). However, there remain practical challenges in packaging a high-frequency crossed electrode array into an endoscopic form factor. A process has been developed that uses a thinly diced strip of flexible circuit board to bring the back-side connections to a common bond surface, which allows the final size of the endoscope to measure only 6 mm

x 5 mm. An electrostrictive ceramic composite design was developed for the crossed electrode array. A laser dicing system was used to cut the 1-3 composite as well as etch the array electrode pattern. One and two-way pulse measurements were completed to confirm the pulse polarity and fast switching speed (3 µs). Preliminary 3D images were generated of a wire phantom using the previously described SAFE compounding imaging technique.

The crossed electrode array was successfully packaged into an endoscopic form factor. The laser micromachining of the composite and electrode pattern provided advantages beyond the ability to cut the high-frequency composite. The electrode pattern was etched in less than an hour. The pattern was not limited to the straight lines of a dicing saw but there was also no delay caused by the steps of photolithography. Wire bonding to very small pillared composites can be difficult due to the transition of materials and potential uneven surfaces. By not cutting the composite to the edge of the array the wire bond strength and yield were improved. Limitations of the study are the uncertainties around the threshold for damage during laser dicing. Future studies will compare composites cut with different laser settings (i.e. power, spot size, cut speed, number of passes, etc.) to determine the dicing program that produces the best composite.

6.3 A New 3D Imaging Technique Integrating Ultrafast Compounding, Hadamard Encoding, and Reconfigurable Fresnel Lensing (Study 3 – Chapter 5)

Study 3 describes a new 3D imaging technique that uses the flexibility and fast switching capability of the bias-sensitive substrates to create a high-quality elevation focus on a crossed electrode array. Similar to study 1, the principle behind this technique was to perform conventional compound imaging with an azimuth set of electrodes, while implementing a bias controllable elevation lens with an elevation set of electrodes. On transmit, the biases are chosen to mimic a Fresnel lens. Then, on receive, Hadamard coding is implemented along the elevation dimension. After decoding, we gain the RF data for each element across the elevation aperture even though there is effectively only one channel in that dimension. The 30 MHz, 128-element crossed electrode relaxor array described in Study 2 was used to demonstrate the performance of the imaging technique. The on-axis -6 dB beamwidths were simulated to be 175 µm and 150 µm in the azimuth and elevation direction respectively and the focus remained isotropic in the furthest elevation slice. In experiment, the beamwidths compared within reasonably expected error at 155 µm and 162 µm in azimuth and elevation. Imaging experiments were completed of ex vivo rat brains, showing the folded layers of the cerebellum throughout the volume.

The advantage of this imaging technique is that the lens concept is combined with a form of synthetic aperture imaging with increased sensitivity. The transmit lens provides some focus to select the elevation slice. Then, on receive we build a synthetic aperture by decoding the Hadamard coded data. Finally, dynamically receive beamforming focusses at all depths on receive. Also, data from neighbouring slices can be reused to improve the elevation focus without sacrificing frame rate. Using a pulse repetition rate of 40 kHz, 64 receive Hadamard codes per elevation slice and 32 elevation slices a frame rate of 19.5 volumes per second can theoretically be achieved.

The in-house beamformer was used in a mode that collects and saves channel data for the 64 signal channels. All the beamforming was completed offline in Matlab. The delay between image collection and viewing the result was a limitation in the imaging experiments, especially the brain imaging. Small adjustments to probe position that are easy to make with real-time feedback were difficult and tedious. This problem relates to another limitation, the slow speed of the beamforming. The current script takes minutes to beamform each elevation slice. This could be sped up significantly by performing the initial beamforming and decoding steps with FPGAs on the beamformer. A final limitation of this study relates to the switching artifacts between transmit and receive. When the bias switches it can cause the substrate to pulse. We have tried to mitigate the artifact by slowing the transition with an RC time constant. However, the

substrate is still pulsing, and a phantom point can be seen below the scatterer in some images. Future work should slow the bias transitions further or, possibly, have each channel switch at a slightly different time so that the net effect is smaller.

6.4 Future Directions

The limitations in the previous sections call out some obvious future work or future iterations for this imaging device. This includes a better understanding of the effects of laser machining the composite, eliminating the switching artifact and repeating ex-vivo studies with a gold standard comparison before progressing to studies that image tissue in-vivo in setups that mimic minimally invasive surgeries. The next sections speak to concepts that extend the use cases and imaging techniques presented in this dissertation.

Crossed electrode arrays greatly reduce the number of array elements and electrical connections necessary for 3D imaging. This advantage can be used to miniaturize the probes and increase the operating frequency for high-resolution imaging in endoscopic applications. In the extreme case, a 1D array with the elements bias controlled with a digital ASIC integrated into the probe can perform 2D scans with a single RF channel [178]. Alternatively, the reduced channel count could be exploited to create very large crossed electrode arrays. Large arrays would be able to image wide fields of view, even whole sections of

the body. Ultrasound is a safe and relatively low-cost imaging modality. A large field of view volume ultrasound scanner that produces high-quality images could potentially be used in place of CT or MRI scans for some applications.

6.4.1 Elevation Lens Improvement

The elevation lens is created using a pattern of polarization across the substrate to approximate a Fresnel lens. It more closely mimics a Fresnel type zone plate that creates areas of in-phase and out of phase regions in the aperture that loosely accounts for the path length difference between each element and the focal point. Compared to the traditional delay profiles in delay and sum beamforming these phase reversals are severe approximations. The work presented in this dissertation has shown several ways to improve upon the sub-standard focus, however, future work could improve upon these results. For example, the aperture size and element pitch along the Fresnel dimension of the array can be changed to improve the radiation pattern. Figure 6-1 shows how an on-axis and a steered radiation pattern changes while increasing and decreasing the element pitch (λ, 0.5λ and 1.5λ while keeping the aperture size constant) in a Field II simulation. For patterns that focus directly in front of the array there are fewer transitions from a positive bias to negative and vice versa. When the focal point starts to steer off-axis there are a lot of transitions between positive and negative bias in an ideal pattern. If the element pitch is not fine enough to

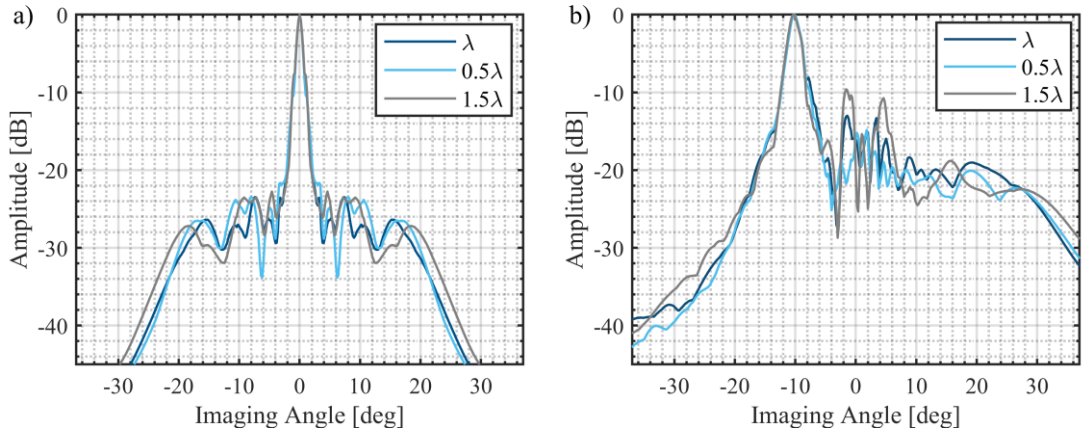

Figure 6-1 Example two-way radiation patterns from a Fresnel mimicking lens with increasing pitch a) on-axis and b) steered off-axis. The total aperture size is held constant at 64λ with the focus 8 mm deep.

capture those transitions errors occur that manifest as increased secondary lobe energy in the radiation pattern. The steering angle of a Fresnel mimicking lens is very limited. The focussed beam comes straight out from the array elements nearest to the focal point. If the focus was creased using a conventional delay profile on a phased array the beam would come out on an angle as if from the centre of the array. Consequently, the Fresnel pattern can steer the transmitted beam only as far as the edge of the array, shown in Figure 6-2. In applications where a larger field of view is required the aperture must be increased. Figure 6-3 shows a two-way simulation result where the aperture is doubled, decreasing the f-number from 2.6 to 1.3. The focus is improved at the lower f-number and the focus can be steered to much wider angles. A potential improvement can be made by reducing the aperture with increased steering angle. At larger steering angles the differences in path lengths from the element to the focus across the array are

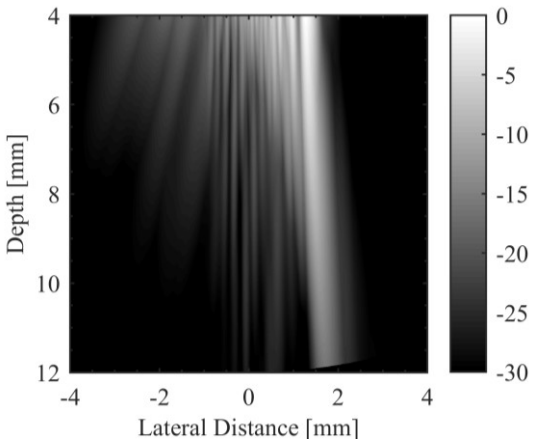

Figure 6-2 A two-way radiation pattern showing the beam direction when steered off-axis.

much larger than when using a centre focus. Because the path length differences are larger, the errors created by the Fresnel lens approximation are larger and manifest as clutter outside the focal point. The elements near the right edge of the array are not contributing to the focus but are creating unwanted energy away from the focus. To mitigate this issue, the active aperture can be decreased with steering angle. The grey dashed line in Figure 6-3 shows the small improvement when "turning off" (i.e. setting the bias to 0V) the quarter of the

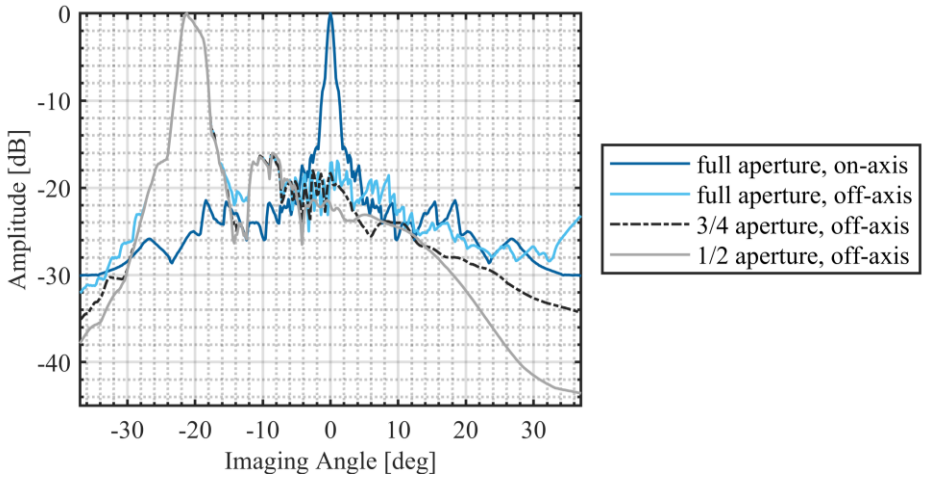

Figure 6-3 Two-way radiation patterns when the aperture is doubled to 128λ. The steered profile is improved by reducing the active aperture.

aperture that is farthest from the focus. Moreover, there is a larger improvement when half of the aperture is inactive (shown in the light grey line). If this strategy was employed as part of a compounding approach the improvements could be quite significant in the result. Reducing the active aperture size in the off-axis simulation has no effect on pressure at the focus or main beamwidth, indicating that few elements are contributing to the focus in those edge steering cases. We know that crossed electrode arrays often create edge artifacts cause by the long elements [81], [82], [91]. The edge effects are often mitigated with electronic apodization. Aperture apodization is also used along conventional arrays to reduce secondary lobe levels. If bias level control was added to the 3D imaging system, a sliding apodization window could be incorporated with the active aperture control. Figure 6-4 shows SAFE compounding results with and

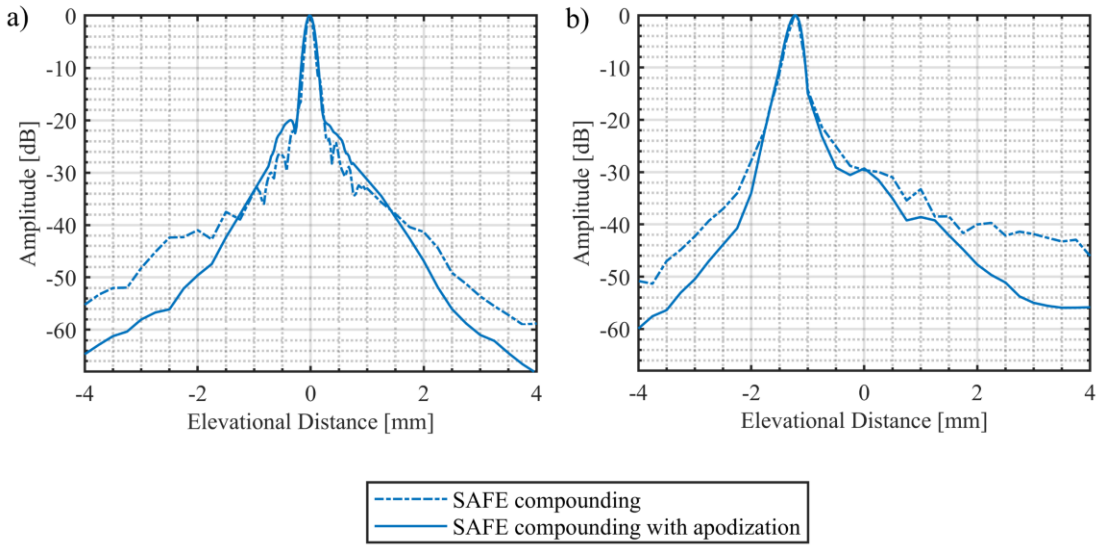

Figure 6-4 Simulation results of SAFE compounding with and without bias-controlled apodization for a focus a) on-axis and b) off-axis.

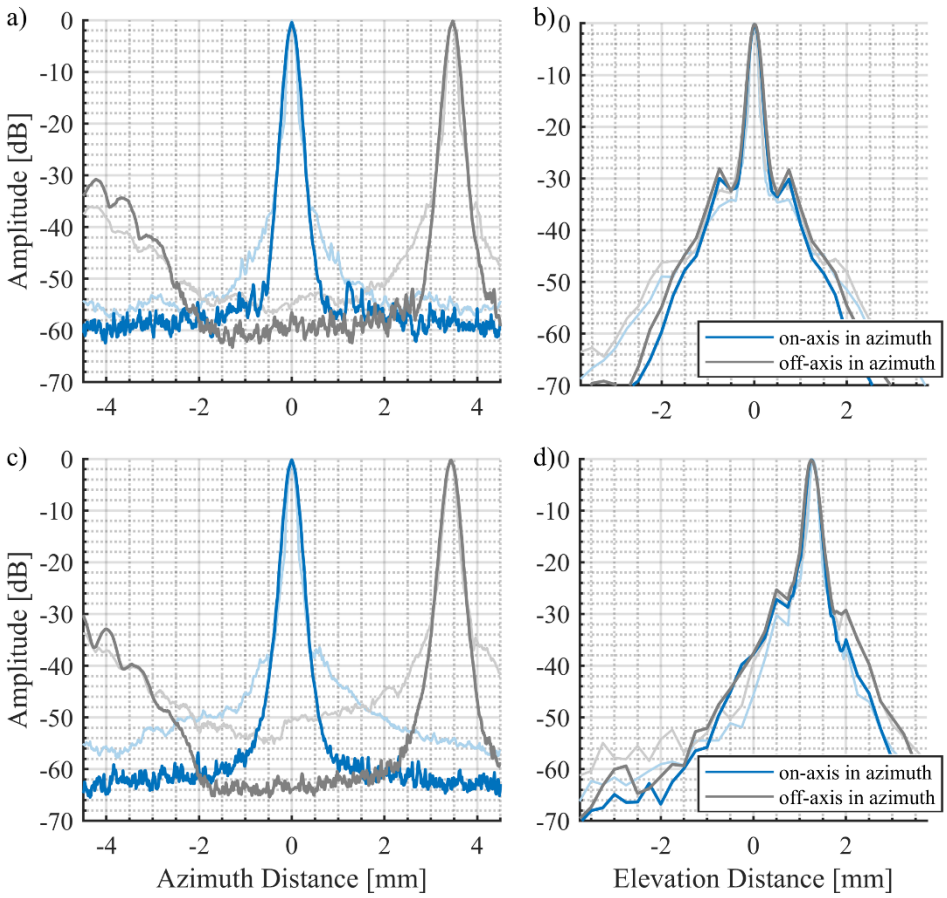

Figure 6-5 Simulated radiation patterns illustrating the performance of the imaging technique in Chapter 5 with elevation apodization in the centre elevation slice (a) and b)) and the edge elevation slice 1.3 mm from centre (c) and d)). For each slice the radiation pattern for an on-axis azimuth focus is shown in blue and the steered azimuthal focus is shown in grey. The semi-transparent lines show the reference results without apodization.

without a sliding Hamming apodization window. The apodization function is centred with the steered beam. Figure 6-5 shows the simulation results from the imaging technique combining a Fresnel transmit lens and Hadamard receive coding in elevation with ultrafast imaging in azimuth (Chapter 5) with bias level apodization. The receive apodization is applied along the aperture prior to encoding. The apodization supresses the secondary lobes by approximately 10 dB

but there is a small trade-off of main beam width on-axis. These beam shapes can be further refined by the choice of apodization function.

Apart from changing the active aperture, apodization and pitch, the Fresnel patterns themselves can be optimized. A simple cost function was used to find the set of Fresnel patterns in the second imaging technique that used the Fresnel pattern as a transmit lens and using Hadamard coding on receive. A function searched through the set of unique Fresnel patterns that focused to a given point, simulated the radiation profile and scored the result based on the area under the curve. A similar approach could be used in the future to improve the results for SAFE compounding. The set of Fresnel patterns in SAFE compounding were chosen by slightly moving the location of the focal point within the width of the elevation beam. Simulations were repeated to get the set of unique patterns that gave the best compounded beam pattern but an exhaustive search for the optimal pattern would likely be beneficial. The function could ensure that the result of each compounded frame increases the quality of the elevation lens.

6.4.2 Direct Volume Acquisition

For this dissertation, the choice was made to collect a volume image elevation slice by slice. In this acquisition scheme each slice is collected very quickly (64 insonifications) and then the elevation slice is shifted. In contrast, Hadamard coding could be performed on transmit and receive in elevation to

collect a whole volume directly. With this approach, up to 4096 insonifications (N^2) would be required because there is only one RF channel in the elevation dimension. The frame rate for the 30 MHz array would be 10 volumes/s using synthetic transmit/receive aperture imaging. The difficulty arises in properly decoding the data. The data will not decode if the phase has not been maintained over the coded patterns, making the scheme very sensitive to motion. One solution is to decrease the size of the synthetic apertures created in elevation. If we reduce the number of elements, we equally reduce the number of rows in the Hadamard matrix. Still, reducing the size of the aperture reduces the elevational resolution. Table 6-1 shows the increase in frame rate with reduced elevation aperture. Field II simulations were completed to compare the results from difference elevation aperture sizes and coding schemes. A 2D array was simulated with a 30 MHz centre frequency and the received responses were summed along the elevation dimension to model the crossed electrode array. Figure 6-6 shows simulated point spread functions in azimuth and elevation for elevation aperture of 64, 32 and 16 elements. In all cases 32 diverging waves were repeated on the 64

Table 6-1 Comparison of the volumetric frame rate with decreasing elevation aperture.

Elevation elements	Tx/Rx events	Acquisition Rate [vol/s]
64	4096	9.8
32	1024	39
16	256	156

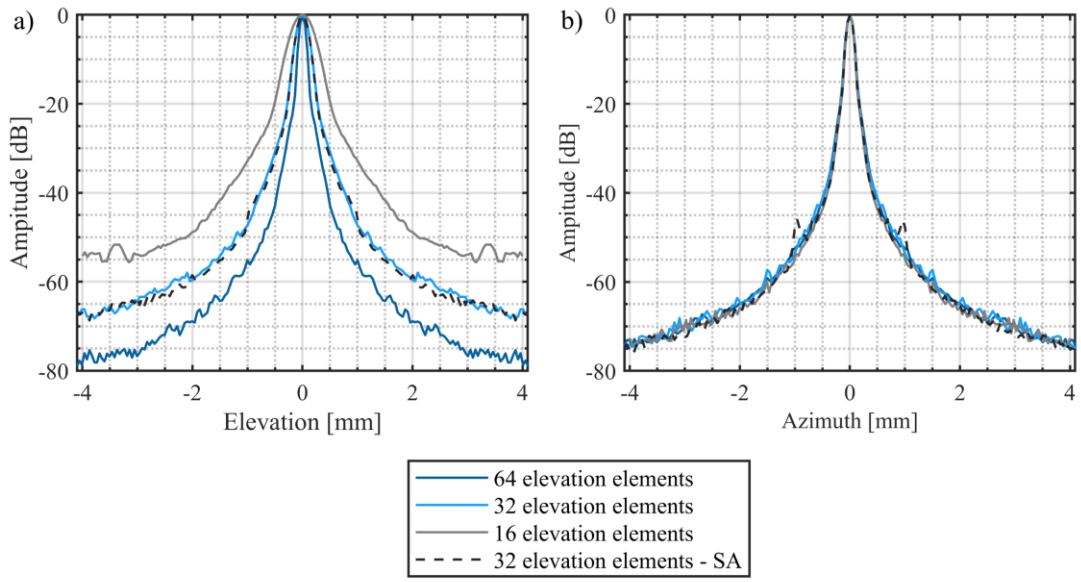

Figure 6-6 Field II simulation results from a crossed electrode array a) in elevation and b) in azimuth and reducing the size of the Hadamard coded elevation aperture.

element azimuth aperture and, as expected, the azimuth aperture was unaffected by the reduction in elevation aperture size. The black dashed line in Figure 6-6 shows the result of traditional single element synthetic aperture on transmit and receive. Using another approach, the Hadamard matrix can become sparse, effectively grouping neighbouring elevational elements or only using a subset of the Hadamard matrix. In this approach, the total aperture size is maintained so lateral resolution is not sacrificed. Figure 6-7 shows the simulation results after making the Hadamard coding sparse by a factor of two. Since the sparse codes are applied on transmit and receive the frame rate is increased by a factor of four (compared to the values listed in Table 6-1). Samson et. al. [52], [179] have shown that grating lobes can be reduced by beamforming to the centre of each element. However, the sparse Hadamard coding reduces beamformed directivity

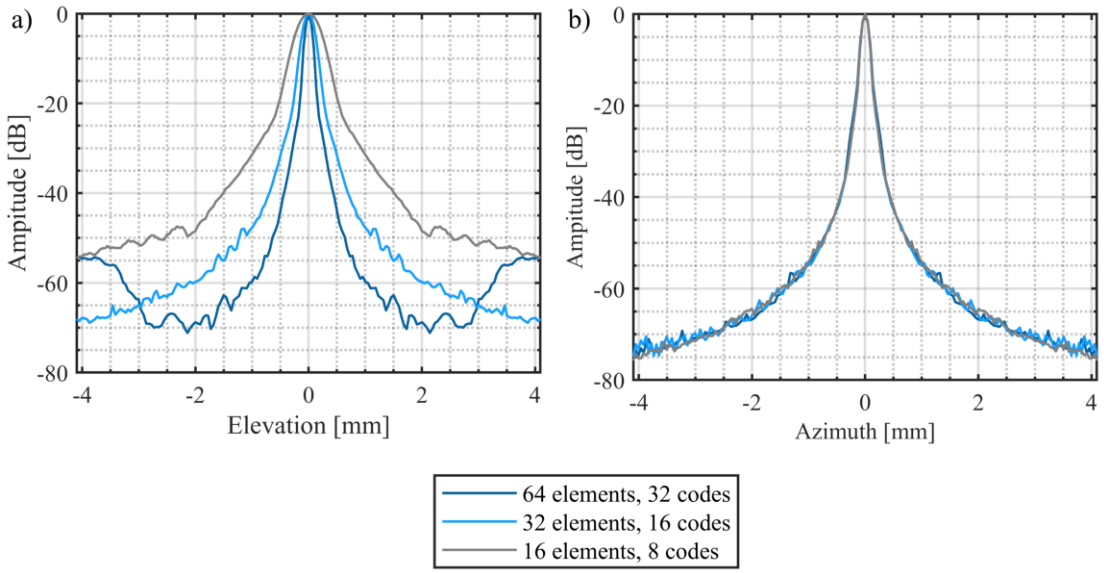

Figure 6-7 Field II simulation results from a crossed electrode array a) in elevation and b) in azimuth with the reduced Hadamard coded elevation aperture made sparse by a factor of two.

so the field of view may not be larger than the limits of the Fresnel lensing approach. A combination of different transmit and receive aperture sizes and level of sparseness may be the best choice for trading off resolution, grating lobe levels, directivity and frame rate.

A benefit of the elevation lens is that the energy is focussed on transmit in one plane. If we use a transmit and receive synthetic aperture, we have unfocussed energy in both the elevational and the azimuthal planes, therefore, a slice by slice acquisition approach will have higher SNR than a Hadamard coded approach or a single element synthetic aperture approach. Further study should include signal-to-noise and motion artifact degradation when evaluating these 3D imaging schemes through both simulation and experiment. These results should be quantified to contrast slice-by-slice acquisition to direct volume acquisition.

REFERENCES

[1] K. Latham, R. J. Zemp, and J. A. Brown, "Simulation of Fresnel Based Beam Focusing and Steering for a Crossed Electrode Array," in *Acoustics Week in Canada*, 2015.

[2] K. Latham, C. A. Samson, A. Bezanson, R. Adamson, and J. A. Brown, "Design and Preliminary Experimental Results for a High-Frequency Crossed Electrode Phased Array , Based on a Reconfigurable Fresnel Lens," in *2016 IEEE International Ultrasonics Symposium Proceedings*, 2016.

[3] C. Ceroici, K. Latham, B. A. Greenlay, J. A. Brown, and R. J. Zemp, "Fast orthogonal row-column electronic scanning experiments and comparisons," *IEEE Trans. Ultrason. Ferroelectr. Freq. Control*, vol. 66, no. 6, pp. 1093–1101, 2019.

[4] C. Ceroici *et al.*, "3D Photoacoustic Imaging Using Hadamard-Bias Encoding with Crossed Electrode Relaxor Array," *Opt. Lett.*, 2018.

[5] K. Latham, C. Ceroici, C. Samson, R. J. Zemp, and J. A. Brown, "Simultaneous Azimuth and Fresnel Elevation (SAFE) Compounding: A Fast 3D Imaging Technique for Crossed Electrode Arrays," *IEEE Trans. Ultrason. Ferroelectr. Freq. Control*, vol. 65, no. 9, pp. 1657–1668, 2018.

[6] K. Latham, C. Samson, C. Ceroici, R. J. Zemp, and J. A. Brown, "Fabrication and performance of a 128-element crossed-electrode relaxor array, for a novel 3D imaging approach," in *2017 IEEE International Ultrasonics Symposium (IUS)*, 2017, pp. 1–4.

[7] K. Latham, C. A. Samson, and J. A. Brown, "Systems and Methods for Ultrasound Beamforming using Coherently Compounded Fresnel Focussing," WO 2018/107299 Al, 2017.

[8] K. Latham, C. Samson, E. Simpson, R. Zemp, and J. A. Brown, "A 30 MHz, 3D Imaging, Forward Looking Miniature Endoscope Based on a 128-Element Relaxor Array," in *IEEE International Ultrasonics Symposium, IUS*, 2018, pp. 1–4.

[9] K. Latham, C. Samson, and E. Simpson, "A New 3D Imaging Technique Integrating Ultrafast Compounding , Hadamard Encoding , and Reconfigurable Fresnel Lensing , demonstrated on a 128-Element , Crossed Electrode Endoscope," in *2019 IEEE International Ultrasonics Symposium*, 2019, pp. 1–4.

[10] Q. Huang and Z. Zeng, "A Review on Real-Time 3D Ultrasound Imaging Technology," *Biomed Res. Int.*, vol. 2017, pp. 1–20, 2017.

[11] R. S. C. Cobbold, *Foundations of Biomedical Ultrasound*. New York: Oxford University Press, 2007.

[12] C. S. Desilets, J. D. Fraser, and G. S. Kino, "The Design of Efficient Broad-Band Piezoelectric Transducers," *IEEE Trans. Sonics Ultrason.*, vol. 25, no. 3, pp. 115–125, 1978.

[13] G. G. Haertling, "Ferroelectric Ceramics: History and Technology," *J. Am. Ceram. Soc.*, vol. 82, no. 4, pp. 797–818, 1999.

[14] B. Jaffe, W. R. Cook Jr., and H. Jaffe, *Piezoelectric Ceramics*. London and New York: Academic Press Inc., 1971.

[15] D. Damjanovic and R. E. Newnham, "Electrostrictive and Piezoelectric Materials for Actuator Applications," *J. Intell. Mater. Syst. Struct.*, vol. 3, no. 2, pp. 190–208, 1992.

[16] C. L. Hom and N. Shankar, "Fully coupled constitutive model for electrostrictive ceramic materials," *J. Intell. Mater. Syst. Struct.*, vol. 5, no. 6, pp. 795–801, 1994.

[17] S. P. Joshi, "Non-linear constitutive relations for piezoceramic materials," *Smart Mater. Struct.*, vol. 1, no. 80, pp. 80–83, 1992.

[18] J. Zhao, Q. M. Zhang, N. Kim, and T. Shrout, "Electromechanical properties of relaxor ferroelectric lead magnesium niobate-lead titanate ceramics," *Jpn. J. Appl. Phys.*, vol. 34, no. 10, pp. 5658–5663, 1995.

[19] H. Takeuchi, H. Masuzawa, C. Nakaya, and Y. Ito, "Relaxor ferroelectric transducers," *Ultrason. Symp. 1990. Proceedings., IEEE 1990*, pp. 697–705, 1990.

[20] S. Sherrit, G. Catoiu, R. B. Stimpson, and B. K. Mukherjee, "Modeling and characterization of electrostrictive ceramics," *Smart Struct. Mater. 1998 Smart Mater. Technol.*, vol. 3324, no. July, p. 161, 2003.

[21] S. Sherrit and B. K. Mukherjee, "Electrostrictive Materials: Characterization and Applications for Ultrasound," *Med. Imaging 1998 Ultrason. Transducer Eng.*, vol. 3341, no. May, pp. 196–207, 2003.

[22] S. Sherrit, G. Catoiu, and B. K. Mukherjee, *The characterisation and modelling of electrostrictive ceramics for transducers*, vol. 228, no. 1–4. 1999.

[23] W. Ren, A. J. Masys, G. Yang, and B. K. Mukherjee, "Nonlinear strain and DC bias induced piezoelectric behaviour of electrostrictive lead magnesium niobate-lead titanate ceramics under high electric fields," *J. Phys. D. Appl. Phys.*, vol. 35, no. 13, pp. 1550–1554, 2002.

[24] T. R. Shrout and J. J. Fielding, "Relaxor Ferroelectric Materials," in *Proceedings - IEEE Ultrasonics Symposium*, 1990, pp. 711–720.

[25] K. Uchino, *Advanced Piezoelectric Materials*, 2nd Ed. Woodhead Publishing, 2017.

[26] K. Uchino, "Electrostrictive Actuators: Materials and Applications.," *Am. Ceram. Soc. Bull.*, vol. 65, no. 4, pp. 647–652, 1986.

[27] K. Uchino, Y. Tsuchiya, S. Nomura, T. Sato, H. Ishikawa, and O. Ikeda, "Deformable mirror using the PMN electrostrictor," *Appl. Opt.*, vol. 20, no. 17, pp. 3077–3080, 1981.

[28] T. R. Shrout and A. Halliyal, "Preparation of Lead Based Ferroelectric Relaxors for Capacitors," *Bull. Am. Ceram. Soc.*, vol. 66, no. 4, pp. 704–711, 1987.

[29] R. E. Davidsen and S. W. Smith, "Relaxor ferroelectric materials in two-dimensional transducer arrays," in *1995 IEEE Ultrasonics Symposium*, 1995, pp. 1283–1286.

[30] R. E. Davidsen and S. W. Smith, "A multiplexed two-dimensional array for real time volumetric and B-mode imaging," in *1996 IEEE Ultrasonics Symposium. Proceedings*, 1996, vol. 2, pp. 1523–1526.

[31] J. Chen, A. Shurland, and J. Perry, "Electrostrictive transducers for medical ultrasonic applications," *Appl. Ferroelectr. 1996. ISAF '96., Proc. Tenth IEEE Int. Symp.*, vol. 1, pp. 27–30, 1996.

[32] M. I. Haller and B. T. Khuri-yakub, "A Surface Micromachined Electrostatic Ultrasonic Air Transducer," *IEEE Trans. Ultrason. Ferroelectr. Freq. Control*, vol. 43, no. 1, 1996.

[33] T. Otake, A. Sako, K. Imagawa, H. Tanaka, M. Fukada, and M. Sato, "Development of 4G CMUT (CMUT Linear SML44 probe)," 2017.

[34] I. Ladabaum, X. Jin, A. Atalar, H. T. Soh, and B. t. Khuri-Yakub, "Surface micromachined capacitive ultrasonic transducers," *IEEE Trans. Ultrason. Ferroelectr. Freq. Control*, vol. 45, no. 3, pp. 678–690, 1998.

[35] D. M. Mills, "Medical imaging with capacitive micromachined ultrasound transducer (cMUT) arrays," *Proc. - IEEE Ultrason. Symp.*, vol. 1, no. c, pp. 384–390, 2004.

[36] A. S. Ergun, G. G. Yaralioglu, and B. T. Khuri-yakub, "Capacitive Micromachined Ultrasonic Transducers: Theory and Technology," *J. Aerosp. Eng.*, vol. 16, no. 2, pp. 76–84, 2003.

[37] G. G. Yaralioglu, A. S. Ergun, B. Bayram, E. Hæggström, and B. T. Khuri-Yakub, "Calculation and measurement of electromechanical coupling coefficient of capacitive micromachined ultrasonic transducers," *IEEE Trans. Ultrason. Ferroelectr. Freq. Control*, vol. 50, no. 4, pp. 449–456, 2003.

[38] D. Leedom, R. Krimholtz, and G. Matthaei, "Equivalent circuits for transducers having arbitrary even-or odd-symmetry piezoelectric excitation.," *Sonics Ultrason. IEEE Trans.*, vol. 18, no. 3, pp. 128–141, 1971.

[39] A. R. Selfridge, G. S. Kino, and B. T. Khuri-Yakub, "Fundamental Concepts in Acoustic Transducer Array Design," in *Ultrasonics Symposium*, 1980, pp. 989–993.

[40] T. L. Szabo, *Diagnostic Ultrasound Imaging: Inside Out*, 2nd Ed. Elsevier, 2014.

[41] T. L. Szabo and P. A. Lewin, "Piezoelectric Materials for Imaging," *J. Ultrasound Med.*, vol. 26, no. 3, pp. 238–288, 2007.

[42] W. A. Smith, "The Role of Piezocomposites in Ulrasonic Transducers," in *1989 Ultrasonics Symposium*, 1989, pp. 755–766.

[43] W. A. Smith and B. A. Auld, "Modeling 1-3 Composite Piezoelectrics : Thickness-Mode Oscillations," *IEEE Trans. Ultrason. Ferroelectr. Freq. Control*, vol. 38, no. I, pp. 40–47, 1991.

[44] G. R. Lockwood and F. S. Foster, "Optimizing the Radiation Pattern of Sparse Periodic Two-Dimensional Arrays," *IEEE Trans. Ultrason. Ferroelectr. Freq. Control*, vol. 43, no. 1, pp. 15–19, 1996.

[45] G. R. Lockwood, J. R. Talman, and S. S. Brunke, "Real-time 3-D ultrasound imaging using sparse synthetic aperture beamforming.," *IEEE Trans. Ultrason. Ferroelectr. Freq. Control*, vol. 45, no. 4, pp. 980–8, Jan. 1998.

[46] G. R. Lockwood, P.-C. Li, M. O-Donnell, and F. S. Foster, "Optimizing the Radiation Pattern of Sparse Periodic Linear Arrays," *IEEE Trans. Ultrason. Ferroelectr. Freq. Control*, vol. 43, no. 1, pp. 7–14, 1996.

[47] G. Montaldo, M. Tanter, J. Bercoff, N. Benech, and M. Fink, "Coherent Plane-Wave Compounding for Very High Frame Rate Ultrasonography and Transient Elastography," *IEEE Trans. Ultrason. Ferroelectr. Freq. Control*, vol. 56, no. 3, pp. 489–506, 2009.

[48] C. Papadacci, M. Pernot, M. Couade, M. Fink, and M. Tanter, "High-contrast ultrafast imaging of the heart," *IEEE Trans. Ultrason. Ferroelectr. Freq. Control*, vol. 61, no. 2, pp. 288–301, 2014.

[49] R. Y. Chiao, L. J. Thomas, and S. D. Silverstein, "Sparse array imaging with spatially-encoded transmits," in *1997 IEEE Ultrasonics Symposium*, 1997, pp. 1679–1682.

[50] P. Gong, M. C. Kolios, and Y. Xu, "Delay-encoded transmission and image reconstruction method in synthetic transmit aperture imaging," *IEEE Trans. Ultrason. Ferroelectr. Freq. Control*, vol. 62, no. 10, pp. 1745–1756, 2015.

[51] P. Gong, P. Song, and S. Chen, "Ultrafast Synthetic Transmit Aperture Imaging Using Hadamard-Encoded Virtual Sources with Overlapping Sub-Apertures," *IEEE Trans. Med. Imaging*, vol. 36, no. 6, pp. 1372–1381, 2017.

[52] C. A. Samson, E. Simpson, R. Adamson, and J. A. Brown, "Sparse Orthogonal Diverging Wave Imaging on a High-Frequency Phased Array," in *IEEE Ultrasonics Symposium*, 2018.

[53] C. Ceroici, T. Harrison, and R. J. Zemp, "Fast Orthogonal Row-Column Electronic Scanning With Top-Orthogonal-to-Bottom Electrode Arrays," *IEEE Trans. Ultrason. Ferroelectr. Freq. Control*, vol. 64, no. 6, pp. 1009–1014, 2017.

[54] C. Ceroici, K. Latham, B. Greenlay, J. A. Brown, and R. Zemp, "Fast Orthogonal Row-Column Electronic Scanning (FORCES) Experiments and Comparisons," *Submitt. Publ.*

[55] J. A. Jensen, "Field : A Program for Simulating Ultrasound Systems," *Pap. Present. 10th Nord. Conf. Biomed. Imaging. Pap. Publ. Med. Biol. Eng. Comput.*, vol. 34, no. Supplement 1 Part 1, pp. 351–353, 1996.

[56] J. A. Jensen, "FIELD: A Program for Simulating Ultrasound Systems," *Med. Biol. Eng. Comput.*, vol. 34, no. SUPPL. 1, pp. 351–352, 1996.

[57] J. A. Jensen and N. B. Svendsen, "Calculation of Pressure Fields from Arbitrarily Shaped, Apodized, and Excited Ultrasound Transducers," *IEEE Trans. Ultrason. Ferroelectr. Freq. Control*, vol. 39, no. 2, pp. 262–267, 1992.

[58] G. E. Tupholme, "Generation of acoustic pulses by baffled plane pistons," *Mathematika*, vol. 16, no. 16, pp. 209–224, 1969.

[59] P. R. Stepanishen, "Pulsed transmit/receive response of ultrasonic piezoelectric transducers," *J. Acoust. Soc. Am.*, vol. 69, no. 6, pp. 1815–1827, 1981.

[60] P. R. Stepanishen, "Transient Radiation from Pistons in an Infinite Planar Baffle," *J. Acoust. Soc. Am.*, vol. 48, no. 1A, pp. 101–101, 1970.

[61] S. W. Smith, H. G. Pavy, and O. T. Von Ramm, "High-speed ultrasound volumetric imaging system - Part I: Transducer design and beam steering," *IEEE Trans. Ultrason. Ferroelectr. Freq. Control*, vol. 38, no. 2, pp. 100–108, 1991.

[62] O. T. Von Ramm, S. W. Smith, and H. G. Pavy, "High-speed Ultrasound Volumetric Imaging System- Part II : Parallel Processing and Image Display," *IEEE Trans. Ultrason. Ferroelectr. Freq. Control*, vol. 38, no. 2, pp. 100–108, 1991.

[63] D. P. Shattuck, M. D. Weinshenker, S. W. Smith, and O. T. von Ramm, "Explososcan: A parallel processing technique for high speed ultrasound imaging with linear phased arrays," *J. Acoust. Soc. Am.*, vol. 75, no. 4, pp. 1273–1282, 1984.

[64] B. Savord and R. Solomon, "Fully sampled matrix transducer for real time 3D ultrasonic imaging," *IEEE Symp. Ultrason.*, vol. 1, no. c, pp. 945–953, 2003.

[65] X. M. Lu, "Comprehensive design considerations for 2D matrix arrays," *Proc. - IEEE Ultrason. Symp.*, pp. 1134–1137, 2008.

[66] H. G. Kang *et al.*, "Column-based micro-beamformer for improved 2D beamforming using a matrix array transducer," *IEEE Biomed. Circuits Syst. Conf. Eng. Heal. Minds Able Bodies, BioCAS 2015 - Proc.*, pp. 2–5, 2015.

[67] R. Cobbold, *Foundations of biomedical ultrasound*. New York: Oxford University Press, 2007.

[68] D. H. Turnbull and F. S. Foster, "Beam Steering With Pulsed 2-Dimensional Transducer Arrays," *Ieee Trans. Ultrason. Ferroelectr. Freq. Control*, vol. 38, no. 4, pp. 320–333, 1991.

[69] S. S. Brunke and G. R. Lockwood, "Broad-bandwidth radiation patterns of sparse two-dimensional vernier arrays," *IEEE Trans. Ultrason. Ferroelectr. Freq. Control*, vol. 44, no. 5, pp. 1101–1109, 1997.

[70] J. T. Yen, J. P. Steinberg, and S. W. Smith, "Sparse 2-D array design for real time rectilinear volumetric imaging," *IEEE Trans. Ultrason. Ferroelectr. Freq. Control*, vol. 47, no. 1, pp. 93–110, 2000.

[71] B. Y. Mills and A. G. Little, "A High-Resolution Aerial System of a New Type," *Aust. J. Phys.*, vol. 6, p. 272, 1953.

[72] J. T. Yen and S. W. Smith, "Real-time rectilinear volumetric imaging," *Ultrasound Med. Biol.*, vol. 28, no. 7, pp. 923–931, 2002.

[73] K. Kim and T.-K. Song, "High Volume Rate 3-D Ultrasound Imaging Using Cross Array Based on Synthetic Transmit Focusing," in *IEEE Ultrasonics Symposium*, 2004, pp. 1409–1412.

[74] A. S. Logan, L. L. Wong, and J. T. W. Yeow, "2-D CMUT wafer bonded imaging arrays with a row-column addressing scheme," in *IEEE International Ultrasonics Symposium Proceedings*, 2009, pp. 984–987.

[75] A. S. Logan, L. L. P. Wong, A. I. H. Chen, and J. T. W. Yeow, "A 32 x 32 element row-column addressed capacitive micromachined ultrasonic transducer," *IEEE Trans. Ultrason. Ferroelectr. Freq. Control*, vol. 58, no. 6, pp. 1266–1271, 2011.

[76] C. H. Seo and J. T. Yen, "256x256 2-D array transducer with row-column addressing for 3-D imaging," in *IEEE Ultrasonics Symposium*, 2007, pp. 2381–2384.

[77] C. H. Seo and J. T. Yen, "Recent results using a 256x256 2-D array transducer for 3-D rectilinear imaging," in *IEEE Ultrasonics Symposium*, 2008, pp. 1146–1149.

[78] C. H. Seo and J. T. Yen, "A 256x256 2-D Array Transducer with Rectilinear Imaging," *IEEE Trans. Ultrason. Ferroelectr. Freq. Control*, vol. 56, no. 4, pp. 837–847, 2009.

[79] J. T. Yen and S. W. Smith, "Real-Time Rectilinear 3-D Ultrasound Using Receive Mode Multiplexing," *IEEE Trans. Ultrason. Ferroelectr. Freq. Control*, vol. 51, no. 2, pp. 216–226, 2004.

[80] N. M. Daher and J. T. Yen, "2-D array for 3-D ultrasound imaging using synthetic aperture techniques," *IEEE Trans. Ultrason. Ferroelectr. Freq. Control*, vol. 53, no. 5, pp. 912–924, 2006.

[81] M. F. Rasmussen, T. L. Christiansen, E. V. Thomsen, and J. A. Jensen, "3-D imaging using row-column-addressed arrays with integrated apodization - Part i: Apodization design and line element beamforming," *IEEE Trans. Ultrason. Ferroelectr. Freq. Control*, vol. 62, no. 5, pp. 947–958, 2015.

[82] T. L. Christiansen, M. F. Rasmussen, J. P. Bagge, L. N. Moesner, J. A. Jensen, and E. V. Thomsen, "3-D imaging using row-column-addressed arrays with integrated apodization-part ii: Transducer fabrication and experimental results," *IEEE Trans. Ultrason. Ferroelectr. Freq. Control*, vol. 62, no. 5, pp. 959–971, 2015.

[83] H. Bouzari, M. Engholm, S. I. Nikolov, M. B. Stuart, E. V. Thomsen, and J. A. Jensen, "Imaging Performance for Two Row-Column Arrays," *IEEE Trans. Ultrason. Ferroelectr. Freq. Control*, vol. 66, no. 7, pp. 1209–1221, 2019.

[84] A. Sampaleanu and R. Zemp, "Synthetic aperture 3D ultrasound imaging schemes with S-sequence bias-encoded top-orthogonal-to-bottom-electrode 2D CMUT arrays," in *IEEE International Ultrasonics Symposium, IUS*, 2013, pp. 1994–1997.

[85] A. Sampaleanu, P. Zhang, A. Kshirsagar, W. Moussa, and R. J. Zemp, "Top-Orthogonal-to-Bottom-Electrode (TOBE) CMUT Arrays for 3-D Ultrasound Imaging," *IEEE Trans. Ultrason. Ferroelectr. Freq. Control*, vol. 61, no. 2, pp. 266–276, 2014.

[86] R. J. Zemp, W. Zheng, and P. Zhang, "Feasibility of Top-Orthogonal-to-Bottom Electrode (TOBE) 2D CMUT arrays for low-channel-count 3D imaging," in *IEEE International Ultrasonics Symposium Proceedings*, 2011, pp. 498–502.

[87] R. J. Zemp, R. Chee, A. Sampaleanu, D. Rishi, and A. Forbrich, "S-sequence bias-encoded photoacoustic imaging with top Orthogonal to Bottom Electrode (TOBE) CMUT arrays," in *2013 Joint UFFC, EFTF and PFM Symposium*, 2013, pp. 1197–1200.

[88] A. Shaulov, M. Singer, W. A. Smith, and D. Dorman, "Biplane Phased Array for Ultrasonic Medical Imaging," in *1988 Ultrasonics Symposium*, 1988, pp. 635–638.

[89] C. E. Morton and G. R. Lockwood, "Theoretical assessment of a crossed electrode 2-D array for 3-D imaging," in *Ultrasonics, 2003 IEEE Symposium on*, 2003, pp. 968–971.

[90] A. W. Joyce and G. R. Lockwood, "Crossed-Array Transducer for Real-Time 3D Imaging," in *IEEE International Ultrasonics Symposium Proceedings*, 2014, pp. 2116–2120.

[91] C. E. M. Démoré, A. W. Joyce, K. Wall, and G. R. Lockwood, "Real-time volume imaging using a crossed electrode array.," *IEEE Trans. Ultrason. Ferroelectr. Freq. Control*, vol. 56, no. 6, pp. 1252–61, Jun. 2009.

[92] M. F. Rasmussen and J. A. Jensen, "3D ultrasound imaging performance of a row-column addressed 2D array transducer: a simulation study," in *Proceedings of SPIE*, 2013.

[93] M. F. Rasmussen and J. A. Jensen, "3-D Ultrasound Imaging Performance of a Row-Column Addressed 2-D Array Transducer : A Measurement Study 3-D Ultrasound Imaging Performance of a Row-Column Addressed 2-D Array Transducer : A Measurement Study," in *2013 Joint UFFC, EFTF and PFM Symposium*, 2013, pp. 460–463.

[94] T. L. Christiansen, M. F. Rasmussen, J. A. Jensen, and E. V. Thomsen, "Row-Column Addressed 2-D CMUT Arrays with Integrated Apodization," in *IEEE International Ultrasonics Symposium Proceedings*, 2014, pp. 600–603.

[95] S. I. Nikolov and J. A. Jensen, "Investigation of the Feasibility of 3D Synthetic Aperture Imaging," *IEEE Int. Ultrason. Symp.*, vol. 00, no. c, pp. 1903–1906, 2003.

[96] T. Harrison, A. Sampaleanu, and R. J. Zemp, "S-Sequence Spatially-Encoded Synthetic Aperture Ultrasound Imaging," *IEEE Trans. Ultrason. Ferroelectr. Freq. Control*, vol. 61, no. 5, pp. 886–890, 2014.

[97] D. . Bhattacharya and P. Tandon, "Chapter 2: Diffraction," in *Engineering Physics*, Oxford University Press, 2015, pp. 39–88.

[98] H. D. Hristov, *Fresnel Zones in Wireless Links, Zone Plate Lenses and Antennas*. Boston: Artech House, 2000.

[99] B. Hadimioglu *et al.*, "High-efficiency Fresnel acoustic lenses," in *Ultrasonics Symposium, 1993. Proceedings., IEEE 1993*, 1993, pp. 579–582.

[100] D. G. Wildes, R. Y. Chiao, C. M. W. Daft, K. W. Rigby, L. S. Smith, and K. E. Thomenius, "Elevation Performance of 1.25D and 1.5D Transducer Arrays," *IEEE Trans. Ultrason. Ferroelectr. Freq. Control*, vol. 44, no. 5, pp. 1027–1037, 1997.

[101] C. Emery, R. Lahman, and J. Kook, "Therapeutic and diagnostic electrostrictor ultrasonic arrays," WO 2008/033528 A2, 2008.

[102] C. Daft, P. Wagner, S. Panda, and I. Ladabaum, "Elevation beam profile control with bias polarity patterns applied to microfabricated ultrasound transducers," in *IEEE Symposium on Ultrasonics, 2003*, 2003, pp. 1578–1581.

[103] D. Medvedofsky *et al.*, "Three-dimensional echocardiographic quantification of the left-heart chambers using an automated adaptive analytics algorithm: Multicentre validation study," *Eur. Heart J. Cardiovasc. Imaging*, vol. 19, no. 1, pp. 47–58, 2018.

[104] M. V. Burri, D. Gupta, R. E. Kerber, and R. M. Weiss, "Review of novel clinical applications of advanced, real-time, 3-dimensional echocardiography," *Transl. Res.*, vol. 159, no. 3, pp. 149–164, 2012.

[105] R. M. Lang *et al.*, "Recommendations for cardiac chamber quantification by echocardiography in adults: An update from the American society of echocardiography and the European association of cardiovascular imaging," *Eur. Heart J. Cardiovasc. Imaging*, vol. 16, no. 3, pp. 233–271, 2015.

[106] V. Beletsky, C. C. Blake, C. D. Ainsworth, J. D. Spence, A. Fenster, and A. Tamayo, "3D Ultrasound Measurement of Change in Carotid Plaque Volume," *Stroke*, vol. 36, no. 9, pp. 1904–1909, 2005.

[107] J. Yao *et al.*, "Three-Dimensional Ultrasound Study of Carotid Arteries Before and After Endarterectomy : Analysis of Stenotic Lesions and Surgical Impact on the Vessel," *Stroke A J. Cereb. Circ.*, vol. 29, no. 10, pp. 2026–2031, 1998.

[108] A. Lyshchik, V. Drozd, and C. Reiners, "Accuracy of Three-Dimensional Ultrasound for Thyroid Volume Measurement in Children and Adolescents," *Thyroid*, vol. 14, no. 2, pp. 113–120, 2004.

[109] S. Schlögl *et al.*, "Techniques in Thyroidology The Use of Three-Dimensional Ultrasound for Thyroid Volumetry," *Thyroid*, vol. 11, no. 6, pp. 569–574, 2001.

[110] D. H. Pretorius, M. House, T. R. Nelson, and K. A. Hollenbach, "Evaluation of normal and abnormal lips in fetuses: Comparison between three- and two-dimensional sonography," *Am. J. Roentgenol.*, vol. 165, no. 5, pp. 1233–1237, 1995.

[111] G. Tonni, G. Centini, and L. Rosignoli, "Prenatal screening for fetal face and clefting in a prospective study on low-risk population: Can 3- and 4-dimensional ultrasound enhance visualization and detection rate?," *Oral Surgery, Oral Med. Oral Pathol. Oral Radiol. Endodontology*, vol. 100, no. 4, pp. 420–426, 2005.

[112] V. Wilkins-Haug, L; Levine, D; Firth, HV; Barss, *Prenatal Diagnosis of Orofacial Malformations*. Springer, 2010.

[113] R. Romero *et al.*, "A Diagnostic Approach for the Evaluation of Spina Bifida by Three-dimensional Ultrasonography," *J. Ultrasound Med.*, vol. 21, no. 6, pp. 619–626, 2017.

[114] D. D. Johnson, D. H. Pretorius, M. Riccabona, N. E. Budorick, and T. R. Nelson, "Three-dimensional ultrasound of the fetal spine," *Obstet. Gynecol. Surv.*, vol. 89, no. 3, pp. 434–438, 1997.

[115] B. R. Benacerraf *et al.*, "Three- and 4-Dimensional Ultrasound in Obstetrics and Gynecology," in *Proceedings of the American Institute of Ultrasound in Medicine Consensus Conference*, 2005, pp. 1587–1597.

[116] E. Merz and J. S. Abramowicz, "3D/4D ultrasound in prenatal diagnosis: Is it time for routine use?," *Clin. Obstet. Gynecol.*, vol. 55, no. 1, pp. 336–351, 2012.

[117] L. F. Goncalves, W. Lee, J. Espinoza, and R. Romero, "Three- and 4-Dimensional Ultrasound in Obstetric Practice: Does it Help?," *J. Ultrasound Med.*, vol. 24, pp. 1599–1624, 2005.

[118] T. R. Nelson *et al.*, "Feasibility of performing a virtual patient examination using three-dimensional ultrasonographic data acquired at remote locations.," *J. Ultrasound Med.*, vol. 20, no. 9, pp. 941–952, 2017.

[119] L. Chen *et al.*, "Comparative Study of Automated Breast 3-D Ultrasound and Handheld B-Mode Ultrasound for Differentiation of Benign and Malignant Breast Masses," *Ultrasound Med. Biol.*, vol. 39, no. 10, pp. 1735–1742, 2013.

[120] J. L. Zamorano *et al.*, "EAE/ASE Recommendations for Image Acquisition and Display Using Three-Dimensional Echocardiography," *Eur. Hear. J. - Cardiovasc. Imaging*, vol. 13, no. 1, pp. 1–46, 2012.

[121] L. K. Ryan *et al.*, "A high frequency intravascular ultrasound imaging system for investigation of vessel wall properties," in *Proceedings 1992 IEEE Ultrasonics Symposium*, 1992, pp. 1101–1105.

[122] Z. Wei, A. Fenster, D. B. Downey, L. Gardi, and M. Ding, "Needle and seed segmentation in intra-operative 3D ultrasound-guided prostate brachytherapy," *Ultrasonics*, vol. 44, pp. e331–e336, 2006.

[123] C. C. Blake, T. L. Elliot, P. J. Slomka, D. B. Downey, and A. Fenster, "Variability and accuracy of measurements of prostate brachytherapy seed position in vitro using three-dimensional ultrasound: An intra- and inter-observer study," *Med. Phys.*, vol. 27, no. 12, pp. 2788–2795, 2000.

[124] W. L. Smith, K. J. M. Surry, G. R. Mills, D. B. Downey, and A. Fenster, "Three-Dimensional Ultrasound-Guided Core Needle Breast Biopsy," *Ultrasound Med. Biol.*, vol. 27, no. 8, pp. 1025–1034, 2001.

[125] C. F. Weismann, R. Forstner, E. Prokop, and T. Rettenbacher, "Three-dimensional targeting: A new three-dimensional ultrasound technique to evaluate needle position during breast biopsy," *Ultrasound Obstet. Gynecol.*, vol. 16, no. 4, pp. 359–364, 2000.

[126] C. H. Seo and J. T. Yen, "64x64 2-D array transducer with row-column addressing," *IEEE Ultrason. Symp.*, pp. 74–77, 2006.

[127] R. E. Davidsen, "Design and Fabrication of Multiplexed Two-Dimensional Transducer Arrays Using Electrostrictive Ceramic Materials," Duke University, 1997.

[128] A. Bezanson, R. Adamson, and J. Brown, "Fabrication and performance of a miniaturized 64-element high-frequency endoscopic phased array.," *IEEE Trans. Ultrason. Ferroelectr. Freq. Control*, vol. 61, no. 1, pp. 33–43, Jan. 2014.

[129] TRS Technologies, "PMN-PT Materials for Sonar Applications," in *PMN Meeting*, 1998.

[130] TRS Technologies and TRS, "PMN-PT Electrostrictors: Property Summary of TRS PMN-PT Family."

[131] H. Wang, T. Ritter, W. Cao, and K. K. Shung, "High frequency properties of passive materials for ultrasonic transducers," *IEEE Trans. Ultrason. Ferroelectr. Freq. Control*, vol. 48, no. 1, pp. 78–84, 2001.

[132] "3D Slicer," *Slicer Solutions*, 2018. [Online]. Available: https://www.slicer.org/.

[133] T. Cummins, P. Eliahoo, and K. K. Shung, "High-Frequency Ultrasound Array Designed for Ultrasound-Guided Breast Biopsy," *IEEE Trans. Ultrason. Ferroelectr. Freq. Control*, vol. 63, no. 6, pp. 817–827, 2016.

[134] A. Bezanson, R. Adamson, and J. A. Brown, "Fabrication and Performance of a Miniaturized 64- Element High-Frequency Endoscopic Phased Array," in *2013 Joint UFFC, EFTF and PFM Symposium*, 2013, pp. 765–768.

[135] R. McPhillips *et al.*, "The fabrication and integration of a 15 MHz array within a biopsy needle," *IEEE Int. Ultrason. Symp. IUS*, vol. m, pp. 15–18, 2017.

[136] G. Schiavone *et al.*, "A highly compact packaging concept for ultrasound transducer arrays embedded in neurosurgical needles," *Microsyst. Technol.*, vol. 23, no. 9, pp. 3881–3891, 2017.

[137] H. S. Lay, B. F. Cox, V. Seetohul, C. E. M. Demore, and S. Cochran, "Design and Simulation of a Ring-Shaped Linear Array for Microultrasound Capsule Endoscopy," *IEEE Trans. Ultrason. Ferroelectr. Freq. Control*, vol. 65, no. 4, pp. 589–599, 2018.

[138] E. Light and E. Dixon-Tulloch, "Real-time 3d Ultrasound Laparoscopy," *IEEE Ultrason. Symp.*, pp. 796–799, 2005.

[139] E. C. Pua, E. D. Light, P. D. Wolf, S. W. Smith, and D. Von Allmen, "3-D ultrasound guidance of surgical robotics: A feasibility study," *Proc. - IEEE Ultrason. Symp.*, vol. 1, no. 11, pp. 993–996, 2006.

[140] S. W. S. W. Smith, W. Lee, E. D. E. D. Light, J. T. J. T. Yen, P. Wolf, and S. Idriss, "Two Dimensional Arrays for 3-D Ultrasound Imaging," in *2002 IEEE Ultrasonics Symposium*, 2002, vol. 2, pp. 1545–1553.

[141] D. E. Dausch, K. H. Gilchrist, J. B. Carlson, S. D. Hall, J. B. Castellucci, and O. T. Von Ramm, "In vivo real-time 3-D intracardiac echo using PMUT arrays," *IEEE Trans. Ultrason. Ferroelectr. Freq. Control*, vol. 61, no. 10, pp. 1754–1764, 2014.

[142] E. C. Pua, S. F. Idriss, P. D. Wolf, and S. W. Smith, "Real-time 3D transesophageal echocardiography," *Proc. - IEEE Ultrason. Symp.*, vol. 1, pp. 778–781, 2004.

[143] E. D. Light and S. W. Smith, "Two dimensional arrays for real time 3D intravascular ultrasound," *Ultrason. Imaging*, vol. 26, no. 2, pp. 115–128, 2004.

[144] W. Lee, S. F. Idriss, P. D. Wolf, and S. W. Smith, "Dual lumen transducer probes for real-time 3-D interventional cardiac ultrasound," *Ultrasound Med. Biol.*, vol. 29, no. 9, pp. 1297–1304, 2003.

[145] J. O. Fiering, P. Hultman, W. Lee, E. D. Light, and S. W. Smith, "High-density flexible interconnect for two-dimonsional ultrasound arrays," *IEEE Trans. Ultrason. Ferroelectr. Freq. Control*, vol. 47, no. 3, pp. 764–770, 2000.

[146] L. Changgeng, F. T. Djuth, Q. Zhou, and K. K. Shung, "Micromachining Techniques in Developing Ultrasonic Array Transducers," *IEEE Trans. Ultrason. Ferroelectr. Freq. Control*, vol. 60, no. 12, pp. 2615–2625, 2013.

[147] A. Bhuyan *et al.*, "Integrated circuits for volumetric ultrasound imaging with 2-D CMUT arrays," *IEEE Trans. Biomed. Circuits Syst.*, vol. 7, no. 6, pp. 796–804, 2013.

[148] A. Bhuyan *et al.*, "A 32×32 integrated CMUT array for volumetric ultrasound imaging," *IEEE Int. Ultrason. Symp. IUS*, pp. 545–548, 2013.

[149] D. Wildes *et al.*, "4-D ICE: A 2-D Array Transducer with Integrated ASIC in a 10-Fr Catheter for Real-Time 3-D Intracardiac Echocardiography," *IEEE Trans. Ultrason. Ferroelectr. Freq. Control*, vol. 63, no. 12, pp. 2159–2173, 2016.

[150] I. O. Wygant *et al.*, "Integrated ultrasonic imaging systems based on CMUT arrays: Recent progress," *Proc. - IEEE Ultrason. Symp.*, vol. 1, no. c, pp. 391–394, 2004.

[151] J. Janjic *et al.*, "A 2-D Ultrasound Transducer With Front-End ASIC and Low Cable Count for 3-D Forward-Looking Intravascular Imaging: Performance and Characterization," *IEEE Trans. Ultrason. Ferroelectr. Freq. Control*, vol. 65, no. 10, pp. 1832–1844, 2018.

[152] M. Tan *et al.*, "A front-end ASIC with high-voltage transmit switching and receive digitization for 3-D forward-looking intravascular ultrasound imaging," *IEEE J. Solid-State Circuits*, vol. 53, no. 8, pp. 2284–2297, 2018.

[153] C. Tekes *et al.*, "3-D real-time volumetric imaging using 20 MHz 1.5-mm diameter single-chip CMUT-on-CMOS array," *IEEE Int. Ultrason. Symp. IUS*, pp. 2–5, 2012.

[154] G. Gurun *et al.*, "Single-chip CMUT-on-CMOS front-end system for real-time volumetric IVUS and ICE imaging," *IEEE Trans. Ultrason. Ferroelectr. Freq. Control*, vol. 61, no. 2, pp. 239–250, 2014.

[155] F. L. Degertekin, R. O. Guldiken, and M. Karaman, "Annular-ring CMUT arrays for forward-looking IVUS: Transducer characterization and imaging," *IEEE Trans. Ultrason. Ferroelectr. Freq. Control*, vol. 53, no. 2, pp. 474–482, 2006.

[156] A. I. H. Chen, L. L. P. Wong, and J. T. W. Yeow, "A CMUT-based Finger-mounted 3D Ultrasound Probe," in *IEEE International Ultrasonics Symposium Proceedings*, 2014, pp. 1603–1606.

[157] J. T. Yen, C. H. Seo, S. I. Awad, and J. S. Jeong, "A dual-layer transducer array for 3-D rectilinear imaging," *IEEE Trans. Ultrason. Ferroelectr. Freq. Control*, vol. 56, no. 1, pp. 204–212, 2009.

[158] T. L. Christiansen, C. Dahl-Petersen, J. A. Jensen, and E. V. Thomsen, "2-D row-column CMUT arrays with an open-grid support structure," in *IEEE International Ultrasonics Symposium Proceedings*, 2013, pp. 1712–1715.

[159] D. H. Turnbull and F. S. Foster, "In vivo ultrasound biomicroscopy in developmental biology," *Trends Biotechnol.*, vol. 20, no. 8, pp. 29–33, 2002.

[160] F. S. Foster *et al.*, "High frequency ultrasound imaging: From man to mouse," *Proc. IEEE Ultrason. Symp.*, vol. 2, pp. 1633–1638, 2000.

[161] T. G. Landry and J. A. Brown, "B-mode and Doppler imaging of in vivo rat brain and ex vivo human brain with a high frequency endoscopic phased array," *IEEE Int. Ultrason. Symp. IUS*, vol. 2019-Octob, pp. 2133–2136, 2019.

[162] E. Macé, G. Montaldo, I. Cohen, M. Baulac, M. Fink, and M. Tanter, "Functional ultrasound imaging of the brain," *Nat. Methods*, vol. 8, no. 8, pp. 662–664, 2011.

[163] C. Errico *et al.*, "Ultrafast ultrasound localization microscopy for deep super-resolution vascular imaging," *Nature*, vol. 527, no. 7579, pp. 499–502, 2015.

[164] J. Sun, L. Lindvere, A. Dorr, M. Van Raaij, B. Stefanovic, and S. Foster, "Functional imaging of the rat brain with micro-ultrasound," *Proc. - IEEE Ultrason. Symp.*, pp. 325–328, 2009.

[165] M. Imbault, D. Chauvet, J. L. Gennisson, L. Capelle, and M. Tanter, "Intraoperative Functional Ultrasound Imaging of Human Brain Activity," *Sci. Rep.*, vol. 7, no. 1, pp. 1–7, 2017.

[166] G. Unsgaard *et al.*, "Brain operations guided by real-time two-dimensional ultrasound: New possibilities as a result of improved image quality," *Neurosurgery*, vol. 51, no. 2, pp. 402–412, 2002.

[167] D. Chauvet *et al.*, "In Vivo Measurement of Brain Tumor Elasticity Using Intraoperative Shear Wave Elastography," *Ultraschall der Medizin*, vol. 37, no. 6, pp. 584–590, 2016.

[168] C. A. Samson, A. Bezanson, and J. A. Brown, "A Sub-Nyquist, Variable Sampling, High-Frequency Phased Array Beamformer," *IEEE Trans. Ultrason. Ferroelectr. Freq. Control*, vol. 64, no. 3, pp. 568–576, Mar. 2017.

[169] J. Chen and T. R. Gururaja, "DC-biased electrostrictive materials and transducers for medical imaging," *Proc. IEEE Ultrason. Symp.*, vol. 2, pp. 1651–1658, 1997.

[170] M. Lukacs, M. Sayer, G. Lockwood, and S. Foste, "Laser Micromachined High Frequency Ultrasonic Arrays," in *Ultrasonics Symposium, 1999. Proceedings. 1999 IEEE*, 1999, pp. 1209–1212.

[171] M. Lukacs *et al.*, "Performance and characterization of high frequency linear arrays," *Proc. - IEEE Ultrason. Symp.*, vol. 1, no. 10, pp. 105–108, 2005.

[172] R. Farlow, W. Galbraith, M. Knowles, G. Hayward, and S. Member, "Micromachining of a piezocomposite transducer using a copper vapor laser," *IEEE Trans. Ultrason. Ferroelectr. Freq. Control*, vol. 48, no. 3, pp. 639–640, 2001.

[173] K. Snook, T. Shrout, and K. K. Shung, "Design of a 50 MHz annular array using fine-grain lead titanate," *IEEE Int. Symp. Appl. Ferroelectr.*, no. 0, pp. 351–354, 2002.

[174] X. Jiang, J. R. Yuan, A. Cheng, K. Snook, and P. J. Cao, "Microfabrication of Piezoelectric Composite Ultrasound Transducers (PC-MUT)," in *2006 IEEE Ultrasonics Symposium*, 2006, pp. 918–921.

[175] A. Ramalli, E. Boni, A. S. Savoia, and P. Tortoli, "Density-tapered spiral arrays for ultrasound 3-D imaging," *IEEE Trans. Ultrason. Ferroelectr. Freq. Control*, vol. 62, no. 8, pp. 1580–1588, 2015.

[176] A. Austeng and S. Holm, "Sparse 2-D arrays for 3-D phased array imaging - Design methods," *IEEE Trans. Ultrason. Ferroelectr. Freq. Control*, vol. 49, no. 8, pp. 1073–1086, 2002.

[177] A. Austeng and S. Holm, "Sparse 2-D Arrays for 3-D Phased Array Imaging - Experimental Validation," *IEEE Trans. Ultrason. Ferroelectr. Freq. Control*, vol. 49, no. 8, pp. 1087–1093, 2002.

[178] E. Simpson, K. Latham, and C. Samson, "Single-Channel Hadamard Encoded Endoscope for High-Frequency IVUS Imaging," in *2019 IEEE International Ultrasonics Symposium*, 2019, pp. 1–4.

[179] C. Samson, R. Adamson, and J. A. Brown, "Ultrafast Phased Array Imaging using Sparse Orthogonal Diverging Waves," *IEEE Trans. Ultrason. Ferroelectr. Freq. Control*, 2020.

[180] R. Kikinis, S. D. Pieper, and K. G. Vosburgh, "3D Slicer: A Platform for Subject-Specific Image Analysis, Visualization, and Clinical Support," in *Intraoperative Imaging and Image-Guided Therapy*, F. Jolesz, Ed. New York: Springer, 2014, pp. 277–289.

[181] APC International Inc., "Piezoelectricity," 2016. [Online]. Available: https://www.americanpiezo.com/knowledge-center/piezo-theory/piezoelectricity.html.

[182] I. L. Guy, S. Muensit, and E. M. Goldys, "Electrostriction in gallium nitride," *Appl. Phys. Lett.*, vol. 75, no. 23, pp. 3641–3643, 1999.

[183] R. O. Guldiken, J. McLean, and F. L. Degertekin, "CMUTS with dual-electrode structure for improved transmit and receive performance," *IEEE Trans. Ultrason. Ferroelectr. Freq. Control*, vol. 53, no. 2, pp. 483–491, 2006.

APPENDIX A
EXAMPLE SIMULATION SCRIPT

The following is an example Field II simulation script used to evaluate the volume imaging technique using a Fresnel transmit elevation lens and Hadamard receive coding combined with ultrafast imaging in azimuth. This script can be used to simulate the capture and beamforming for each elevation slice in the volume. The simulated phantom can model a wire/point target in a water bath or tissue.

```
%%%%%% in this version an azimuthal image is made for each compound number
%%%%%% (receive Hadamard code / DW virtual point), the images are decoded
%%%%%% and elevational beamforming delay are applied.

clear all
% close all
path('D:\Field II\m-files',path);

% az_bf_mode = 'planewave';
az_bf_mode = 'divergingwave';
tic;

% ---- Make folder for saving data
currentFolder = pwd;
newSubFolder = strcat(datestr(now,'mm-dd-yyyy HH-MM'),'_',az_bf_mode,'sim_vol');
if ~exist(newSubFolder, 'dir')
  mkdir('FRHAD\sim_im', newSubFolder) ;
end

% sim_slices = [1:32];
sim_slices = 3;

% Field II
% ---- Start Field II and set initial parameters
field_init(0);
f0=30.0e6;                          % center frequency [Hz]
fs=1e9;                             % sampling frequency [Hz]
c = 1500;                           % speed of sound [m/s]
lambda = c/f0;                      % wavelength [m]
```

```
focus = [0 0 0]/1000;                % fixed focal point [m]
N = 64;                              % number of physical elements
kerf = 8e-6;                         % kerf [m]
el_width = 48e-6-kerf;               % element width [m]
height = N*el_width;                 % height of element [m]
pitch= el_width + kerf;

% ---- Set the sampling frequency, the medium sound speed
set_sampling(fs);
set_field('c',c);
Ts = 1/fs;                           % Sampling period [s]

% ---- Define the transducer
Ny = 64;
enabled = ones(N,Ny); % all elements enabled
tx_aperture = xdc_2d_array (N, Ny, el_width, height/Ny, kerf, kerf, enabled, 1, 1,
focus);
rx_aperture = xdc_2d_array (N, Ny, el_width, height/Ny, kerf, kerf, enabled, 1, 1,
focus);

aperture_data = xdc_get(tx_aperture,'rect');
el_pos_az = aperture_data(24,1:64);
el_pos_el = aperture_data(25,1:64:4096);


% ----  Set the excitation signal
excitation=sin(2*pi*f0*(0:1/fs:1/f0));
excitation = excitation/(max(excitation));
xdc_excitation(tx_aperture, excitation);

% ---- Set the aperture impulse response
impulse_response=sin(2*pi*f0*(0:1/fs:2/f0));
impulse_response=impulse_response.*hanning(max(size(impulse_response)))';
xdc_impulse (tx_aperture, impulse_response);
xdc_impulse (rx_aperture, impulse_response);

xdc_focus_times(tx_aperture,0,zeros(1,N*Ny));
xdc_focus_times(rx_aperture,0,zeros(1,N*Ny));

xdc_apodization(tx_aperture,0,ones(1,N*Ny));
xdc_apodization(rx_aperture,0,ones(1,N*Ny));

% ---- Read in Fresnel patterns
line_spacing = 2*50e-6;
line_loc = -15*line_spacing:line_spacing:16*line_spacing;
line_loc = -line_loc;
A =
readmatrix('D:\SystemFirmware\BiasFirmware\Bias_generation_FrTx_HadRx_optimizedFr.xlsx','
Sheet','FresnelLens','Range','B2:BM65');
num_lines = length(line_loc);
num_comps = size(A,1);
num_slices = num_lines;

apod = A(1:num_lines,:);
```

```
apod(apod == 0) = -1;

H = hadamard(N);
apod_H = H;
invH = transpose(H);

if(strcmp(az_bf_mode,'planewave')) % ---- Calculate plane wave delays
    ang = linspace(-10,10,num_comps)*pi/180;
        ang = zeros(size(ang));
        foc = 10e3;
        for nc=1:num_comps
            x_tmp = foc*sin(ang(nc));
            y_tmp = 0;
            z_tmp = foc*cos(ang(nc));
            for x1 = 1:N
                del(nc,x1) = (sqrt((x_tmp-el_pos(x1))^2 + y_tmp^2 + z_tmp^2))/c;
            end
            del(nc,:) = del(nc,:) - min(del(nc,:));
        end

    apod_tx = apod;
    apod_rx = apod_H;

elseif(strcmp(az_bf_mode,'divergingwave'))% ---- Calculate diverging wave delays
    theta_aperture = 50*pi/180;                              % subaperture angle
    el = (1:1:N);
    no_vp = 32;

    no_sub_el = N-no_vp+1;                                   % number of elements in the
sub-aperture
    z_vp = -no_sub_el*el_width/(2*tan(theta_aperture/2));   % z position of the virtual
point sources
    x_vp = repmat(el_pos_az((N-no_vp)/2+1:1:(N-no_vp)/2+no_vp),1,2);

    for nc=1:num_comps
        for x1 = 1:N
            del(nc,x1) = sqrt((z_vp)^2 + (el_pos_az(x1)-x_vp(nc))^2 )/c;
        end
    end

    apod_tmp = ones(N,1);
    apod_tmp(33+1:end) = 0;
    ind = [0:31 0:31];
    for nc = 1:N
        apod_div(:,nc) = circshift(apod_tmp,ind(nc));
    end
    apod_tx = (apod);
    apod_rx = apod_H;

elseif(strcmp(az_bf_mode,'noazbf'))% ---- Calculate 0 dels
    del = zeros(N,N);
    apod_tx = (apod);
    apod_rx = apod_H;
end
```

```
z_foc = 160*lambda;

% % ---- Define the simulation grid for field calculations.
xmin = -100*lambda;
xmax = 100*lambda;
thmin = -38*pi/180;
thmax = 38*pi/180;
ymin = 0;
ymax = 0;
zmin = 90*lambda;
zmax = 240*lambda;
ypoints = 1;
zpoints = 2*512;
no_lines = 141;

dx = (xmax-xmin)/no_lines;
% dy = (ymax-ymin)/ypoints;
dz = (zmax-zmin)/zpoints;

th = linspace(thmin,thmax,no_lines);
r = linspace(zmin,zmax,zpoints);
[th_mesh, r_mesh] = meshgrid(th,r);

% ----  Set phantom positions
phantom_position=[0 line_loc(16)*1000 z_foc*1000]/1000;
phantom_amplitude = ones(size(phantom_position,1),1);

delay_tot = zeros(zpoints,no_lines);
vol_image = zeros(zpoints,no_lines,num_slices);

no_neighbor_slices = 1;
upsamp_int = 4;

epsilon = 1.2*1000;
apo = exp((-el_pos_az.^2)/(epsilon*el_pos_az(1))^2);

for sl = sim_slices
    if ~rem(no_neighbor_slices,2)
      no_neighbor_slices = no_neighbor_slices +1;
    end

    slice_seq = linspace(sl-
floor(no_neighbor_slices/2),sl+floor(no_neighbor_slices/2),no_neighbor_slices);

    for nl = 1:no_neighbor_slices
        %%%% ---- SIMULATE IMAGING AND DATA COLLECTION
        %     pl
        fprintf ('slice %d of %d \n', sl, num_slices)

        % ---- Pre-allocate some storage
        image_data = zeros(1000,N,num_comps);
        bf_image = zeros(zpoints,no_lines,num_comps);
        rough_image = zeros(zpoints,no_lines,num_comps);
```

```
        deco_image = zeros(zpoints*upsamp_int,no_lines,num_comps);
        capture_times = zeros(num_comps,1);

        for nc=1:num_comps
            xdc_focus_times(tx_aperture,0,repmat(del(nc,:),1,Ny));
            xdc_focus_times(rx_aperture,0,zeros(1,N*Ny));

            if(strcmp(az_bf_mode,'divergingwave'))

xdc_apodization(tx_aperture,0,reshape(repmat(apod_tx(slice_seq(nl),:),Ny,1).*repmat(apod_
div(:,nc),1,N),1,N*Ny));
            else

xdc_apodization(tx_aperture,0,reshape(repmat(apod_tx(slice_seq(nl),:),Ny,1),1,N*Ny));
            end
            xdc_apodization(rx_aperture,0,reshape(repmat(apod_rx(nc,:),Ny,1),1,N*Ny));

            % Calculate the received response
            [v, t1]=calc_scat_multi(tx_aperture, rx_aperture, phantom_position,
phantom_amplitude);
            % Store the result
            v_2 = reshape(v,size(v,1),N,Ny);
            image_data(1:max(size(v_2)),:,nc)= sum(v_2,3);
            capture_times(nc) = t1;
        end

        % ----- define beamforming delays
        for x1=1:N
            delay_rx(:,:,x1) = sqrt((el_pos_az(x1)-r_mesh.*sin(th_mesh)).^2 +
(line_loc(sl)).^2 + (r_mesh.*cos(th_mesh)).^2)/c;
        end

        if(strcmp(az_bf_mode,'planewave')) % ---- Calculate plane wave beamforming delays
            for nc = 1:num_comps
                delay_tx(:,:,nc) = sqrt( (z_mesh*cos(ang(nc)) + x_mesh*sin(ang(nc))).^2 +
line_loc(sl)^2)/c + del(nc,32) ;
            end
        elseif(strcmp(az_bf_mode,'divergingwave'))% ---- Calculate diverging wave
beamforming delays
            for nc = 1:num_comps
                delay_tx(:,:,nc) = sqrt( ((r_mesh.*cos(th_mesh))-z_vp).^2 +
((r_mesh.*sin(th_mesh)) - x_vp(nc)).^2 + line_loc(sl).^2)/c;
            end
        elseif(strcmp(az_bf_mode,'noazbf'))% ---- Calculate plane waves
            for nc = 1:N
                delay_tx(:,:,nc) = r_mesh/c;
            end
        end

        for xe = 1:N
            delay_el(:,:,xe) = sqrt( (el_pos_el(xe)-(line_loc(sl))).^2/2 +
(r_mesh.*sin(th_mesh)).^2  + (r_mesh.*cos(th_mesh)).^2) ;
        end
```

```
        zpad = 10;
        image_data = [zeros(zpad,N,num_comps);image_data;zeros(zpad,N,num_comps)];
        [L,~,~] = size(image_data);

        %%%% ---- BEAMFORM SLICE PT 1.
        % beamform in azimuth
        for x1 = 1:N
            clearvars delay_size datamat_temp
            for xc = 1:N
                delay_tot = delay_rx(:,:,x1) + delay_tx(:,:,xc)-capture_times(xc);
                delay_size = delay_tot*fs + zpad;
                delay_size(abs(delay_size)>L)=L;                % prevents delay to shift
outside image
                delay_size = ceil(delay_size);                  % rounds sample delay up
                delay_size(delay_size<2)=2;

                datamat_temp = apo(x1)*image_data(:,x1,xc);

                rough_image(:,:,xc) = rough_image(:,:,xc) +
double(datamat_temp(delay_size));
            end
        end
        % ------ upsample image
        for samp = 1:N
            resamp_image(:,:,samp) = resample(rough_image(:,:,samp),upsamp_int ,1);
        end

        %%%% ---- DECODE ROUGH IMAGES
        for l = 1:no_lines
            for d = 1:zpoints*upsamp_int
                deco_image(d,l,:)= invH*(squeeze(resamp_image(d,l,:)));
            end
        end
        clearvars delay_tot delay_size
        %%%% ---- BEAMFORM SLICE PT 2. (phase and combine elevation)
        for px = 1:no_lines
            for xe = 1:N
                delay_tot = delay_el(:,px,xe) - zmin;

                delay_size = delay_tot/(dz/upsamp_int);

                delay_size((delay_size)>(zpoints*upsamp_int))=(zpoints*upsamp_int); %
prevents delay to shift outside image
                delay_size = floor(delay_size); % rounds sample delay up
                delay_size(delay_size<2)=2;

                datamat_temp = deco_image(:,px,xe);

                bf_image(:,px,nl) = bf_image(:,px,nl) + double(datamat_temp(delay_size));
% adds contribution from each element to each pixel location

            end
        end
    end
```

```
    vol_image(:,:,sl) = abs(hilbert(sum(bf_image,3)));
    save(strcat('FRHAD\sim_im\', newSubFolder,'/slice', sprintf('%d',sl), '.mat'),
'th','r','sl','line_loc', 'bf_image');

end

bf_image_compounded = sum(bf_image,3);
im= abs(hilbert(bf_image_compounded));
im2 = im/max(im(:));
[cartim, x, z]= ultrasound_cart2pol(min(r)*1000, max(r)*1000, zpoints, no_lines,
min(th)*180/pi, max(th)*180/pi, im2);

im2_db = 20*log10(cartim);

figure
imagesc(x,z,im2_db);caxis([-60 0]);colormap('gray')
xlabel('Azimuth Distance [mm]')
ylabel('Depth [mm]')

profile = max(cartim);
figure
plot(x,20*log10(profile/max(profile)))
xlim([-3.75,3.75])
ylim([-60,0])
xlabel('Azimuth Distance [mm]')
ylabel('Amplitude [dB]')
toc
field_end;
```

APPENDIX B
COPYRIGHT PERMISSION LETTERS

5/14/2020 Rightslink® by Copyright Clearance Center

RightsLink

Home | Help | Email Support | Sign in | Create Account

IEEE Requesting permission to reuse content from an IEEE publication

Simultaneous Azimuth and Fresnel Elevation Compounding: A Fast 3-D Imaging Technique for Crossed-Electrode Arrays

Author: Katherine Latham
Publication: Ultrasonics, Ferroelectrics and Frequency Control, IEEE Transactions on
Publisher: IEEE
Date: Sept. 2018

Copyright © 2018, IEEE

Thesis / Dissertation Reuse

The IEEE does not require individuals working on a thesis to obtain a formal reuse license, however, you may print out this statement to be used as a permission grant:

Requirements to be followed when using any portion (e.g., figure, graph, table, or textual material) of an IEEE copyrighted paper in a thesis:

1) In the case of textual material (e.g., using short quotes or referring to the work within these papers) users must give full credit to the original source (author, paper, publication) followed by the IEEE copyright line © 2011 IEEE.
2) In the case of illustrations or tabular material, we require that the copyright line © [Year of original publication] IEEE appear prominently with each reprinted figure and/or table.
3) If a substantial portion of the original paper is to be used, and if you are not the senior author, also obtain the senior author's approval.

Requirements to be followed when using an entire IEEE copyrighted paper in a thesis:

1) The following IEEE copyright/ credit notice should be placed prominently in the references: © [year of original publication] IEEE. Reprinted, with permission, from [author names, paper title, IEEE publication title, and month/year of publication]
2) Only the accepted version of an IEEE copyrighted paper can be used when posting the paper or your thesis on-line.
3) In placing the thesis on the author's university website, please display the following message in a prominent place on the website: In reference to IEEE copyrighted material which is used with permission in this thesis, the IEEE does not endorse any of [university/educational entity's name goes here]'s products or services. Internal or personal use of this material is permitted. If interested in reprinting/republishing IEEE copyrighted material for advertising or promotional purposes or for creating new collective works for resale or redistribution, please go to http://www.ieee.org/publications_standards/publications/rights/rights_link.html to learn how to obtain a License from RightsLink.

If applicable, University Microfilms and/or ProQuest Library, or the Archives of Canada may supply single copies of the dissertation.

BACK CLOSE WINDOW

© 2020 Copyright - All Rights Reserved | Copyright Clearance Center, Inc. | Privacy statement | Terms and Conditions
Comments? We would like to hear from you. E-mail us at customercare@copyright.com

https://s100.copyright.com/AppDispatchServlet#formTop 1/1

Thank you for your order!

Dear Katherine Latham,

Thank you for placing your order through Copyright Clearance Center's RightsLink® service.

Order Summary

Licensee:	Katherine Latham
Order Date:	Jul 17, 2020
Order Number:	4871441030194
Publication:	Journal of the American Ceramic Society
Title:	Ferroelectric Ceramics: History and Technology
Type of Use:	Dissertation/Thesis
Order Total:	0.00 CAD

View or print complete details of your order and the publisher's terms and conditions.

Sincerely,

Copyright Clearance Center

Tel: +1-855-239-3415 / +1-978-646-2777
customercare@copyright.com
https://myaccount.copyright.com

Copyright Clearance Center RightsLink®

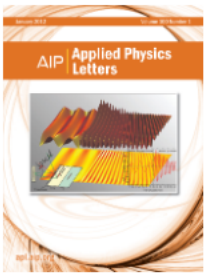

Thank you for your order!

Dear Katherine Latham,

Thank you for placing your order through Copyright Clearance Center's RightsLink® service.

Order Summary

Licensee:	Katherine Latham
Order Date:	Jul 16, 2020
Order Number:	4870880205689
Publication:	Applied Physics Letters
Title:	Electrostriction in gallium nitride
Type of Use:	Thesis/Dissertation
Order Total:	0.00 CAD

View or print complete details of your order and the publisher's terms and conditions.

Sincerely,

Copyright Clearance Center

Tel: +1-855-239-3415 / +1-978-646-2777
customercare@copyright.com
https://myaccount.copyright.com

Copyright Clearance Center RightsLink®

CMUTS with dual electrode structure for improved transmit and receive performance

Author: R.O. Guldiken
Publication: Ultrasonics, Ferroelectrics and Frequency Control, IEEE Transactions on
Publisher: IEEE
Date: Feb. 2006

Thesis / Dissertation Reuse

The IEEE does not require individuals working on a thesis to obtain a formal reuse license, however, you may print out this statement to be used as a permission grant:

Requirements to be followed when using any portion (e.g., figure, graph, table, or textual material) of an IEEE copyrighted paper in a thesis:

1) In the case of textual material (e.g., using short quotes or referring to the work within these papers) users must give full credit to the original source (author, paper, publication) followed by the IEEE copyright line © 2011 IEEE.
2) In the case of illustrations or tabular material, we require that the copyright line © [Year of original publication] IEEE appear prominently with each reprinted figure and/or table.
3) If a substantial portion of the original paper is to be used, and if you are not the senior author, also obtain the senior author's approval.

Requirements to be followed when using an entire IEEE copyrighted paper in a thesis:

1) The following IEEE copyright/ credit notice should be placed prominently in the references: © [year of original publication] IEEE. Reprinted, with permission, from [author names, paper title, IEEE publication title, and month/year of publication]
2) Only the accepted version of an IEEE copyrighted paper can be used when posting the paper or your thesis on-line.
3) In placing the thesis on the author's university website, please display the following message in a prominent place on the website: In reference to IEEE copyrighted material which is used with permission in this thesis, the IEEE does not endorse any of [university/educational entity's name goes here]'s products or services. Internal or personal use of this material is permitted. If interested in reprinting/republishing IEEE copyrighted material for advertising or promotional purposes or for creating new collective works for resale or redistribution, please go to http://www.ieee.org/publications_standards/publications/rights/rights_link.html to learn how to obtain a License from RightsLink.

If applicable, University Microfilms and/or ProQuest Library, or the Archives of Canada may supply single copies of the dissertation.

BACK CLOSE WINDOW

Marketplace™

American Society of Civil Engineers - License Terms and Conditions

This is a License Agreement between Katherine Latham ("You") and American Society of Civil Engineers ("Publisher") provided by Copyright Clearance Center ("CCC"). The license consists of your order details, the terms and conditions provided by American Society of Civil Engineers, and the CCC terms and conditions.

All payments must be made in full to CCC.

Order Date	23-Jul-2020	**Type of Use**	Republish in a thesis/dissertation
Order license ID	1050418-1		
ISSN	0893-1321	**Publisher**	American Society of Civil Engineers
		Portion	Chart/graph/table/figure

LICENSED CONTENT

Publication Title	Journal of Aerospace Engineering	**Country**	United States of America
		Rightsholder	American Society of Civil Engineers
Author/Editor	American Society of Civil Engineers	**Publication Type**	Journal
Date	01/01/1988		
Language	English		

REQUEST DETAILS

Portion Type	Chart/graph/table/figure	**Distribution**	Canada
Number of charts / graphs / tables / figures requested	2	**Translation**	Original language of publication
		Copies for the disabled?	No
Format (select all that apply)	Print, Electronic	**Minor editing privileges?**	No
Who will republish the content?	Academic institution	**Incidental promotional use?**	No
Duration of Use	Current edition and up to 5 years	**Currency**	CAD
Lifetime Unit Quantity	Up to 499		
Rights Requested	Main product		

NEW WORK DETAILS

Title	Bias Controlled Imaging for a Endoscopic 3D Ultrasound System	**Institution name**	Dalhousie University
		Expected presentation date	2020-08-28
Instructor name	Katherine Latham		

ADDITIONAL DETAILS

Order reference number	N/A

Marketplace™

Oxford University Press - Books (US & UK) - License Terms and Conditions

This is a License Agreement between Katherine Latham ("You") and Oxford University Press - Books (US & UK) ("Publisher") provided by Copyright Clearance Center ("CCC"). The license consists of your order details, the terms and conditions provided by Oxford University Press - Books (US & UK), and the CCC terms and conditions.

All payments must be made in full to CCC.

Order Date	17-Jul-2020	**Type of Use**	Photocopy for internal/external business use
Order license ID	1049137-1		
ISBN-13	9780195168310	**Publisher**	OXFORD UNIVERSITY PRESS

LICENSED CONTENT

Publication Title	Foundations of biomedical ultrasound	**Country**	United States of America
		Rightsholder	Oxford University Press - Books (US & UK)
Author/Editor	COBBOLD, RICHARD S. C.		
Date	01/01/2006	**Publication Type**	Book
Language	English		

REQUEST DETAILS

Publication year of title being used	2007	**Number of copies**	10
		Currency	CAD
Total number of pages	5		

ADDITIONAL DETAILS

Article/Chapter	Figs 6.1, 6.3, 6.20 c), 8.28	**Your reference**	N/A

PUBLISHER TERMS AND CONDITIONS

Please note. Any permission obtained through this service only relates to material owned or controlled by Oxford University Press. If the material you wish to use is acknowledged to any other source, you may also need to clear additional permission with the rights holder.

Print and Digital Transactional Terms and Conditions

All licenses are subject to Copyright Clearance Center terms and conditions and some are subject to additional terms set by the rightsholder. Please reference below the Copyright Clearance Center terms and conditions associated with your order.

Photocopy / Digital Transactional Licensing Services
Terms And Conditions (which apply to all photocopy and digital license transactions)

1. General. Licenses are granted by Copyright Clearance Center, Inc. ("CCC"), as agent for the rightsholder identified on the Order Confirmation (the "Rightsholder"). Licenses are for use of a copyrighted work as described in detail on the Order Confirmation (the "Work"), including any special limitations imposed by the Rightsholder, and may include use in the form of paper or digital reproductions. User shall be deemed to have accepted and agreed to all of these terms and conditions if User uses or reproduces the Work in any fashion. All rights not expressly granted

IEEE
Requesting permission to reuse content from an IEEE publication

A 256 x 256 2-D array transducer with row-column addressing for 3-D rectilinear imaging

Author: Chi Hyung Seo
Publication: Ultrasonics, Ferroelectrics and Frequency Control, IEEE Transactions on
Publisher: IEEE
Date: April 2009

Thesis / Dissertation Reuse

The IEEE does not require individuals working on a thesis to obtain a formal reuse license, however, you may print out this statement to be used as a permission grant:

Requirements to be followed when using any portion (e.g., figure, graph, table, or textual material) of an IEEE copyrighted paper in a thesis:

1) In the case of textual material (e.g., using short quotes or referring to the work within these papers) users must give full credit to the original source (author, paper, publication) followed by the IEEE copyright line © 2011 IEEE.
2) In the case of illustrations or tabular material, we require that the copyright line © [Year of original publication] IEEE appear prominently with each reprinted figure and/or table.
3) If a substantial portion of the original paper is to be used, and if you are not the senior author, also obtain the senior author's approval.

Requirements to be followed when using an entire IEEE copyrighted paper in a thesis:

1) The following IEEE copyright/ credit notice should be placed prominently in the references: © [year of original publication] IEEE. Reprinted, with permission, from [author names, paper title, IEEE publication title, and month/year of publication]
2) Only the accepted version of an IEEE copyrighted paper can be used when posting the paper or your thesis on-line.
3) In placing the thesis on the author's university website, please display the following message in a prominent place on the website: In reference to IEEE copyrighted material which is used with permission in this thesis, the IEEE does not endorse any of [university/educational entity's name goes here]'s products or services. Internal or personal use of this material is permitted. If interested in reprinting/republishing IEEE copyrighted material for advertising or promotional purposes or for creating new collective works for resale or redistribution, please go to http://www.ieee.org/publications_standards/publications/rights/rights_link.html to learn how to obtain a License from RightsLink.

If applicable, University Microfilms and/or ProQuest Library, or the Archives of Canada may supply single copies of the dissertation.

BACK CLOSE WINDOW